Cepheids as distance indicators and stellar tracers

G. Bono[1,2*], V. F. Braga[2] and A. Pietrinferni[3]

[1*]Department of Physics, Università di Roma Tor Vergata, via della Ricerca Scientifica 1, Roma, 00133, Italy.
[2*]INAF-Osservatorio Astronomico di Roma, via Frascati 33, Monte Porzio Catone, 00078, Italy.
[3*]INAF-Osservatorio Astronomico d'Abruzzo, via M. Maggini s/n, Teramo, 64100, Italy.

*Corresponding author(s). E-mail(s): bono@roma2.infn.it;
Contributing authors: vittorio.braga@inaf.it;
adriano.pietrinferni@inaf.it;

Abstract

We review the phenomenology of classical Cepheids (CCs), Anomalous Cepheids (ACs) and type II Cepheids (TIICs) in the Milky Way (MW) and in the Magellanic Clouds (MCs). We also examine the Hertzsprung progression in different stellar systems by using the shape of I-band light curves (Fourier parameters) and observables based on the difference in magnitude and in phase between the bump and the minimum in luminosity. The distribution of Cepheids in optical and in optical-near infrared (NIR) color–magnitude diagrams is investigated to constrain the topology of the instability strip. The use of Cepheids as tracers of young (CCs), intermediate (ACs) and old (TIICs) stellar populations are brought forward by the comparison between observations (MCs) and cluster isochrones covering a broad range in stellar ages and in chemical compositions. The different diagnostics adopted to estimate individual distances (period–luminosity, period–Wesenheit, period–luminosity–color relations) are reviewed together with pros and cons in the use of fundamental and overtones, optical and NIR photometric bands, and reddening free pseudo magnitudes (Wesenheit). We also discuss the use of CCs as stellar tracers and the radial gradients among the different groups of elements (iron, α, neutron-capture) together with their age-dependence. Finally, we briefly outline the role that near-future space and ground-based facilities will play in the astrophysical and cosmological use of Cepheids.

Keywords: stars: variables: Cepheids — stars: stellar tracers — stars: stellar evolution — stars: oscillations — stellar systems: Magellanic Clouds

Table 1 List of acronyms

AC	Anomalous Cepheid
AGB	Asymptotic Giant Branch
AHB	Above Horizontal Branch
BC	Bolometric Correction
BHB	Blue Horizontal Branch
BLH	BL Herculis
CC	Classical Cepheid
CMD	Color-Magnitude Diagram
DORB	Classical Cepheids with a bump moving down along the rising branch
EHB	Extreme Horizontal Branch
ELT	Extremely Large Telescope
FO	First Overtone
FU	Fundamental
HB	Horizontal Branch
HRD	Hertzsprung–Russel Diagram
HP	Hertzsprung Progression
IDUP	First Dredge-up
LMC	Large Magellanic Cloud
LTE	Local Thermodynamic Equilibrium
MCs	Magellanic Clouds
MIR	Mid Infrared
ML	Mass-luminosity
MS	Main Sequence
MW	Milky Way
NIR	Near Infrared
OC	Open Cluster
PEAGB	Post-Early Asymptotic Giant Branch
P(HP)	Period at the center of the Hertzsprung Progression
PL	Period–Luminosity relation
PLC	Period–Luminosity-Color relation
PW	Period–Wesenheit relation
pWV	peculiar W Virginis
RGB	Red Giant Branch
RHB	Red Horizontal Branch
RRL	RR Lyrae
RVT	RV Tauri
SMC	Small Magellanic Cloud
SO	Second Overtone
TIIC	Type II Cepheid
TO	Third Overtone
TP	Thermal Pulse
TPAGB	Thermal-pulsing Asymptotic Giant Branch
TRGB	Tip of the Red Giant Branch
UPDB	Classical Cepheid with a bump moving up along the decreasing branch
WD	White Dwarf
WV	W Virginis
ZAHB	Zero-Age Horizontal Branch

Contents

1 Introduction

Cepheids[1] are radially-pulsating variables with periodic luminosity variations used as standardizable candles and tracers of stellar populations. This review focusses on the three different flavours of Cepheids: classical Cepheids (CC, pulsation periods ranging from roughly one day to a few hundred days, absolute visual magnitudes ranging from $M_V \sim -2.5$ mag to $M_V \sim -7.5$ mag) tracers of stellar populations younger than 200–300 Myrs; Anomalous Cepheids (ACs, pulsation periods ranging from half a day to a few days, absolute visual magnitudes ranging from $M_V \sim -1$ mag to $M_V \sim -2.5$ mag) tracers of intermediate-age (a few Gyrs) stellar populations and type II Cepheids (TIICs, pulsation periods ranging from one to a hubndred days, absolute visual magnitudes ranging from $M_V \sim -1$ mag to $M_V \sim -4.5$ mag) tracers of stellar populations older than 10 Gyrs. They have been the topic of many detailed theoretical and empirical investigations and several reviews (Kraft, 1963; Sandage, 1972; Madore and Freedman, 1985, 1991; Gautschy and Saio, 1995, 1996; Sandage and Tammann, 2006; Tammann et al, 2008; Freedman and Madore, 2010; Bono et al, 1999a,b, 2010; Feast and Whitelock, 2013; Subramanian et al, 2017; Bhardwaj, 2020)

Variable stars have played a key role in the development of modern, quantitative Astrophysics. Baade's discovery (Baade, 1956) that CCs and TIICs trace young and old stellar populations and obey to two different period–luminosity (PL) relations has had an unprecedented impact upon both size and age of the Universe. Moreover, CCs one century ago were used to estimate the distance to M31 and solve the Great Debate concerning the extragalactic nature of the Nebulae (Hubble, 1925, 1929; Sandage, 2005) and to trace, for the first time, the rotation of the Milky Way (MW) thin disc (Oort, 1927; Joy, 1939; de Grijs and Bono, 2017, and references therein). More recently, they have been used as fundamental laboratories to constrain evolutionary (Anderson et al, 2016; Bono et al, 2020b; De Somma et al, 2021) and pulsation (Bono et al, 2000b; Marconi et al, 2005; Neilson and Lester, 2008; Neilson et al, 2011) properties of low and intermediate-mass stars.

The lively debate concerning the difference between evolutionary and pulsation mass of classical Cepheids dates back to the 1970s/80s and required significant improvements in micro-physics (radiative opacities, Rogers and Iglesias, 1992; Seaton et al, 1994) and in macro-physics: time-dependent convection, (Kippenhahn et al, 1980; Stellingwerf, 1982b,a, 1984a,b; Moskalik et al, 1992; Bono et al, 1994;

[1] The first Classical Cepheid – η Antinoi (the Antinous constellation was later merged with the Aquila constellation and the currently adopted name is η Aql) was discovered by the British amateur astronomer Edward Pigott on Septemebr 10, 1784, who observed it with his own telescope. He provided a very accurate estimate of its pulsation period 7.18 days compared with the current value of 7.176641 days. However, the official discovery was attributed to another amateur astronomer, John Goodricke, who, one month later, on October 20, discovered with his own telescope that the star δ in the constellation of Cepheus was a variable star. Observing the same object in subsequent nights, he estimated a period of 5.37 days (the current estimate is 5.366249 days). Edward was much more experienced with observations and he can be considered John's mentor, since he was 17 years old. John and Edward were friends and neighbours in York and they often observed together. John also had some health problems (he was deaf and mute). These are probably the reasons why the discovery was assigned to him and the objects are now-days called Cepheids instead of Aquilaes (Hoskin, 1979; Croswell, 1997).

Maeder and Meynet, 2000); extra-mixing (Chiosi et al, 1992) and mass-loss (Neilson et al, 2011).

The quest for accurate empirical estimates of the current mass of CCs reached a conclusion thanks to the discovery of CCs in double eclipsing binary systems by large photometric surveys of variable stars in the Magellanic Clouds (MCs) provided by microlensing experiments (MACHO, OGLE). The game changer in this context was the early discovery by Udalski et al (1999) and by Welch and MACHO Collaboration (1999), and in particular, the detailed and thorough investigations by Soszyński et al (2008a) and by Udalski et al (2015).

The spectroscopic follow-up of these systems provided the opportunity to measure with a geometrical method the mass of a classical Cepheid with a 1% accuracy (Pietrzyński et al, 2010). This discovery was well complemented by the discovery of a few systems in the Large Magellanic Cloud (LMC, Gieren et al, 2015), in the Small Magellanic Cloud (SMC, Graczyk et al, 2012; Pietrzyński et al, 2013) and with the measurement of the dynamical mass of Polaris (Evans et al, 2008). This paramount observational effort provided the opportunity to measure the SMC distance with 2% accuracy (Graczyk et al, 2020).

These measurements are crucial in order to fix the zero-point of the mass–luminosity relation of core helium-burning stellar structures (Neilson et al, 2011; Brott et al, 2011; Cassisi and Salaris, 2011; Prada Moroni et al, 2012), but the number is still too limited to constrain the slope over the entire period range of both FO (Pilecki et al, 2015) and FU (Pilecki et al, 2021) CCs. These systems are also fundamental laboratories to improve the physics of nonlinear pulsation models (Szabó et al, 2011; Marconi et al, 2013; Paxton et al, 2019; Smolec et al, 2023).

An accurate dynamical mass-estimate has also been recently provided for a TIIC by Pilecki et al (2018), confirming the evolutionary channel producing these variables (see section 4.2). We still lack firm estimates of the dynamical mass of an AC. In a recent very detailed investigation, Pilecki et al (2017) suggested that OGLE-LMC-T2CEP-098 is an AC, but its period is too long and its color is too red to be a canonical AC. Accurate measurements await for more solid identifications and for detailed predictions concerning binary evolution (mass-transfer phase) of pulsating stars.

The universality of the diagnostics adopted to estimate individual Cepheid distances has also been a long-standing astrophysical problem. The period–luminosity relation (PL) was discovered more than one century ago by Henrietta Leavitt, (Leavitt, 1908; Leavitt and Pickering, 1912) in a titanic effort to identify variable stars in the MCs. A few decades later, it became clear - on the basis of observations and plain physical arguments - that accurate CC individual distances would require the use of a period–luminosity–color (PLC, Sandage, 1972; Sandage and Tammann, 2006) relation. Individual distances based on the PL relation rely on the assumption that the width in temperature of the Cepheid instability strip can be neglected (Bono et al, 1999a). This assumption is less severe in the near-infrared than in the optical regime. Nonlinear, convective pulsation models at fixed chemical composition, stellar mass and luminosity, indicate that Cepheids in the NIR regime become systematically brighter when moving from the blue (hotter) to the red (cooler) edge of the instability

strip, whereas their magnitudes are almost constant in the optical regime. The difference is caused by the stronger sensitivity to effective temperature of NIR bolometric corrections when compared with optical bolometric corrections. As a consequence, the spread in magnitude of the NIR PL relation, at fixed pulsation periods, is on average a factor of two smaller than the optical PL relations (see Fig. 6 in Bono et al, 1999b). This improvement was brought forward long ago on an empirical basis by McGonegal et al (1982) and McAlary et al (1983) and it is independent of the mild dependence of NIR bands on extinction corrections.

However, the key question in using these diagnostics is: Are they Universal? Can one calibrate them here and now and use them across the Local Universe? A different way to rephrase the same question is: Are the PL and the PLC relations dependent on the metallicity? This is far from being an academic issue, since the current PL/PLC relations are calibrated by using Galactic Cepheids to fix the zero-point of the relations and the MC Cepheids to fix the slope of the same relations. However, the mean observed iron abundance of Galactic Cepheids is around solar ([Fe/H]~0) while MC Cepheids are on average a factor of two (LMC, [Fe/H]~–0.5) and a factor of four (SMC, [Fe/H]~–0.7) more metal-poor.

2 Phenomenology of Cepheids

Cepheids are typically divided into three different sub–groups: classical Cepheids, Anomalous Cepheids, and Type II Cepheids.

2.1 Classical Cepheids

CCs are central helium-burning, intermediate-mass stars with ages younger than a few hundred Myrs; they are solid young stellar tracers, associated with HII regions and young open clusters typical of Galactic thin disk and of stellar systems experiencing recent star-formation episodes (spirals, dwarf irregulars; see the top panel of Fig. 1). CCs pulsate in a variety of radial modes, the most common are fundamental, first and second overtone. Together with the single-mode oscillation, CCs are also characterized by several mixed modes, i.e. radial oscillations in which at least two radial modes are simultaneously excited. The occurrence of overtones among classical Cepheids was still a matter of discussion till the late Eighties. In a seminal investigation Bohm-Vitense (1988) suggested that a good fraction of short-period Cepheids were overtone pulsators. In the General Catalog of Variable Stars (GCVS) they were classified as “S Cepheids” where “S” stands for Cepheids with sinusoidal light curves. The final empirical evidence was provided by the microlensing experiments (MACHO, EROS, OGLE) showing hundreds/thousands of Magellanic Cepheids pulsating in the first three radial modes and in a variety of mixed modes. The name adopted for mixed mode CCs was Beat Cepheids (Rodgers, 1970), so as to distinguish them from the so-called bump Cepheids (Simon and Schmidt, 1976),

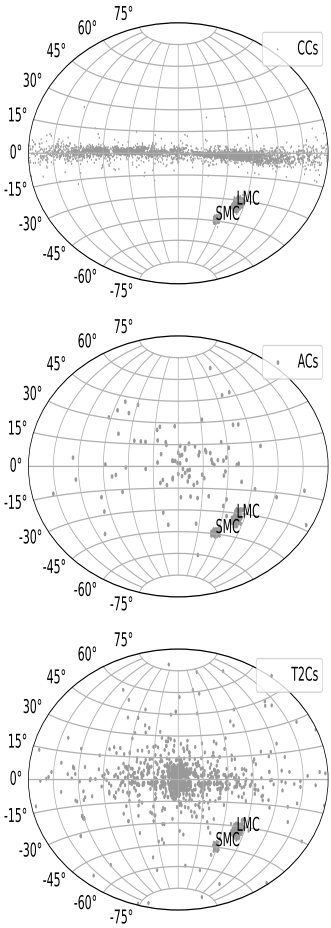

Fig. 1 Top – Distribution in Galactic coordinates of currently known CCs. The current sample includes data from Pietrukowicz et al (2021, and references therein). Galactic CCs are mainly distributed along the thin disk and the regions across the bulge. The overdensities associated with the MCs are labelled. Middle – Same as the top, but for ACs. The current sample includes data available on the OGLE Download Site (http://ogle.astrouw.edu.pl/) and on the Gaia catalog (Ripepi et al, 2022c). Bottom – Same as the middle, but for TIICs.

i.e. the CCs showing the Hertzsprung progression[2] The identification of the different modes was facilitated, since MC CCs are all located at the same distance. Therefore, the typical diagnostics adopted to estimate individual distances (PL, PLC, Period-Wesenheit [PW]) can also be adopted to identify the pulsation mode (see section 5.2).

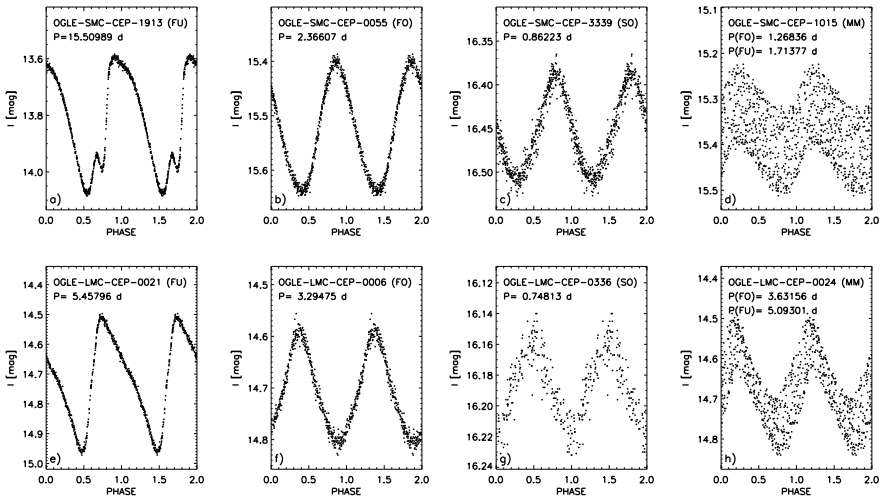

Fig. 2 Top: from left to right the light curves, based on the OGLE IV data set, for SMC CCs pulsating in the fundamental (panel a), in the first overtone (panel b), in the second overtone (panel c) and in a mixed-mode (panel d). The ID and the period (days) are labelled. For the mixed mode are labelled both primary and secondary period. Bottom: Same as the top, but for LMC CCs.

The top panels of Fig. 2 show from left to right the light curves of SMC CCs pulsating in the fundamental (panel a), first overtone (panel b), second overtone (panel c) and in a mixed mode (first overtone/fundamental, panel d), while the bottom panels (e,f,g,h) display similar light curves, but for LMC CCs. We are showing these typical light curves for MC CCs, because the empirical scenario is quite rich and includes a variety of single and mixed mode variables. The reader interested in a more detailed discussion concerning their phenomenology is referred to Soszyński et al (2015b). The current MW sample only includes a few first overtones, a single second overtone, and a very limited number of mixed-modes. The lack of these objects is an observational bias. The current Galactic photometric surveys are far from being complete,

[2]The most appropriate way to introduce and summarize the Hertzsprung progression is to use the sentences he wrote in his pioneering paper: *. . . At the shorter periods up to about 6 days the curves show the characteristic regular δ Cephei form with quick rise and slow decrease, without additional peculiarites. Above 6 days a secondary wave on the descending branch of the light curve makes its appearance. This secondary wave is a very characteristic feature of the following periods. For periods between 10 and 13 days, the secondary wave is, when present, situated on top of the suppressed ordinary maximum, the form of the light curve being nearly symmetrical. . . . The secondary wave has superseded the maximum shown at shorter periods. At periods of about 14 or 15 days the new superposed maximum occurs earlier, giving the light curve again an unsymmetrical shape with a hesitation in the increase of the brightness about midway between minimum and maximum. This hesitation is persistent at the periods mentioned and not found at any other period materially different from them. . . . At periods longer than 16 days several curves are found rather similar to that of δ Cephei, showing quick rise and slow decrease apparently without complications.* (Hertzsprung, 1926, see also section 3).

since the current limiting magnitude in the optical regime is $I \approx 19$ mag. The observational bias becomes more severe in the inner/outer disk and beyond the Galactic center, due to the high column density of dust along the line of sight. The surface density of CCs (see Table 3) across the thin disk in the annulus in Galactocentric distance between 7 and 9 kpc is ρ=5.64 per kpc^2, while in the annulus between 5 and 7 kpc it is 20% smaller (ρ=4.51 per kpc^2). However, the density gradient of stars steadily increases when moving toward the inner disk and the surface density of CCs should show the same trend. This is also the reason why the peak in the iron distribution of CCs is at solar-iron abundance.

Pulsation models and observations indicate that the topology of the CC instability strip depends on the metal content. Moreover, evolutionary models also indicate that the width in temperature of the blue loop, and in turn, the minimum mass crossing the CC instability strip depend on the metal content. These circumstantial evidence takes account of the limited number of Galactic second overtones and mixed-mode variables currently known. This bias is going to be removed by the current ongoing long-term photometric surveys either of the Galactic plane (OGLE, Skowron et al, 2019) or by an all-sky survey like Gaia (Gaia DR3).

Panel a) of Fig. 3 shows the period distribution of both fundamental (red hatched area) and first overtone CCs (light blue hatched area). This sample includes CCs collected by OGLE IV (Skowron et al, 2019; Pietrukowicz et al, 2021). We adopted this sample because accurate and homogeneous photometry and pulsation parameters are available for both MC and MW variables. The mixed mode Cepheids pulsating either in FO(primary)/FU(secondary) or in FU/FO were included by using their dominant periods. The histograms plotted in this panel display that FUs peak at $P \sim 4$ days ($\log P \sim 0.60$) and the distribution is skewed towards longer periods, with a secondary maximum (shoulder) located at $P \sim 12.5$ days ($\log P \sim 1.1$). As a whole, the periods range from roughly one day to 50 days. The FOs peak at $P \sim 1.5$ days ($\log P \sim 0.20$), their distribution is skewed towards shorter periods and their periods range from ~0.18 days to ~5.6 days.

Note that no single-mode second overtone CC is currently known in the MW. The variable V473 Lyr is a second overtone CC, but shows strong amplitude and phase modulations (Burki and Mayor, 1980; Breger, 1981; Molnár and Szabados, 2014; Molnár et al, 2017). Galactic double-mode and mixed-mode CCs, including a second overtone mode, have also been identified (Pardo and Poretti, 1997; Beltrame and Poretti, 2002; Sziládi et al, 2007; Poretti et al, 2014), but they are few and were not included.

Panel b) of Fig. 3 shows the Bailey diagram (I-band amplitude versus logarithmic period) for Galactic CCs. This panel only includes CCs with accurate and homogeneous I-band light curves collected by OGLE IV along the Galactic plane.

The FO amplitudes are on average a factor of two smaller than FU amplitudes. The FU amplitudes display a broad distribution with amplitudes ranging from $\Delta I \sim 0.2$ mag to $\Delta I \sim 0.8$ mag. There is a mild evidence for a minimum in amplitudes for periods ranging from $P \sim 6.5$ to 10 days ($\log P \sim 0.8$ to $\log P \sim 1$). The reason for this secondary minimum will become clearer in the following.

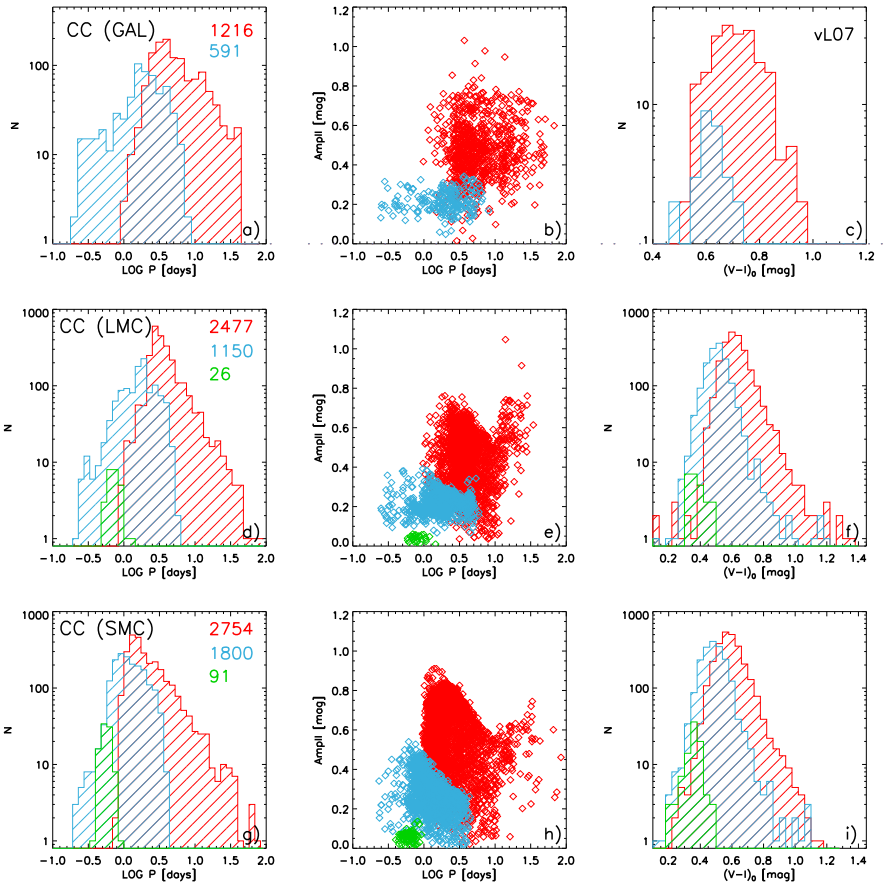

Fig. 3 Top: Panel a)– Period distribution for fundamental (red hatched area), and first overtone (light blue hatched area) Galactic CCs. Note that the Y-axis is logarithmic. Panel b)– I-band luminosity amplitude versus logarithmic period (Bailey diagram) for FU (red), and FO (light blue) Galactic CCs. Panel c)– Dereddened $(V-I)_0$ color distribution for CCs. The sample adopted for the color distribution is based on multi-band optical photometry provided by van Leeuwen et al (2007, vL07) and on individual reddenings provided by Tammann et al (2003). Middle: Same as the top, but for LMC CCs (panels d,e,f). The green hatched area shows the period distribution of second overtone CCs. Bottom: Same as the middle, but for SMC CCs (panels g,h,i).

Panel c) shows the dereddened color distribution of both FOs and FUs. This panel only includes CCs for which are available accurate and homogeneous estimates of V,I photometry and individual reddenings. The main source for the photometry is van Leeuwen et al (2007), while for the reddening is Tammann et al (2003). The latter authors performed a critical analysis not only of the reddening estimates available in the literature, but also on the absorption coefficients and on their impact on the Period-Color relations (see also Laney and Caldwell, 2007). As expected, the FOs are systematically bluer than FUs and peak at $(V-I)_0 \sim 0.63$ mag, while the FU peak at $(V-I)_0 \sim 0.73$ mag (see Table 2).

The parameters adopted to discuss the pulsation properties of CCs are independent of uncertainties affecting either distance and reddening estimates (periods, luminosity amplitudes) or distance estimates (colors). The dispersion in period and amplitude distribution is driven by differences in evolutionary and/or in pulsation properties (Bono et al, 2020a).

The middle panels of the same figure show the same parameters, but for LMC CCs. Data plotted in these panels display several interesting features worth being discussed in detail.

i)–FO period distribution– The number of FOs (light blue diamonds) is significantly larger than for Galactic Cepheids, indeed the population ratio between FO/FU increases by ∼50% (0.49 versus 0.72). Moreover, their periods range from 0.18 days to 6.3 days and their period distribution shows two well-defined shoulders for periods of ∼0.3 days and ∼1 day ($\log P \sim -0.5$ and 0.0).

ii)–FU period distribution– The period distribution of FUs (red diamonds) is broader, indeed their periods range from about a half day to more than one hundred days. Moreover, the shoulder (secondary maximum) identified in Galactic CCs is now located at longer periods, around 20 days ($\log P \sim 1.3$) but is less evident.

iii)–SO period distribution–The LMC include a sizable sample of SO CCs (green diamonds) that are only minimally present among Galactic CCs.

Panel e) shows the Bailey diagram. A glance at the data plotted in this panel shows that FUs display the typical "V"-shape with a well-defined maximum for periods around 2.5 days ($\log P$ ∼0.4) and a secondary minimum for periods around ten days (Bono et al, 2000b). The main peak is connected with the peak in the period distribution, while the secondary minimum is associated with the Hertzsprung progression and to the so-called bump Cepheids (see section 3). For periods around ten days, the phase of the bump along the pulsation cycle approaches the maximum in surface brightness, and the luminosity amplitude attains a minimum (associated with a minimum in radius) when compared with shorter- and longer-period Cepheids. The amplitude distribution of FO Cepheids is more complex, its maximum is located at periods around 1.26 days ($\log P \sim 0.10$) and shows secondary maxima around 1 and 0.3 days ($\log P \sim 0.0$ and -0.5). The SOs are characterized by small amplitudes and also cover, as expected, a narrow range in periods.

Panel f) shows the dereddened $(V-I)_0$ color distribution. The difference in color between Galactic and LMC CCs, the latter being systematically bluer, was noted more than a half century ago by Gascoigne and Kron (1965) and more recently by Laney and Stobie (1994). Data plotted in this figure show that FU, FO and SO color distributions are quite symmetrical and the median $(V-I)_0$ colors peak at $(V-I)_0 = 0.651 \pm 0.107$ mag (FU), $(V-I)_0 \sim 0.530 \pm 0.091$ mag (FO) and $(V-I)_0 \sim 0.368 \pm 0.129$ (SO) mag, where the errors are the standard deviations (see Table 2).

The bottom panels show the same parameters of middle and top panels, but for SMC CCs. The period distributions plotted in panel g) show that SOs are more representative compared with the LMC, and indeed the population ratio SO/FO increases by a factor of three (0.01 versus 0.03). They also cover a narrower range in period ($0.40 \leq P(\mathrm{SO}) \leq 0.92$ vs $0.58 \leq P(\mathrm{SO}) \leq 1.46$ days) and a broader range in luminosity amplitudes (panel h) when compared with LMC SOs.

Table 2 Median *V-I* colors (mag) of Magellanic Cloud and Milky Way Cepheids.

Mode	*V-I* [mag]		
	SMC	LMC	MW
		—CCs—	
FU	0.613± 0.102	0.651± 0.107	0.726± 0.094
FO	0.509± 0.095	0.530± 0.091	0.629± 0.059
SO	0.373± 0.056	0.368± 0.129	...
		—ACs—	
FU	0.530± 0.066	0.485± 0.107	0.556± 0.223
FO	0.386± 0.092	0.399± 0.096	0.405± 0.266

The errors associated with the median colors are the standard deviations.

The peak in the period distribution of SMC FUs and FOs shifts towards shorter periods (∼0.9 days (FO), ∼1.5 days (FU) vs ∼1.8 (FO) days, ∼2.8 days (FU)). The range in periods shows the same trend: $0.25 \leq P(\mathrm{FO}) \leq 4.5$ vs $0.25 \leq P(\mathrm{FO}) \leq 6.0$ days and $0.84 \leq P(\mathrm{FU}) \leq 129$[3] vs $0.97 \leq P(\mathrm{FU}) \leq 134$ days, respectively. Note that the shoulder located in the long period tail of FU CCs is now placed at even longer periods when compared with Galactic and LMC CCs, i.e. around 25 days ($\log P \sim 1.4$).

The *I*-band luminosity amplitudes plotted in panel h) display quite clearly that the secondary minimum linked with the Hertzsprung progression moves SMC bump Cepheids towards longer periods, $P \sim 9.8 \pm 0.1$ days. Moreover, the peak in the *I*-band luminosity amplitudes moves towards shorter periods, namely 1.58 days (FU, $\log P \sim 0.2$), 0.79 days (FO, $\log P \sim -0.1$) and 0.63 days (SO, $\log P \sim -0.2$). Finally, the dereddened $(V - I)_0$ colors of SMC CCs plotted in panel f) and listed in Table 2 are either similar (SO) or systematically bluer than LMC and Galactic CCs.

The circumstantial evidence emerging in the comparison between Galactic and Magellanic CCs can be summarized as follows:

i)– The peak in the period distributions and the range in period covered by FU, FO and SO CCs steadily move towards shorter periods when moving from Galactic to LMC and SMC CCs. On the other hand, the shoulder located in the long period tale of FU CCs, moves in the opposite direction: it is placed at longer periods when moving from Galactic to LMC and SMC CCs.

ii)– The center of the Hertzsprung progression, i.e. the period in which bump Cepheids attain a well-defined minimum in luminosity amplitude, steadily moves towards longer periods when shifting from Galactic to LMC and SMC FU CCs.

iii)– The peak in the Bailey diagram for FU and FO CCs systematically shifts towards shorter periods when moving from metal-rich to more metal-poor stellar systems (Galaxy–LMC–SMC).

iv)– The color distribution of FU and FO CCs becomes systematically bluer when moving from Galactic to LMC and to SMC (see Table 2). This evidence cannot be extended to SO CCs, since they are vanishing in the MW and only two dozens are currently known in the LMC. The evidence that the peak in color when moving from FU to FO and to SO MC CCs becomes systematically bluer, fully supports pulsation predictions concerning the topology of the instability strip. Indeed, the regions in which

[3]The SMC sample includes a long-period CC with $P \sim 208$ days.

they show a stable limit cycle become, at fixed chemical composition, systematically hotter when moving from the fundamental mode to the overtones.

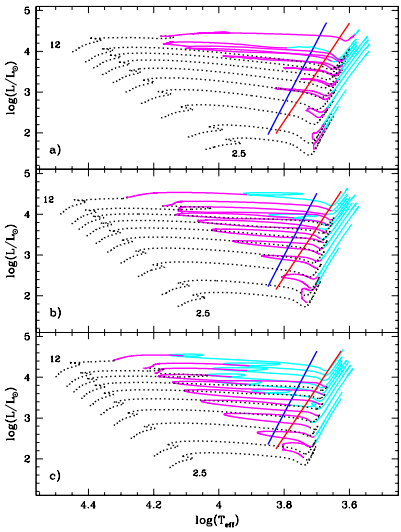

Fig. 4 Panel a)– Scaled solar evolutionary tracks for young stellar structures computed by neglecting convective overshooting during core hydrogen-burning phases in the Hertzsprung–Russell diagram at fixed chemical composition (metal mass fraction, Z=0.02) and stellar masses ranging from 2.5 to 12 $M/M_{\odot}$ (see labels). The dashed lines display hydrogen-burning phases, while the magenta color marks central helium-burning phases, the cyan color marks double-shell (H and He) burning phases (Asymptotic Giant Branch). The almost vertical solid lines display the blue (hot, first overtone) and the red (cool, fundamental) edge of the CC instability strip (Fiorentino et al, 2002; De Somma et al, 2021). Panel b)– Same as Panel a), but for a more metal-poor chemical composition Z=0.01. Panel c)– Same as Panel b), but for a more metal-poor chemical composition Z=0.001.

Theoretical and empirical evidence indicate that the difference in the evolutionary and pulsation properties of CCs when moving from the MW to the MCs is caused by the iron content. Indeed, current metallicity determinations based on high-resolution spectra indicate that the mean observed iron abundance of MW CCs is solar, whereas LMC CCs are on average a factor of two more metal-poor and SMC CCs are a factor of four more metal-poor. Panels a), b) and c) of Fig. 4 display the comparison between evolutionary and pulsation predictions over a broad range of chemical compositions (for more details see section C in Appendix).

In the following, we will discuss the population ratios of the different pulsation modes. Before discussing them, we point out that, for the MW samples, we will only derive the ratios based on the OGLE sample. In fact, OGLE is the only survey allowing an extremely detailed and accurate analysis of the mixed-mode classifications. We did not include Gaia classification, because the sampling of the light curves is still based on a modest number of phase points.

Data listed in Table 3 show that the population ratio between first overtone and fundamental CCs is 0.65±0.02 in the SMC, 0.72±0.02 in the LMC and 0.49±0.01 in the MW. The observed population ratios do not show a clear dependence on the observed iron abundance and probably hint to a possible observational bias in the Galactic sample. The population ratio between second overtone and fundamental CCs decreases, as expected, when moving from more metal-poor to more metal-rich stellar systems (0.03 [SMC] vs 0.01 [LMC]) and it is vanishing for the MW. On the other hand, the fraction of mixed mode variables does not show a clear dependence on the metallicity (0.11±0.01, [SMC]; 0.17±0.01, [LMC]; 0.14±0.01, [MW]).

The population ratio between first overtone and fundamental ACs, listed in Table 3, is similar in the MCs (0.54±0.10, SMC; 0.44±0.08, LMC), while in the MW attain a larger value (0.76±0.11). However, the Poissonian uncertainties are large and do not allow us to reach firm conclusions. The reader interested in a more detailed discussion concerning the statistics of ACs in nearby dwarf galaxies is referred to Monelli and Fiorentino (2022).

The relative number of the different subgroups of TIICs changes when moving from the MCs to the MW. The MW has the highest fraction of BLHer variables (0.38±0.02) compared to the LMC (0.34±0.01) and to the SMC (0.28±0.01). The fraction of WVir, including pWVir, follows an opposite trend, decreasing from the SMC (0.51±0.01), to the LMC (0.46±0.01), and the MW (0.43±0.02). Interestingly enough, the fraction of RVTau variables is, within the errors, constant in the three different stellar systems, namely 0.19±0.01 (MW), 0.19±0.01 (LMC) and, 0.21±0.01 (SMC). The population ratio between fundamental and first overtone is meaningless for TIICs, due to the paucity of FOs which have been identified sofar. Indeed, after the seminal discovery of two FO TIICs in the LMC by Soszyński et al (2019) only three other variables were identified in the MW by Ripepi et al (2022c, see also Table 3).

2.2 Anomalous Cepheids

Anomalous Cepheids (ACs)[4] are low-mass stars with stellar masses ranging from 0.8 to 1.8 (Fiorentino and Monelli, 2012) in which central helium burning takes place in a partially electron-degenerate helium core. They are associated with intermediate-age stellar tracers. The current evidence indicates that they might be the aftermath of both single and binary merging evolutionary channels. This is the reason why they are ubiquitous over the entire Galactic spheroid and in nearby galaxies (see the middle panel of Fig. 1). However, theory and observations suggest that only stellar populations more metal-poor than [Fe/H]$\lesssim -1.5$ cross the Cepheid instability strip. This is the reason why they mainly show up in metal-poor/metal-intermediate stellar systems.

ACs display quite regular light curves for both fundamental and first overtone variables. The majority of Magellanic ACs, the sample for which we have a more

[4]The definition of Anomalous Cepheids dates back to Zinn and Searle (1976, see their Fig. 1) in their detailed analysis of the mass-distribution of Draco dSph variable stars. The anomaly was driven by the evidence that ACs, at fixed pulsation period, are brighter than RR Lyrae (RRLs) and TIICs, and fainter than CCs. The increase of a factor of two in the stellar mass for ACs, when compared with RRLs and TIICs, was originally suggested by Christy (1970). The reader interested in a more detailed discussion concerning the early discoveries of ACs in globulars and dwarf galaxies is referred to Monelli and Fiorentino (2022).

Table 3 Number of Magellanic Cloud and Milky Way Cepheids and their pulsation mode.

Mode	SMC	LMC	MW (OGLE)	MW (PP)	MW (all)
		—Classical Cepheids—			
FU	2754	2477	1216	2250	...
FO	1800	1778	591	1092	...
SO	91	26	0	1	...
		Mixed Mode			
FU/FO	69	96	59	100	...
FO/SO	239	322	161	201	...
FO/TO	0	1	0	0	...
SO/TO	0	1	3	3	...
FU/FO/SO	0	1	2	3	...
FO/SO/TO	1	7	8	8	...
		—Anomalous Cepheids—			
FU	79	102	38	...	118
FO	43	45	81	...	90
MM	0	0	1	...	1
		—Type II Cepheids—			
FU(tot)	53	291	1666	...	2187
FU(BLHer)	20	99	674	...	838
FU(WVir)	15	108	609	...	869
FU(pWVir)	7	27	67	...	67
FU(RVTau)	11	55	313	...	410
FO	0	2	3	...	3

The source and the mode identification for Cepheids in the "SMC", "LMC" and "MW(OGLE)" column come from the OGLE IV data set (http://ogle.astrouw.edu.pl/ and references therein). The source and the mode identification for CCs listed in the column "MW (PP)" come from Pietrukowicz et al (2021) and they are based on the cross-identification they performed with the Gaia catalog (Ripepi et al, 2022c) and with catalogs available in the literature. The source and the mode identification for ACs and TIICs listed in the column "MW (all)" is based on the cross-identification (matching radius of 1 arcsec) that we performed between the catalogs available on the OGLE Download Site (http://ogle.astrouw.edu.pl/) and the Gaia catalog (Ripepi et al, 2022c).

detailed knowledge, mainly includes FU variables, indeed the population ratio is ~0.65–0.70. They were considered, until a few years ago, single mode variables, but Soszyński et al (2020) found a Galactic triple mode AC. Figure 5 shows representative light curves for Galactic, LMC and SMC ACs in the three different pulsation modes.

The AC pulsating in the fundamental-mode have pulsation periods ranging from 0.6 to 2.7 days, while the first-overtones oscillate with periods ranging from 0.4 to 1.2 days. The period distributions are quite similar when moving from Galactic to Magellanic ACs (see left panels in Fig. 6). The same outcome applies to the I-band luminosity amplitudes, the FO amplitudes are on average a factor of two smaller than fundamental ones (see middle panels in Fig. 6). The color $(V-I)$ distribution covered by Magellanic ACs are quite similar, thus suggesting a marginal dependence on the metallicity (see right panels in Fig. 6). The comparison with Galactic ACs is hampered by the dependence of the reddening correction in the Bulge and on the adopted reddening law in the disk. In order to overcome possible systematics, the intrinsic $(V\text{-}I)_0$ colors of ACs in the Galactic Bulge were estimated using the reddening map provided by Nataf et al (2013), while for the others we adopted the reddening maps provided by Schlegel et al (1998) and by Schlafly and Finkbeiner (2011) and the Cardelli et al (1989) reddening law. We found that their median intrinsic colors are

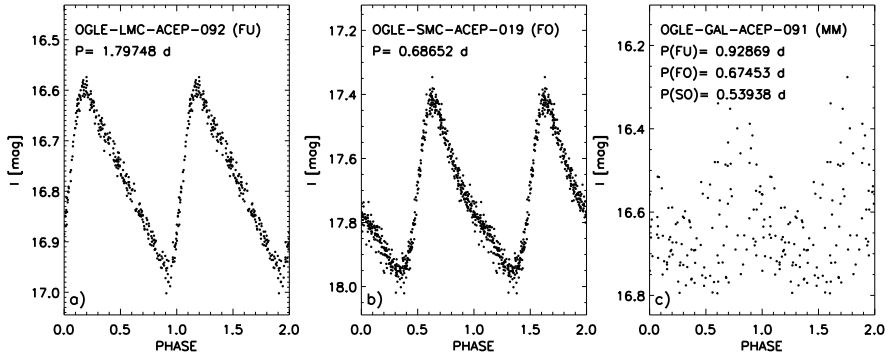

Fig. 5 Panel a): Light curve for an LMC AC pulsating in the fundamental mode from the OGLE-IV data set. The ID and the period (days) are labelled. Panel b): Same as the left, but for an SMC AC pulsating in the first overtone. Panel c): Same as the left, but for the Galactic AC pulsating simultaneously in the first three radial modes. Primary and secondary periods (days) are labelled.

$(V\text{-}I)_0$=0.556±0.223 mag (FU) and $(V\text{-}I)_0$=0.405±0.266 mag (see Table 2) and they are quite similar, within the errors, to the intrinsic colors of MC ACs.

The predicted dependence of ACs evolutionary and pulsation properties on the chemical composition are showed in Fig. 7). Panels a), b) and c) display evolutionary tracks for metal-poor (see labelled values) intermediate-age stellar structures (for more details see section C in Appendix). However, spectroscopic abundances are only available for two Galactic ACs (V716 Oph, BF Ser) that were originally classified as TIICs (Kovtyukh et al, 2018), but we still lack a detailed abundance analysis for both Galactic and Magellanic ACs.

2.3 Type II Cepheids

TIICs[5] are low-mass stars in a double shell, helium and hydrogen, burning phase. According to the pulsation period, they are either Asymptotic Giant Branch (AGB) or post-AGB radial variables. They are solid old ($t \geq$10 Gyr) stellar tracers and have been identified in stellar systems hosting old stellar populations (Halo, Bulge, globulars, Magellanic Clouds, Andromeda group; see the bottom panel of Fig. 1). However, they have not been identified in nearby dwarf spheroidal galaxies. It is not clear yet whether this evidence is either an observational bias, or caused by the lack of hot and extreme horizontal branch stars in these stellar systems, as recently suggested by Bono et al (2020b).

The pulsation properties of TIICs are canonical, since they pulsate as single mode variables in the fundamental and in the first overtone, but the latter group only includes a few objects both in the Galaxy and in the Magellanic Clouds (Soszyński et al, 2019). Interestingly enough, long-term photometric surveys have also identified a few mixed-mode TIICs (Smolec et al, 2018; Udalski et al, 2018). The top panels (a,b,c) of Fig. 8 shows representative light curves for Galactic single and mixed-mode

[5]They were originally called Globular Cluster Cepheids by (Baade, 1956) thanks to the discovery of stellar populations. The reader interested in a more detailed discussion concerning early discoveries based on TIICs is referred to Wallerstein and Cox (1984).

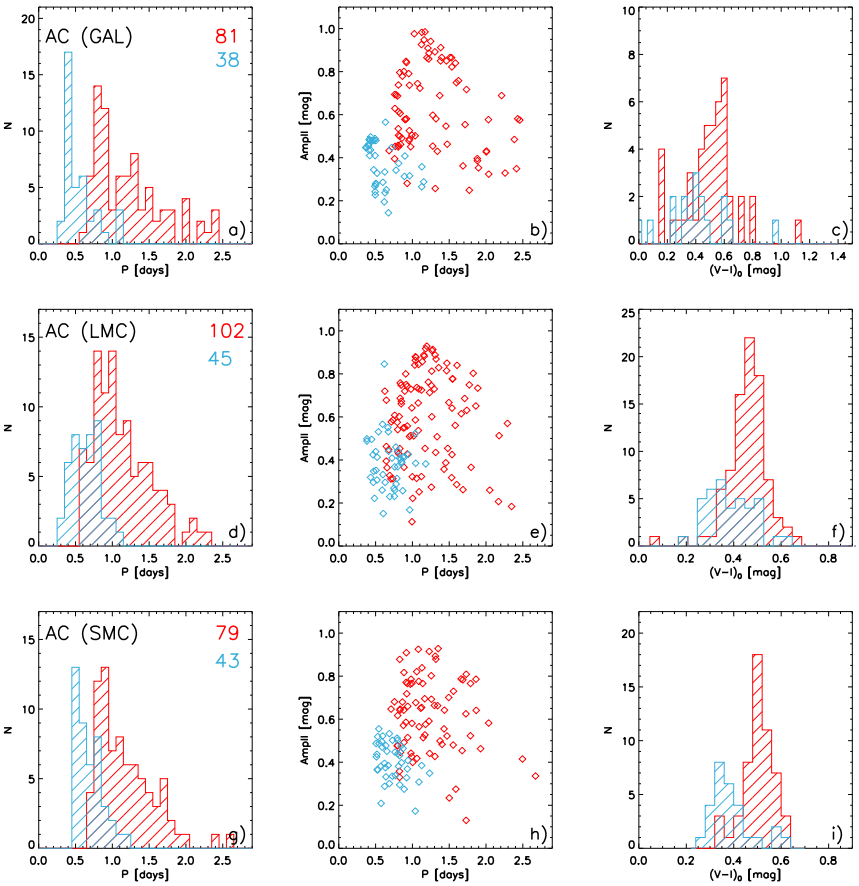

Fig. 6 Top: Panel a)– Period Distribution for fundamental (red-hatched area) and first overtone (light-blue hatched area) Galactic ACs. Panel b)– I-band luminosity amplitude versus period (Bailey diagram) for both FU and FO ACs. Panel c)– dereddened $(V - I)_0$ color distribution for the same ACs plotted in the left and in the middle panel. Middle: Same as the top, but for LMC ACs. Bottom: Same as the top, but for SMC ACs.

TIICs, while the bottom panels display selected light curves for TIICs typical of the three sub-groups: a Galactic Bulge BLH (panel d), an LMC WV (panel e) and an SMC RVT (panel f).

The separation between RRLs and TIICs is a long-standing problem. As a first approximation, it is possible to adopt a period threshold, whose exact value is still a matter of debate. A threshold of ∼0.8 days was set in the review by Gautschy and Saio (1996) where type 1 variables (AHB1, above the Horizontal Branch [HB]), as defined in Strom et al (1970) and Diethelm (1983, 1990), were considered as TIICs rather than evolved RRLs. This threshold is obsolete, however, because a more extended and homogeneous investigation, based on period distribution and on the Fourier parameters of the light curve of RRLs in the Galactic bulge, has now set the threshold at one day (Soszyński et al, 2008b, 2014). The RRLs in the bulge have a

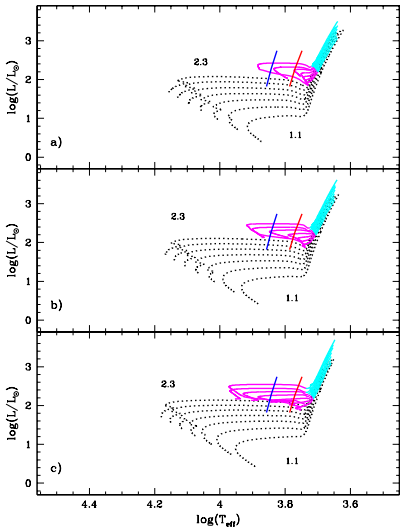

Fig. 7 Panel a)– Evolutionary tracks for intermediate-age stellar structures in the Hertzsprung–Russell diagram at fixed metallicity (Z=0.0008) and stellar masses ranging from 1.1 to 2.3 $M/M_{\odot}$ (see labels). The magenta color marks central helium-burning phases, whereas the light blue color marks double-shell (H and He) burning phases (Asymptotic Giant Branch). The almost vertical solid lines display the blue (hot) and the red (cool) edge of the Anomalous Cepheid instability strip (Fiorentino and Monelli, 2012; Monelli and Fiorentino, 2022). Panel b)– Same as panel a), but for Z=0.0004. Panel c)– Same as panel a), but for Z=0.0002.

primordial (or minimally enhanced) helium abundance (Marconi and Minniti, 2018), but there is theoretical evidence that helium enhancement increases the periods of RRLs (Marconi et al, 2018). This means that a one-day period threshold should be considered a particular case of a more general chemical and evolution-dependent threshold.

TIICs have periods ranging from 1 day to more than 100 days (see left panels in Fig. 9). Moreover, they display two local minima in the period distribution for $P \sim 5$ and $P \sim 20$ days. The former value was adopted for separating BLHs from WVs, and the current data indeed suggest that it ranges from about four days in the Bulge to about six days in the Galactic field. The latter value ($P \sim 20$ days) was adopted for separating WVs from RVTs, and the current data suggest that it shows up as a shoulder in the period distribution of Bulge and field TIICs and as a local minimum in GCs and in Magellanic TIICs.

The difference in the period distribution among BLHs, WVs, and RVTs is fully supported by the Bailey diagrams, the I-band luminosity amplitudes versus the logarithmic period, showed in the middle panels of Fig. 9. The Bailey diagram shows that WVs attain a well-defined minimum at $P \sim 8$ days, with a steady increase towards longer periods. The trend for RVTs is far from being homogeneous, because the maximum around 20 days is broad. Moreover, RVTs in the Bulge and in the LMC display a steady decrease towards longer periods and a well-defined cutoff at periods longer

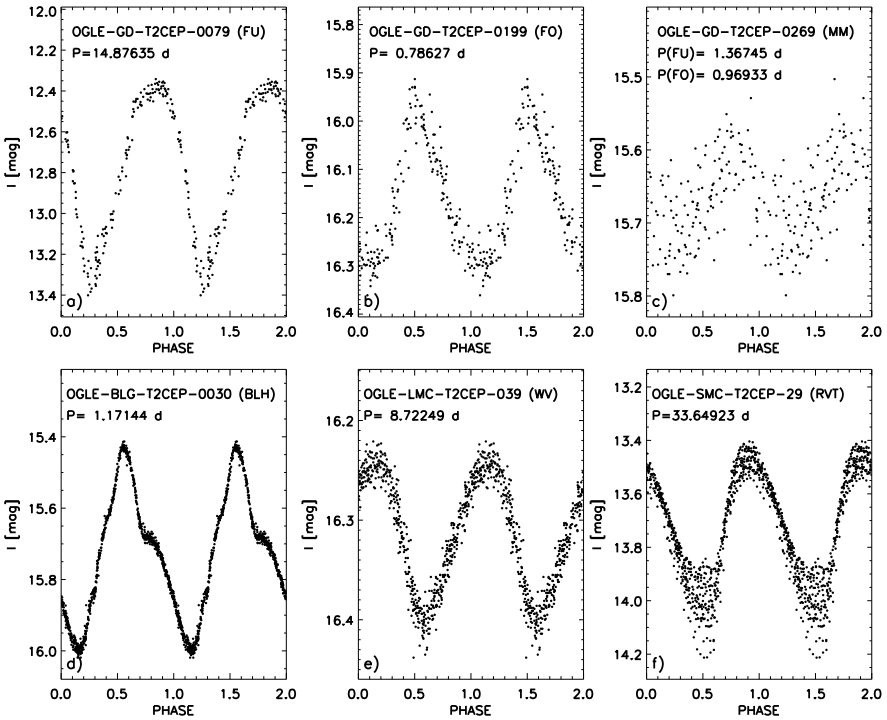

Fig. 8 Panel a): Light curve for a Galactic TIIC pulsating in the fundamental mode from the OGLE IV dataset. The ID and the period are labelled. Panel b): same as panel a), but for a Galactic first overtone TIIC. Panel c): same as panel a), but for a Galactic mixed-mode TIIC. Primary and secondary periods are labelled. Panel d): same as panel a), but for a Galactic Bulge BL Herculis. Panel e): same as panel a), but for a LMC W Virginis. Panel f): same as panel a), but for a SMC RV Tauri.

than 60 days. On the other hand, RVTs in the Galactic field approach 200 days and display at fixed periods a broad range in luminosity amplitudes.

The current partition of TIICs into three sub-groups follows the classification suggested by Soszyński et al (2008b, 2011). They also suggested a new group of TIICs, the peculiar WVs (pWVs) which have peculiar light curves. Moreover, the pWVs are, at fixed periods, brighter than typical TIICs.

The possible dependence on the metallicity requires a more detailed discussion. We still lack spectroscopic measurements of Bulge TIICs, so we assume that their metallicity distribution is either similar to that of Bulge RRLs as measured by Walker and Terndrup (1991), suggesting a mean [Fe/H]= −1.0 with a 0.16 dex standard deviation, or similar to Bulge red giant stars, with average [Fe/H]= −1.5 and a standard deviation equal to 0.5 dex (Rich et al, 2012; Zoccali et al, 2017). The metallicity distribution of TIICs in GCs and in the Galactic field ranges from [Fe/H]∼ −2.4 to slightly super solar [Fe/H] (see Appendix in Bono et al, 2020b).

For LMC TIICs, we can follow two different paths. According to Gratton et al (2004) the iron abundance of LMC RRLs based on low-resolution spectra range from [Fe/H]= −2.1 to [Fe/H]= −0.3, but only a few stars are more metal-rich than [Fe/H]=

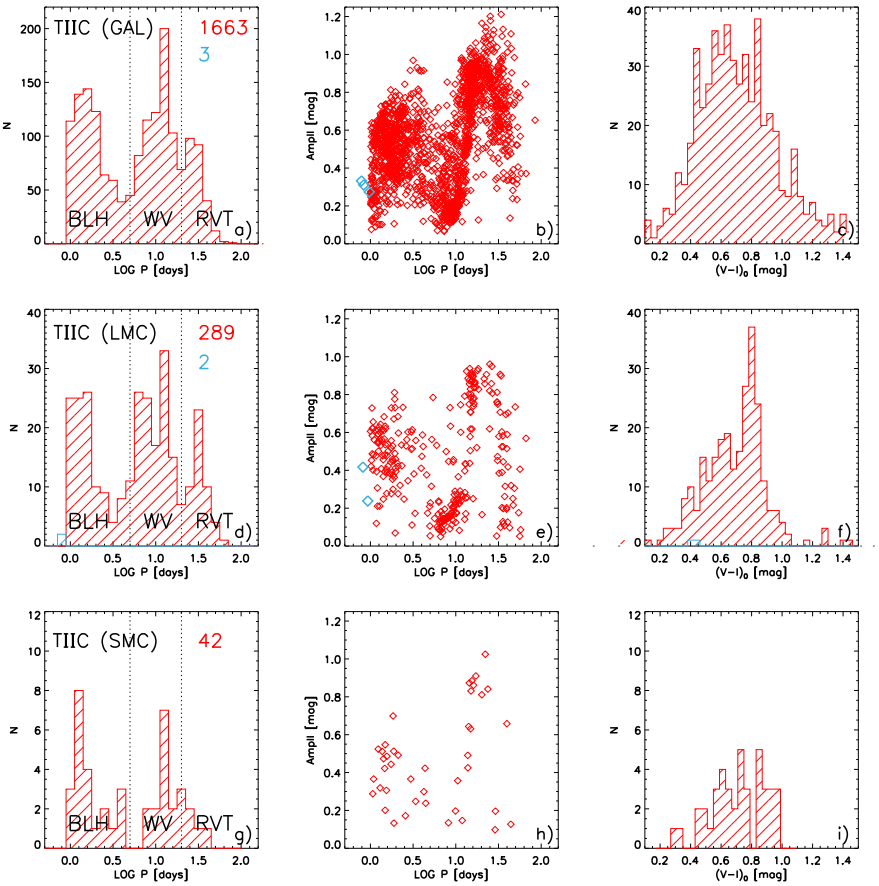

Fig. 9 Top: Panel a)– Period distribution for fundamental (red hatched area) and first overtone (light blue hatched area) Galactic TIICs. Panel b)– I-band luminosity amplitude versus period (Bailey diagram) for both FU and FO TIICs. Panel c)– dereddened $(V-I)_0$ color distribution for the same TIICs plotted in the left and in the middle panel. Middle: Same as the top, but for LMC TIICs. Bottom: Same as the top, but for SMC TIICs.

-1.0; the mean observed iron abundance for 98 RRLs is [Fe/H]= $-1.48 \pm 0.03 \pm 0.06$. This metallicity range is also supported by recent investigations of the mean metallicity of LMC globular clusters. Using homogeneous Strömgren photometry, Piatti and Koch (2018) found, in agreement with spectroscopic measurements, that the metallicity of the ten LMC globulars ranges from -2.1 dex (NGC 1841) to -1.1 dex (ESO121-SC3). We still lack direct measurements of the metallicity distribution of truly old SMC stellar tracers. According to high-resolution spectroscopy (Dalessandro et al, 2016), the metallicity of NGC 121, the only SMC globular cluster, is [Fe/H]= -1.28. Metallicity estimates listed in Table A.1 of Bono et al (2020b) indicate that TIICs cover roughly three dex in metal abundance. However, the population ratios appear to be, within the errors, quite similar. This finding is also supported by

the similarity in the color distribution between Galactic and Magellanic TIICs (see right panels in Fig. 9).

TIICs can be thought as the intersection of several theoretical and empirical investigations; however, their evolutionary status is far from being well established. A first analysis of the evolutionary properties of TIICs was provided over 40 years ago by Gingold (1974, 1976, 1985). He recognized that a significant fraction of hot (blue) HB stars evolve off the Zero-Age Horizontal Branch (ZAHB) from the blue (hot) to the red (cool) region of the color–magnitude diagram (CMD). In the approach to their AGB track, these stars are in a double shell (hydrogen and helium) burning phase (Salaris and Cassisi, 2005) and cross the instability strip at luminosities systematically brighter than typical RRLs. The difference in luminosity and the lower mass induce an increase in the pulsation period of TIICs when compared with RRLs. Typically, the two classes are separated by a period threshold at one day. This separation is supported by a well-defined minimum of the period distribution when moving from RRLs to TIICs, but the physical mechanism(s) causing this minimum are not yet clear, and the exact transition between RRLs and TIICs has not been established (Braga et al, 2020).

The quoted calculations also suggest that blue HB stars after the first crossing of the instability strip experience a "blue nose" (then dubbed "Gingold's nose"), a blue-loop in the CMD that causes two further crossings of the instability strip before the tracks reach the AGB. These three consecutive excursions were associated with the interplay between the helium and hydrogen burning shells. After core-helium exhaustion, HB models with massive enough envelopes evolve redward in the CMD. The subsequent shell-helium ignition causes a further expansion of the envelope, and, in turn, a decrease in the efficiency of the shell-hydrogen burning, which causes a temporary contraction of the envelope, and a blueward evolution in the CMD. Once shell hydrogen burning increases its energy production again, these models move back towards the AGB track. Finally, these models would eventually experience a fourth blueward crossing of the instability strip before approaching their white dwarf (WD) cooling sequence (see Fig. 1 in Gingold 1985 and Fig. 2 in Maas et al 2007). During their final crossing of the instability strip, these stellar structures (in the post-AGB phase) are only supported by a vanishing shell H-burning.

Basic arguments based on their evolutionary status and on the use of the pulsation relation available at that time (van Albada and Baker, 1973) allowed Gingold to associate the first three crossings (including Gingold's nose) with BLHs and the fourth one with the WVs variables. These early analyses, however, lacked quantitative estimates of the time spent inside the instability strip during the different crossings, and in particular the period distributions associated with the different crossings. Moreover, HB evolutionary models dating back to more than 25 years ago and based on updated input physics (Lee et al, 1990; Castellani et al, 1991; Dorman and Rood, 1993; Brown et al, 2000; Pietrinferni et al, 2006a; Dotter, 2008; VandenBerg et al, 2013) do not show the Gingold's nose.

The evolutionary properties of low-mass core helium burning models have been discussed in several recent investigations (Cassisi and Salaris, 2011, and references

therein). Here we summarize the main relevant features in order to explain the evolutionary channels producing TIICs.

The grey area displayed in the top panel of Fig. 10 outlines the region between the ZAHB (faint envelope) and central helium exhaustion (bright envelope) for a set of HB models with different masses and fixed chemical composition (metal–Z=0.01–and helium–Y=0.259–mass fractions). We have assumed an α-enhanced chemical composition (Pietrinferni et al, 2006b) and a progenitor mass according to a 13 Gyr isochrone (the mass at the main sequence turn off, MSTO, is equal to 0.86 $M_{\odot}$).

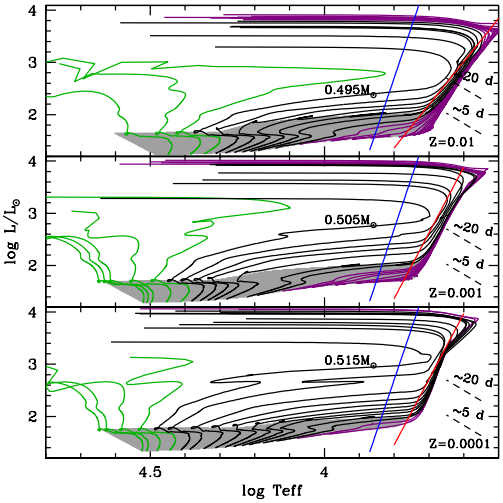

Fig. 10 Top: HRD of HB evolutionary models covering a broad range of stellar masses ($M/M_{\odot}$=0.48–0.90) and the same initial chemical composition (Z=0.01, Y=0.259). The grey area outlines the region between ZAHB (faint envelope) and central-helium exhaustion (bright envelope). The green lines display HB models evolving as AGB-manqué, black lines the post early-AGB models, and purple lines the thermal pulsing AGB models (see text for details). The almost vertical blue and red solid lines indicate the hot and cool edge of the TIIC instability strip. The minimum stellar mass (in solar units) crossing the instability strip is labelled in black. The black dashed lines show two iso-periodic lines for 5 and 20 days. Middle: Same as the top panel, but for stellar masses ranging from $M/M_{\odot}$=0.4912 to 0.80 and for a metal-intermediate chemical composition (Z=0.001, Y=0.246). Bottom: Same as the top panel, but for stellar masses ranging from $M/M_{\odot}$=0.5035 to 0.70 and for a metal-poor chemical composition (Z=0.0001, Y=0.245). Image reproduced with permission from Bono et al (2020b, Fig. 5), copyright by ESO.

The total mass along the ZAHB, as expected, decreases when moving from the red HB (RHB) to the blue HB (BHB) and further on to the extreme HB (EHB). The helium-core mass is constant along the ZAHB and is mainly fixed by the chemical composition of the progenitor ($M_c^{\rm He} = 0.4782\,M_{\odot}$) and is roughly independent of age for ages above a few Gyr. The mass of the envelope decreases from 0.4218 $M_{\odot}$ for RHB models to a few thousandths solar masses for EHB models. In an actual old stellar population with a fixed initial chemical composition, the mass lost along the RGB (more efficient when approaching the tip of the RGB; Origlia et al, 2014) determines the final mass distribution along the ZAHB.

The bright envelope of the grey area marks the central helium exhaustion, corresponding formally to the beginning of the AGB phase. The small ripples along the helium-exhaustion sequence ($\log L/L_{\odot} \sim 1.8$) show that the lower the total mass of the HB model, the hotter the effective temperature at which the helium exhaustion takes place. The luminosity of the ripples ranges from $\log L/L_{\odot} \approx 2$ in the warm region to $\log L/L_{\odot} \approx 1.6$ in the hot region of the HB. At this point, the He burning moves smoothly to a shell around the carbon-oxygen core. The overlying H-shell extinguishes, due to the expansion of the structure before reigniting later with various efficiencies, depending on the mass thickness of the envelope around the original He core.

Models with mass below $0.495\,M_{\odot}$ (corresponding to an envelope mass lower than $\sim 0.017\,M_{\odot}$) never reach the AGB location; they do not cross the instability strip and move to their WD cooling sequence, as a carbon-oxygen (CO) WD (Castellani et al, 2006; Salaris et al, 2013). These objects have been called AGB-manqué (Greggio and Renzini, 1990), and are shown as green tracks in the top panel of Fig. 10).

More massive models cross the instability strip while moving towards their AGB tracks. Models with $0.495 \leq M/M_{\odot} < 0.55$ reach the AGB, but move back towards the WD sequence (hence they cross the instability strip again but at higher luminosities) well before reaching the thermal pulse (TP) phase. They are named post-early AGB (PEAGB), and are plotted as black lines in the top panel of Fig. 10. These AGB models perform several gravo-nuclear loops in the Hertzsprung–Russell Diagram (HRD), either during the AGB phase and/or in their approach to the WD cooling sequence after leaving the AGB (during this post-AGB transition models cross again the instability strip). Some of them may take place inside the instability strip. The reader interested in a more detailed discussion concerning their impact on the pulsation properties is referred to Bono et al (1997). The evolutionary implications, and in particular the impact of the loops concerning the AGB lifetime have recently been discussed by Constantino et al (2016).

Models with $M \geq 0.54\,M_{\odot}$ (plotted as purple lines in Fig. 10) evolve along the AGB and experience the TPs. The number of TPs, and in turn the duration of their AGB phase, is once again dictated by the efficiency of the mass loss and by their residual envelope mass (Weiss and Ferguson, 2009; Cristallo et al, 2009). Calculations of TP evolution are quite demanding from the computational point of view, hence we decided to use the fast and simplified synthetic AGB technique originally developed by Iben and Truran (1978) and more recently by Wagenhuber and Groenewegen (1998) to compute the approach of these AGB models to the WD cooling sequence. In particular, the synthetic AGB modelling started for thermal-pulsing AGB (TPAGB) models just before the occurrence of the first TP, while for PEAGBs it was initiated at the brightest and reddest point along the first crossing of the HRD, towards the AGB.

The middle and the bottom panels of Fig. 10 show the same predictions, but for two more metal-poor chemical compositions. The values of the stellar masses plotted along the ZAHBs show the impact of the chemical composition. The mass range of the tracks that cross the instability strip and produce TIICs steadily decreases from

0.495–0.90 $M/M_{\odot}$ for Z=0.01, to 0.505–0.80 $M/M_{\odot}$ for Z=0.001, and to 0.515–0.70 $M/M_{\odot}$ for Z=0.0001. It is worth mentioning that the range in luminosity covered by the different sets of models is similar. The mild change in stellar mass and the similarity in luminosities suggests a marginal dependence of the mass–luminosity (ML) relation of TIICs on the chemical composition. In order to further define the theoretical framework for RVTs stars (Wallerstein, 2002; Soszyński et al, 2011), we suggest that they are the progeny of both PEAGB and TPAGB. There are two reasons supporting this hypothesis:

a) Period range – The theoretical periods for these models are systematically longer than WVs and more typical of RVTs stars. The predicted mass for these structures is uncertain because it depends on the efficiency of mass loss during the TP phase. The theoretical framework is further complicated by the fact that the number of TPs also depends on the initial mass of the progenitor and on its initial chemical composition. This means that a contribution from intermediate-mass stars cannot be excluded a priori. However, the lack of RVTs in nearby dwarf spheroidal galaxies hosting a sizable fraction of intermediate-mass stars with ages ranging from 1 Gyr to more than 6-8 Gyr, such as Carina, Fornax and Sextans (Aparicio and Gallart, 2004; Beaton et al, 2018), suggests that this channel might not be very efficient. However, RVTs have been identified in the MCs (Soszyński et al, 2008b; Ripepi et al, 2015).

b) Alternating cycle behaviour – There is evidence of an interaction between the central star and the circumstellar envelope, possibly causing the alternating-cycle behaviour (Feast et al, 2008; Rabidoux et al, 2010). The final crossing of the instability strip before approaching the WD cooling sequence either for PEAGB or for TPAGB models appears a very plausible explanation.

The above circumstantial evidence suggests that the variable stars currently classified as TIICs have a range of evolutionary properties. The BLHs and the WVs appear to be either post-ZAHB (AGB, double shell burning) or post-AGB (shell hydrogen burning) stars, whereas RVTs are mainly post-AGB objects.

3 The Hertzsprung progression

More than ninety years ago, Hertzsprung (1926) discovered that a sub-sample of Galactic classical Cepheids presents a relationship between the bump along the light curve and the pulsation period. The so-called "Hertzsprung progression" (HP) was subsequently discovered among Andromeda and MC Cepheids by Shapley and McKibben (1940), Kukarkin and Parenago (1949), and Payne-Gaposchkin (1954). The HP observational scenario was enriched by Joy (1937) and by Ledoux and Walraven (1958) who found a similar shift in the phase of the bump in radial velocity curves.

The empirical fingerprint of the HP is the following: classical Cepheids in the period range $6 < P < 16$ days show a bump along both the light and the velocity curves. This secondary feature appears on the decreasing branch of the light curve for Cepheids with periods up to 9 days, while it appears close to maximum light for $9 < P < 11$ days and moves at earlier phases for longer periods. On the basis of this observational evidence this group of variables was christened "Bump Cepheids" for avoiding to be mixed-up with "Beat Cepheids". In fact, the latter group refer to

mixed-mode variables i.e. objects in which two or more modes are simultaneously excited, and therefore both the shape of the light curves and the pulsation amplitudes change from one cycle to the next, whereas bump Cepheids are single-mode variables and their pulsation properties are characterized by a strong regularity over consecutive cycles.

A more quantitative approach concerning bump Cepheids was originally suggested by Parenago and Kukarkin (1936); Payne-Gaposchkin (1947), and more recently by Simon (1976) and by Simon and Lee (1981) who investigated the shape of the light curves by means of Fourier analysis. The latter authors found out that both the phase difference, ϕ_{21}, and the amplitude ratio, R_{21}, show a sharp minimum close to the center of the HP. Following this approach, several investigations have been already devoted to Fourier parameters of Galactic and Magellanic Cepheids. In particular, Moskalik et al (1992, hereinafter MBM) suggested that the minimum in the Fourier parameters for Galactic Cepheids takes place at P(HP) = 10.0 ± 0.5 days, while Moskalik et al (2000) by investigating a sample of more than 100 radial velocity curves, they found P(HP) = 9.95 ± 0.05 days (see also Hocdé et al, 2022, and references therein). At the same time, Alcock et al (1999) by investigating a large sample of LMC Cepheids estimated that the minimum in the Fourier parameters is located at P(HP) = 11.2 ± 0.8 days. Thus supporting the shift of the HP center toward longer periods originally suggested by Payne-Gaposchkin (1951) and strengthened by Andreasen and Petersen (1987) and by Andreasen (1988). More recently, Beaulieu (1998) suggested that the HP center in LMC and in SMC Cepheids is located at P(HP) = 10.5 ± 0.5 days and P(HP) = 11.0 ± 0.5 days, respectively. Since these three stellar systems are characterized by different mean metallicities, namely Z=0.02 (MW), Z=0.008 (LMC), and Z=0.004 (SMC), this empirical evidence suggests that a decrease in metallicity moves the HP center toward longer periods.

Up to now, two distinct models have been proposed in the literature to explain the appearance of the HP among bump Cepheids: the echo model and the resonance model. The former was suggested by Whitney (1956) and discussed by Christy (1968, 1975) on the basis of Cepheid nonlinear, radiative models. According to Christy, during each cycle close to the phases of minimum radius and before the phase of maximum expansion velocity a pressure excess is generated in the first He ionization region. This pressure excess causes a rapid expansion which, in turn, generates two pressure waves moving outward and inward. The latter reaches the stellar core close to the phase of maximum radius, then reflects and reaches the surface one cycle later causing the appearance of the bump. The resonance model was suggested by Simon (1976) and is based on linear, adiabatic periods. Within this theoretical framework, the bump would be caused by a resonance between the second overtone and the fundamental mode, and takes place when the period ratio between these two modes is close to 0.5. In particular, they suggested that the instability of the fundamental mode drives, due to a resonance, the second overtone instability. This explanation lies on the evidence that the nonlinear, radiative models constructed by Stobie (1969) show a bump along the radial velocity curves close to the resonance line $P_2/P_0 = 0.5$.

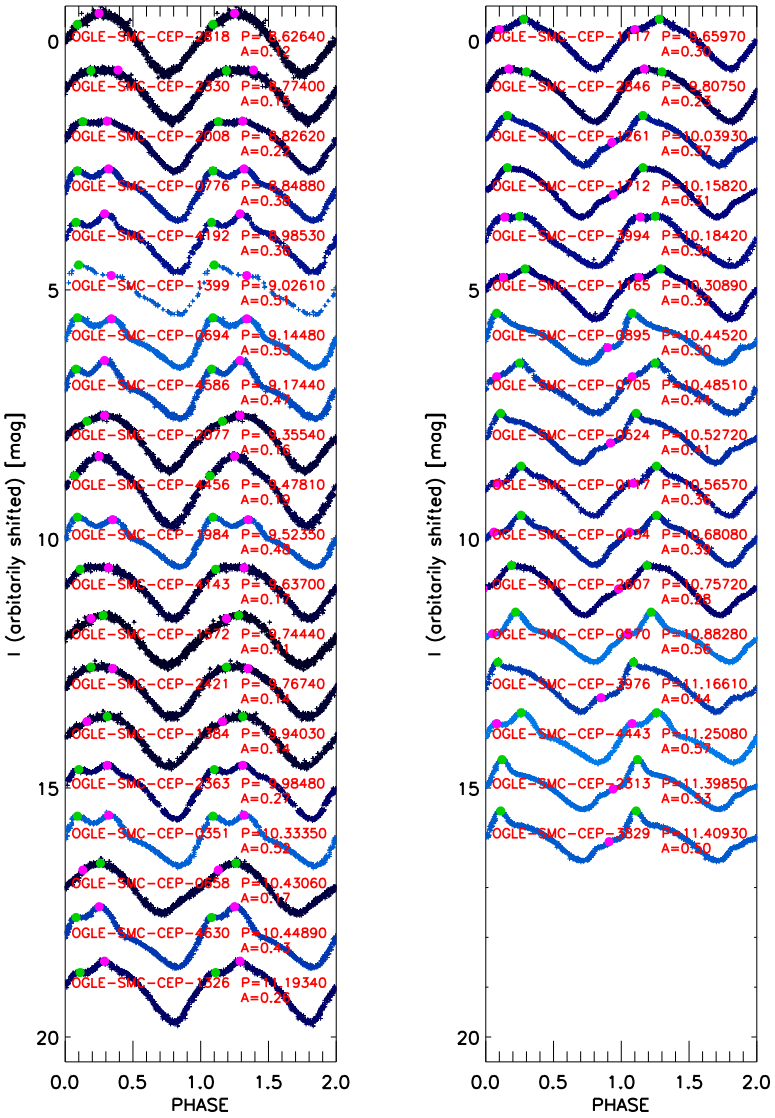

Fig. 11 Left: Phased *I*-band light curves of SMC bump Cepheids with a bump moving up along the decreasing branch (UPDB). From top to bottom, the different variables are plotted with increasing pulsation period and artificially shifted in magnitude. The position of the bump is marked with a pink circle, while the pulsation maximum is marked with a green circle. The light curves are plotted twice, so as to emphasize the changes along the pulsation cycle. The light curves are color-coded according to the luminosity amplitude. They range from light blue for the largest amplitudes to dark blue for the smallest ones. The labels on the left side show the name of the variables, whereas those on the right side display the period (days) and the *I*-band amplitude (mag). Right: Same as the left, but for SMC bump Cepheids with a bump moving down along the rising branch (DORB).

Such an extensive observational and theoretical effort devoted to bump Cepheids was not only aimed at understanding the HP, but also at providing independent estimates of both the mass and the radius of these variables. In fact, dating back to Christy (1968), Christy (1975), Stobie (1969) and Fricke et al (1972) it was suggested that these two evolutionary parameters can be constrained on the basis of period and phase of the bump. A different method to estimate the mass, based on period ratios, was suggested by (Petersen, 1973). Mass determinations based on these two methods present a compelling feature: they are based on observables, such as periods and phases of the bump, which are not affected by systematic empirical uncertainties, since they are only limited by photometric accuracy. However, pulsation masses based on these methods are, with few exceptions (Carson and Stothers, 1988), systematically smaller than the evolutionary masses. This longstanding puzzle raised the so-called bump mass discrepancy (see also Cox et al, 1980) and at the same time supported the use of a ML relation based on evolutionary models, which include either a mild or a strong convective core overshooting (Simon, 1995; Wood, 1998).

Even though the new radiative opacities settled down this long-standing problem (MBM; Kanbur and Simon 1994), recent linear (Buchler et al, 1996; Simon and Young, 1997) and nonlinear (Wood et al, 1997) predictions for MC Cepheids present a small discrepancy with the ML relations predicted by current evolutionary models.

In order to provide a new quantitative spin on the HP, we decided to take advantage of the homogeneous and accurate data set collected by OGLE-IV for both Galactic and MC Cepheids to further constrain the metallicity dependence.

Figure 11 shows the *I*-band light curves of SMC bump Cepheids. The light curves from top to bottom are plotted in order of increasing pulsation period and their colors are correlated with the luminosity amplitude. Darker colors mark low luminosity amplitude variables, whereas light blue colors mark large amplitudes. To help the eye in the identification of secondary features, the bump is marked with a pink circle, while the pulsation maximum is marked with a green circle. To properly trace the transition of the bump from the decreasing to the rising branch, the left panel only shows bump Cepheids with the bump moving UP along the decreasing branch (UPDB), whereas the right panel shows bump Cepheids with the bump moving DOwn along the rising branch (DORB). The light curves plotted in this figure display several distinctive features that are worth being discussed in detail.

a) The phase of the maximum among the UPDB Cepheids (left panel) is quite constant and equal to $\phi \sim 0.1$[6], while the phase of the bump steadily approaches the phase of the maximum light when moving from shorter (top) to longer-period (bottom) bump Cepheids.

b) The bump in UPDB Cepheids with periods shorter than ∼9 days is fainter than the pulsation maximum, while for periods of the order of ∼9.3–9.5 days it attains magnitudes similar to the pulsation maximum and it becomes the main maximum at longer periods. The variation in the shape of the light curve is far from being smooth, indeed UPDB Cepheids with low luminosity amplitudes have light curves that have

[6]The current light curves were phased by using as reference epoch the phase along the rising branch in which the magnitude of the light curve is equal to the mean magnitude of the object (Inno et al, 2013).

been defined as "flat topped" , i.e. with a luminosity maximum characterized by two secondary maxima.

c) The center of the HP is located at periods of P(HP)=9.8±0.2 days, in which the UPDB Cepheids attain a well-defined minimum in luminosity amplitude (A(I)~0.15 mag). The light curve of these variables is more sinusoidal, almost featureless, with the bump showing up either as a small secondary maximum along the rising branch, or a change in the slope along the rising branch. To improve the identification of the bump in these variables we also took advantage of the OGLE-IV V-band light curves.

d) The light curves of DORB Cepheids (right panel) show, as expected, an opposite trend. Close to the minimum in luminosity amplitudes, the light curves of UPDB and DORB Cepheids are similar. The phases of the maximum are once again quite constant, and take place around phases ϕ=0.1–0.2. However, the phase of the bump steadily approaches the phase of the minimum in luminosity when moving from shorter to longer period DORB Cepheids.

e) The variation of the light curve among LMC bump Cepheids (see Fig. A1 in Appendix) is similar to SMC bump Cepheids (Fig. 11). The key difference is that the center of the HP occurs at shorter periods, namely P(HP)~ 9.4±0.2 days. In this period range, the luminosity amplitude is smaller than 0.2 magnitudes, with a well-defined minimum for the Cepheid 2252 with A(I)~0.1 mag. There are a few exceptions concerning the shape of the light curve, but the global trend is well defined among both UPDB and DORB Cepheids.

f) The similarity in the variation of the light curves across the HP also applies to Galactic bump Cepheids (see Fig. A1 in Appendix). The center of the HP is located at even shorter periods P(HP)~ 9.0 ± 0.2 days and I-band luminosity amplitudes of the order of 0.25 magnitudes.

The reader interested in a more quantitative discussion concerning the metallicity dependence of the HP is referred to section A in Appendix.

4 Magellanic Cepheids and the color–magnitude diagram

Optical, NIR and MIR photometric surveys of the MCs provide the unique opportunity to investigate the Cepheid distribution across the CMD. The main reason why the MCs play a crucial role in quantitative Astrophysics is mainly that we can, as a first approximation, assume that the MC stellar populations are all placed at the same distance, i.e., by neglecting the depth effect. Data plotted in Fig. 12 display the distribution of SMC (left) and LMC (right) Cepheids in the optical I,$V-I$ CMD. Different groups of variable stars are plotted with different symbols, while variables pulsating in different modes are plotted with different colors. Common stars are plotted as grey dots. Data for both static and variables stars come from the OGLE IV data set. Helium-burning variable stars are situated, as expected, between the main sequence and the red giant branch in the so-called Hertzsprung gap. They typically attain magnitudes either brighter (CCs, TIICs) or similar (ACs) to red clump stars, the stellar over-density located in the SMC at I ~18.55–18.65 mag and $V-I$ ~0.90–0.95 mag and in the LMC at I ~18.25–18.35 mag and $V-I$ ~1.00–1.05 mag. The mean

magnitude of the variable stars was estimated as a mean in flux over the entire pulsation cycle, and then transformed into a mean magnitude. Variables placed outside the well-defined, almost vertical, variable sequences are either affected by differential reddening or by blending (crowded regions). A glance at the data plotted in this figure clearly show that optical CMDs can be adopted to validate variable identification, but they are far from being an optimal diagnostic to identify different groups of variable stars, since the different Cepheid groups overlap both in magnitude and in color.

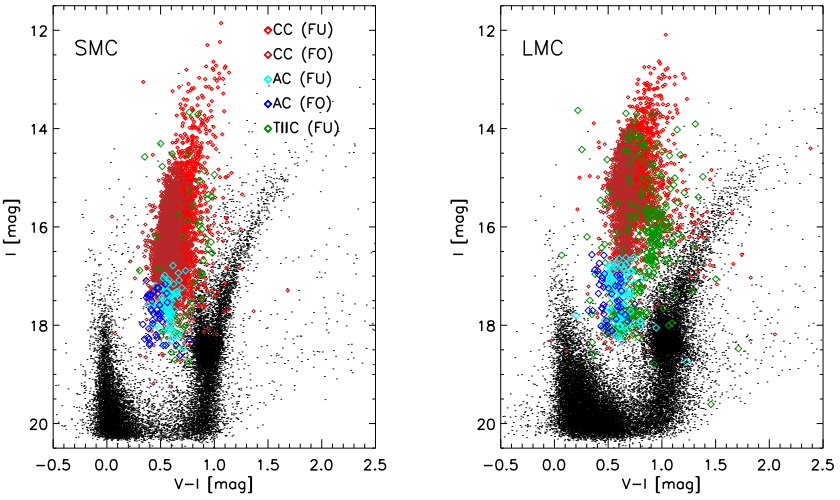

Fig. 12 Left: distribution of fundamental (light red) and first overtone (dark red) CCs, fundamental (light blue) and first overtone (dark blue) ACs and fundamental (green) TIICs in the optical I,$V-I$ CMD of the SMC. Field SMC stars are plotted as grey dots. The optical CMD shows different triple regions, i.e. regions in which the three different groups of variables overlap. Data plotted in this panel come from the OGLE IV data set. The mean magnitudes of variable stars were estimated with a fit of the light curves. Right: Same as the left, but for LMC Cepheids.

In order to find out more about the global properties of Magellanic CCs, the right panel of Fig. 13 shows the comparison between theory and observations in the optical dereddened I_0, $(V-I)_0$ CMD for LMC CCs. The symbols are the same as in Fig. 12, individual reddenings for CCs were estimated by using the reddening map provided by Skowron et al (2021), while common stars were dereddened through a mean reddening of E($V-I$)=0.100 mag (Skowron et al, 2021). The solid lines with different colors display stellar isochrones from the BASTI-IAC database at fixed chemical composition ([Fe/H]= −0.30, iron abundance; Y=0.252, helium mass fraction) and ages ranging from 40 to 300 Myrs (see labelled values). Stellar isochrones are based on evolutionary models, constructed by assuming a scaled-solar chemical mixture and by neglecting convective core overshooting. They were plotted by assuming a true distance modulus of $\mu = 18.477 \pm 0.023$ mag (Pietrzyński et al, 2019).

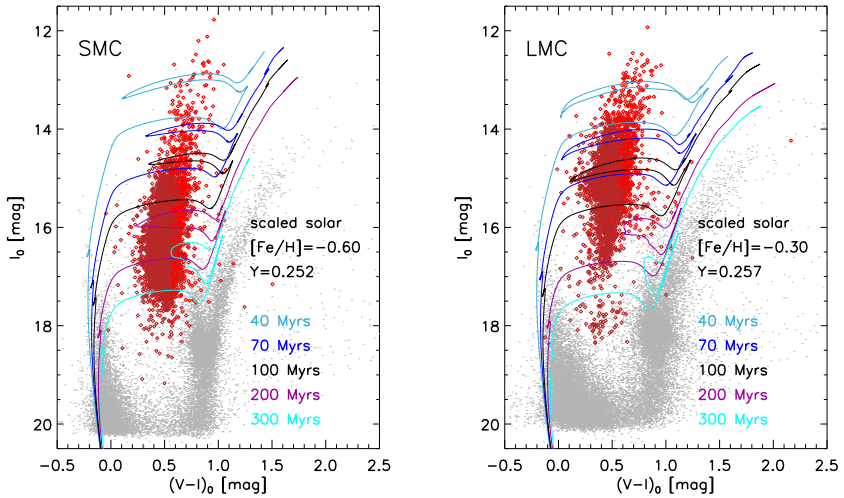

Fig. 13 Left: Comparison between theory and observations in the dereddened $I_0, (V-I)_0$ CMD for SMC CCs. CCs are marked with light (fundamental) and dark (first overtone) red symbols, while static stars with grey dots. Variable stars were dereddened by using the reddening map provided by Skowron et al (2021), while static stars were dereddened through a mean reddening of E($V-I$)=0.047 mag (Skowron et al, 2021). Solid lines display selected scaled-solar stellar isochrones from the BASTI-IAC database at a fixed chemical composition ([Fe/H]= −0.60, Y=0.252) and ages ranging from 30 to 300 Myrs (see labelled values). Isochrones were plotted by assuming a true distance modulus of $\mu = 18.977 \pm 0.028$ mag (Graczyk et al, 2020). Right: Same as the left, but for LMC CCs and more metal-rich scaled-solar stellar isochrones ([Fe/H]= −0.30, Y=0.257). Isochrones were plotted by assuming a true distance modulus of $\mu = 18.477 \pm 0.023$ mag (Pietrzyński et al, 2019). The mean reddening adopted for static stars is E($V-I$)=0.100 mag (Skowron et al, 2021).

Detailed comparisons between theory (evolutionary and pulsation properties) concerning MC variable stars have been widely discussed in the literature (Cioni et al, 2014; Soszyński et al, 2017a; Ripepi et al, 2016). Here we are mainly interested in providing a global picture of their properties. The agreement between theory and observations is quite good over the entire mass/age range. Indeed, the width in color of the blue loops (central helium burning phases) takes globally into account the observed distribution of CCs inside the instability strip. However, this pending issue requires more detailed investigations, since the extension in temperature of the blue loop depends on many different physical assumptions (Bono et al, 2000b) and we still lack quantitative constraints on the impact that input physics (opacities, equation of state), mass loss (Maeder and Meynet, 2000; Marengo et al, 2010; Barmby et al, 2011), rotation (Maeder and Meynet, 2000; Costa et al, 2019) and extra-mixing have on these evolutionary phases. The current theoretical framework also takes into consideration young MS stars (central hydrogen burning phases), and RGB stars (shell hydrogen burning phases).

The left panel of Fig. 13 shows the same comparison, but for SMC CCs. The solid lines display BASTI-IAC scaled-solar stellar isochrones at fixed chemical composition ([He/H]= 0.60, Y=0.257) and different ages (see labelled values). Isochrones were plotted by assuming a true distance modulus of $\mu = 18.977 \pm 0.028$ mag

(Graczyk et al, 2020). The mean reddening adopted for static stars is E($V-I$)=0.047 mag (Skowron et al, 2021). The agreement between theory and observations is once again quite good over the entire mass/age range.

The difference between stellar isochrones based on evolutionary models which either neglect or take into account convective core overshooting during core hydrogen-burning phases have been widely discussed in the literature. The main difference is that the isochrones taking into account overshooting are systematically brighter than canonical isochrones. This means that individual Cepheid ages estimated by using the former set are systematically younger than those based on the latter one. Moreover, the extent in temperature/color of the blue loops associated with canonical and overshooting isochrones is different: the former ones are on average larger. Once again, the morphology of the blue loops depends on a variety of micro and macro physics phenomena and we still lack firm theoretical predictions concerning who is doing what. Note that stellar isochrones were downloaded from the new BASTI-IAC database (http://basti-iac.oa-abruzzo.inaf.it).

However, in some specific cases, like the comparison between theory and observations for the MC CCs, the resolution in mass of the BASTI-IAC evolutionary tracks was improved, and in turn, we also re-computed stellar isochrones.

4.1 Anomalous Cepheids

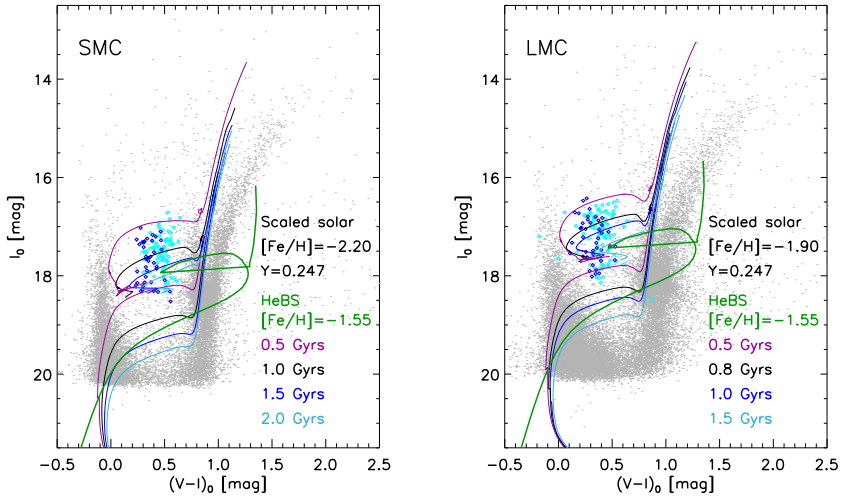

Fig. 14 Left: Comparison between theory and observations in the dereddened $I_0, (V-I)_0$ CMD for SMC ACs. ACs are marked with light (fundamental) and dark (first overtone) blue symbols, while static stars with grey dots. Color-coded lines show stellar isochrones from the BASTI-IAC database at fixed chemical composition ([Fe/H]= −2.20, Y=0.247) and stellar ages ranging from 0.5 Gyr to 2 Gyr (see labelled values). The green line shows the helium-burning sequence (HeBS) for a more metal-rich ([Fe/H]= −1.55, Y=0.248) chemical composition. Right: Same as the left, but for LMC ACs and more metal-rich stellar isochrones ([Fe/H]= −1.90, Y=0.247).

The right panel of Fig. 14 shows the comparison between theory and observations for LMC ACs. The LMC ACs and the static stars were dereddened following the same approach adopted for LMC CCs. The solid lines display stellar isochrones from the BASTI-IAC database at fixed chemical composition ([Fe/H]= −1.90, Y=0.247) and ages ranging from 0.8 to 2 Gyr (see labelled values). Stellar isochrones are based on evolutionary models constructed assuming a scaled-solar chemical mixture and by neglecting convective core overshooting and they were plotted by assuming a true distance modulus of $\mu = 18.477 \pm 0.023$ mag (Pietrzyński et al, 2019). A glance at the data plotted in this panel brings forward two interesting features worth looking into.

a) Metallicity distribution – The faint tail ($m_I \lesssim 18.7$ mag) of LMC ACs is quite metal-poor. The current comparison suggests a mean iron abundance of the order of [Fe/H]=–1.9/–2.0, while the bright tail is less metal-rich than [Fe/H]= −1.55, as suggested by the more metal-rich helium-burning sequence (green line). The upper limit is quite well known and fixed by the evidence that helium-burning loci for more metal-rich chemical compositions attain effective temperatures (colors) that are systematically hotter (bluer) than the Cepheid instability strip (Monelli and Fiorentino, 2022).

b) Luminosity function – There is evidence that both the I- and the V-band luminosity function of LMC ACs shows a well-defined minimum, or a zone of avoidance for $m_I \approx 18.75$ mag. It is not clear whether this feature might be associated with a difference in their origin (binary merging versus single star evolution, Fiorentino and Monelli, 2012). The current evidence indicates that stellar systems mainly dominated by old stellar populations (Tucana, Cetus, Sculptor, LGS3) host ACs which are on average 1.0–1.5 mag brighter than RRLs (Monelli and Fiorentino, 2022). Moreover, the bright tail of the ACs shows up in stellar systems showing multiple star formation episodes and a well sampled intermediate-age stellar population (MCs). This working hypothesis requires more quantitative constraints on the possible difference between faint and bright ACs.

The left panel of Fig. 14 shows the same comparison as the right panel, but for SMC ACs. The stellar isochrones were computed at fixed chemical composition ([Fe/H]= −2.20, Y=0.247) and the stellar ages are labelled. The global properties of the SMC ACs appear to be quite similar to LMC ACs. They only cover a narrower range in magnitudes and FO ACs also cover a narrower range in period. The comparison between the LMC and the SMC luminosity function for ACs indicates that the bright tail appears less extended. This suggests a minor contribution in the younger (more massive) range.

4.2 Type II Cepheids

The right panel of Fig. 15 shows the comparison between theory and observations for the LMC TIICs following the same approach adopted for CCs and ACs. However, the solid lines display HB evolutionary models computed with an α-enhanced chemical mixture, at fixed chemical composition ([Fe/H]= −1.55, Y=0.246) and stellar masses ranging from 0.51 $M/M_\odot$ to 0.60 $M/M_\odot$ (see labelled values). Predictions plotted in this panel display that the bulk of TIICs are AGB stars (hydrogen and helium shell burning). The reader interested in a more detailed discussion concerning the three

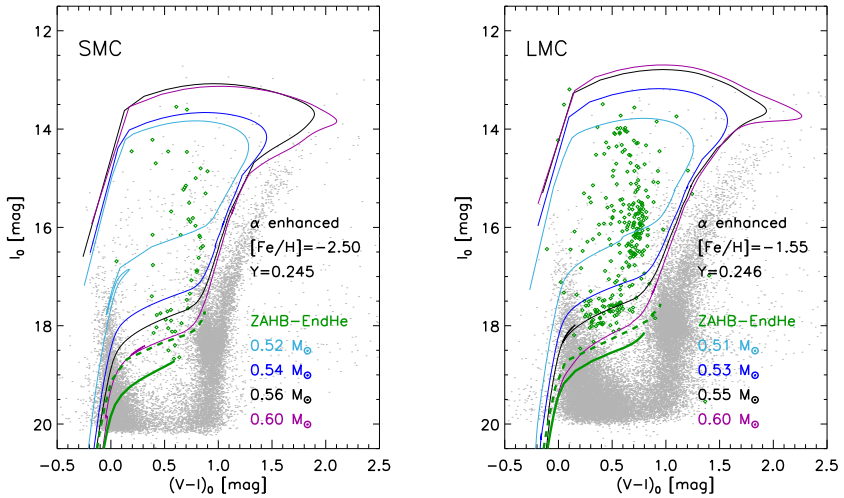

Fig. 15 Left: Comparison between theory and observations in the dereddened $I_0, (V-I)_0$ CMD for SMC TIICs. TIICs are marked with light (fundamental) green symbols, while static stars with grey dots. Solid lines display selected HB evolutionary models from the BASTI-IAC database with a α-enhanced chemical composition ([Fe/H]= −2.50, Y=0.245) and stellar masses ranging from 0.51 $M/M_{\odot}$ to 0.60 $M/M_{\odot}$ (see labelled values). The thick green lines show the Zero Age Horizontal Branch (ZAHB) and the dashed line the end of core helium burning. Right: Same as the left, but for LMC TIICs and more metal-rich HB evolutionary models ([Fe/H]= −1.55, Y=0.246).

different subgroups (BL Herculis, W Virginis, RV Tauri) is referred to Bono et al (2020b) and to Braga et al (2020). The solid and the dashed green lines plotted in the same panel show the ZAHB and the core helium exhaustion. They enclose the region of the CMD, in which the bulk of the RRLs are expected to be located. Clearly, this is a mere simplification, because LMC RRLs cover a broad range in metallicity (Gratton et al, 2004; Skowron et al, 2016) and a significant overlap in the CMD is expected between these two different groups of variable stars.

The left panel of Fig. 15 shows the same comparison as the right panel, but for SMC TIICs. The solid lines display similar HB evolutionary models, but computed by assuming a more metal-poor chemical composition ([Fe/H]= −2.50, Y=0.245). The global agreement is once again quite good over the entire magnitude and color range.

5 Diagnostics to estimate individual Cepheid distances

More than one century ago, Henrietta Leavitt discovered that Cepheids obey to well-defined Period Luminosity (PL) relations. The key advantage of these relations is that they are linear over the entire period range. This outcome applies to optical, NIR and MIR regime.[7] There are a number of pros and cons in using similar diagnostics

[7] RRLs obey to PL relations only for wavelengths longer than the R bands (Bono et al, 2001; Braga et al, 2015) in the visual band they obey to a mean absolute visual-magnitude metallicity relation.

in different wavelength regimes. The reader interested in a detailed empirical discussion concerning the improvements in moving from the optical to the NIR regime is referred to the seminal papers by McGonegal et al (1982, 1983) and McAlary et al (1983). In the following, we will outline the most relevant cons.

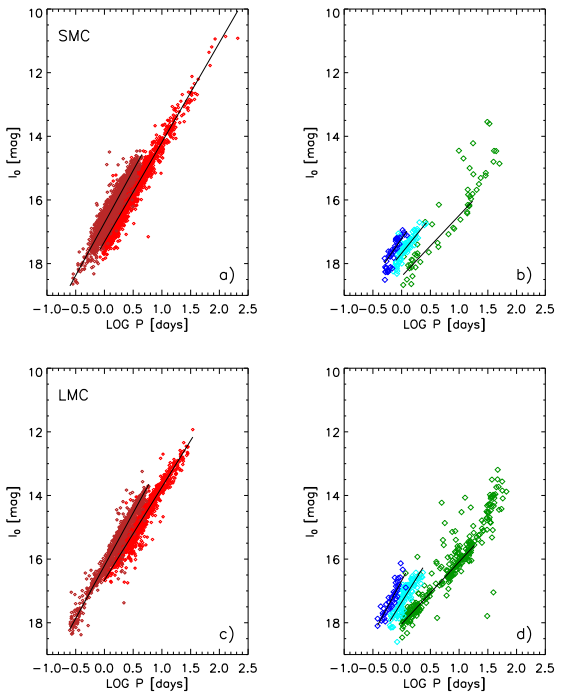

Fig. 16 Panel a): dereddened *I*-band PL relations for SMC CCs. From shorter to longer periods, the different symbols display FO (dark red) and fundamental (light red) CCs. The solid black lines display the linear fits to the PL relations (see Table B1). Panel b): Same as the left, but for FO (dark blue) and FU (light blue) ACs and FU (green) TIICs. The black lines display the linear fits to the PL relations (see Table B1). Panels c) and d): Same as the top, but for LMC Cepheids. Note the increase in sample size of TIICs.

i)–Luminosity amplitude– The identification and characterization of regular variables is significantly easier in the optical regime, because the luminosity amplitude in the *B*-band is typically a factor of three-to-five larger than in the NIR and MIR bands. This means that period determination and mode identification are more straightforward.

ii)–Time series– Optical measurements, thanks to linearity, pixel scale and the size of current CCDs are less demanding about telescope time than NIR measurements.

iii)–Limiting magnitude– Current ground- and space-based observing facilities allow us to identify and characterize CCs and TIICs in the optical regime not only in Local Group ($d \lesssim 1$ Mpc), but also in Local Volume ($d \sim 25$ Mpc) galaxies (Freedman and Madore, 2010; Riess et al, 2021). The limiting magnitudes in the NIR regime are

systematically brighter, but JWST and ELTs are going to open new paths (Fiorentino et al, 2020). There are also some indisputable pros.

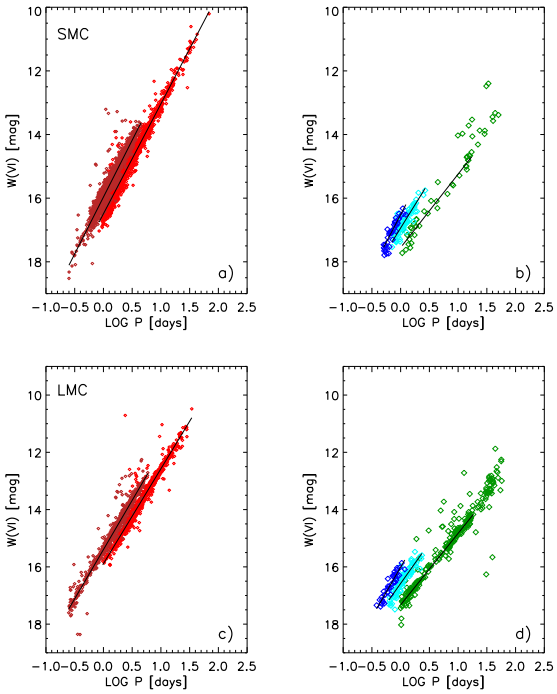

Fig. 17 Top: Optical $I,V-I$ PW relations (see Table B2) for SMC CCs (panel a) and for ACs plus TIICs (panel b). Symbols and color coding are the same as in Fig. 16. Bottom: Same as the top, but for LMC Cepheids (CCs, panel c; ACs plus TIICs, panel d).

i)–Reddening correction– Optical bands are more prone to systematics concerning the reddening correction than NIR bands. The ratio between selective absorption in the K and in the V band is, according to current reddening law (Cardelli et al, 1989), of the order of 0.12. This means that measurements in the K-band are roughly one order of magnitude less affected by reddening uncertainties than the ones in the V-band.

ii)–Shape of the light curves– The shape of the light curves in the optical regime is affected by both temperature and radius variation. This means that light curves in the optical regime might display, according to the pulsation period and the luminosity amplitude, sharp rising branches and cuspy maxima/minima. The shape of the light curves in the NIR and in the MIR regime are mainly dominated by radius variations and they are typically more sinusoidal. This is the main reason why the light curve templates provide very accurate estimates of the mean NIR magnitudes even with a single measurement, once the period, the luminosity amplitude and the reference epoch are known (Inno et al, 2015). In case three independent measurements are

available, the mean magnitude can be estimated once the period and the luminosity amplitude are known (Inno et al, 2015; Braga et al, 2019).

iii)–Slope of the PL relation– The slope of the PL relations becomes systematically steeper when moving from the optical to the NIR regime. This means that NIR PL relations are, at fixed pulsation period, more accurate than optical ones. In this context, it is worth mentioning that the luminosity amplitudes becomes almost constant at wavelengths longer than the K-band, and the same outcome applies to the slope of the PL relations. The approach to a constant value is due to the fact that luminosity variations are mainly dominated by radius variations.

iv)–Width in temperature of the Instability Strip– Radial variables obey to PLC relation. The use of the PL relation for the estimate of individual distances rely on the assumption that the width in temperature of the instability strip can be neglected. This assumption is quite severe in the optical regime, because optical bands are more affected by a variation in intrinsic parameters and in metal content when compared with NIR bands. The physical reason for this variation is mainly in the bolometric correction (BC). The BC in the optical regime is almost constant when moving from the blue to the red edge of the instability strip, while in the NIR regime it increases. This means that regular variables in the NIR become intrinsically brighter when moving from hotter (shorter periods) to cooler (longer periods) variables. The consequence of this difference is that the cosmic variance (standard deviation) of the V-band CC PL relation is, on average, a factor of two to three larger than in the K-band (McGonegal et al, 1982; Inno et al, 2016). This is the reason why individual distances based on V-band PL relations need to be cautiously treated, since they are more affected by possible systematics affecting the completeness of the sample over the entire period range covered by the PL relation (Bono et al, 1999a).

5.1 Fundamental versus overtone PL relations

The use of overtone variables brings forward several key advantages when compared with fundamental variables.

i)–Width in temperature of the Instability Strip– Overtones approach a stable limit cycle in a region of the instability strip that is at least a factor of two narrower than fundamental variables. This means that the PL relations provide individual distances that are more accurate than distances based on fundamental PL relations, because the dependence on the mean temperature is milder (Bono et al, 1999a).

ii)–Comparison between theory and observations– Overtone variables are systematically hotter than fundamental variables. This means that predicted pulsation properties are less prone to uncertainties affecting the treatment of convective transport.

However, overtones are also affected by two cons.

i)–Identification– Overtone variables are characterized by more sinusoidal light curves due to the presence of a nodal line (Bono et al, 2000c). This means that they have on average smaller amplitudes, and in turn, they need very accurate time series to be identified. Moreover, the shape of their light curves can be misidentified with eclipsing binaries.

ii)–Absolute calibration– Till a few years ago, the number of CCs pulsating in the first overtone known in the MW was quite limited. An accurate geometrical distance was only available for Polaris (Evans et al, 2002). Fortunately, the current status concerning first overtone Cepheids rapidly improved (Ripepi et al, 2019; Breuval et al, 2020). It is not clear yet whether the same outcome applies to Galactic single-mode second overtones.

5.2 PL versus PW relations

Almost half a century ago, van den Bergh (1975) and Madore (1982) introduced the so-called Wesenheit[8] magnitude, a pseudo magnitude that is reddening free by construction. Given two generic photometric bands (ξ, χ) it can be defined as:

$W(\chi,\xi\text{-}\chi)= \chi - [A_\chi / A_\xi - A_\chi] \times(\xi\text{-}\chi)$

where the coefficient in square parentheses only depends on the adopted reddening law. Therefore, if we assume that the reddening law is universal, we can easily define a pseudo magnitude that is independent of reddening. The use of the Wesenheit magnitudes has several indisputable advantages.

i)–Individual reddenings– CCs are young stars which trace the spiral arms of the thin disk (Medina et al, 2021). Moreover, they are quite often still embedded in the relics of the giant molecular cloud from which they originated (Genovali et al, 2014). This means that they are either reddened or highly reddened. This limitation applies not only to Galactic Cepheids, but also to CCs in nearby galaxies. The use of the Wesenheit magnitudes overcome the difficulty of individual reddening estimates/measurements.

Data plotted in Fig. 16 and in Fig. B10 (Appendix) display the dereddened *I*- and *K*-band PL relation. To overcome the overlap among different groups of variable stars the top left panel shows the *I*-band PL relations for FO (dark red) and FU (light red) SMC CCs, while the top right panel shows the PL relations for SMC ACs (FO, dark blue; FU, light blue) and SMC TIICs (FU, green). The bottom panels display the same data, but for LMC Cepheids. The coefficients of the PL relations plotted in this figure are listed in Table B1 (Appendix). A few highlights concerning observed optical-NIR PL relations.

a)– Difference in standard deviation – Optical and NIR PL relations for LMC Cepheids have, at fixed pulsation period, systematically smaller standard deviations. The difference is due to the fact that the LMC is almost face-on, while the SMC is elongated along the line of sight (Inno et al, 2015; Jacyszyn-Dobrzeniecka et al, 2016, and references therein).

b)– AC number counts – The LMC is roughly one order of magnitude more massive than the SMC ($\sim 2\times10^{11}$ Shipp et al 2021 vs $\sim 3\times10^{10}$ $M_\odot$, Besla et al 2016). However, the number of ACs differ at the 20% level (146 vs 122). The modest difference in the AC number counts is mainly due to evolutionary effects: the SMC is, on average, more metal poor, and in turn, the probability to produce ACs increases.

c)– TIICs number counts – The number of SMC TIICs is almost six times smaller than LMC TIICs. It is worth mentioning that dwarf galaxies, typically, do not host TIICs. The Sagittarius dSph (Soszyński et al, 2011) and the MCs are exceptions, and

[8] Wesenheit is a German word used by philosophers and its meaning is "essence".

their occurrence seems the consequence of the total mass and/or of their dynamical evolution (Bono et al, 2020b; Braga et al, 2020; Neeley et al, 2021). The difference between the number counts of SMC and LMC TIICs seems to be the consequence of the difference in total mass, and in particular, in the mass fraction of old stellar populations. The SMC hosts a single GC (NGC 121), while the LMC hosts more than a dozen GC (van den Bergh, 2006).

ii)–Color information– The Wesenheit magnitude takes into account the color information. Thus the PW relations are also pseudo PLC relations (Bono et al, 1999b). The main difference is that the color coefficient is fixed by the adopted reddening law and not as a least squares solution of a three-dimensional relation among periods, magnitudes and colors. The reason why the intrinsic dispersion of the PW relations is smaller than the standard deviations of the associated PL relations is also due to the use of color information. Periods, magnitude and colors provide a more accurate location of individual Cepheids inside the instability strip. Figures 17 and 18 show the key advantage in using optical, NIR and optical–NIR Wesenheit magnitudes for estimating individual Cepheid distances. The standard deviation decreases, on average, by a factor of two to 20/30% in the NIR and in the optical-NIR regime.

iii)–Triple band– Wesenheit magnitudes can be defined on the basis of two magnitudes, but this means that magnitude and color are correlated. The use of a Wesenheit pseudo magnitude based on three different bands overcome this limitation. Moreover, the use of three bands brings forward a key advantage. Optical/NIR/MIR magnitude and colors have opposite trends concerning the metallicity dependence. Therefore, appropriate combinations of magnitude and colors might be, within the errors, either independent of, or minimally affected by the metal content. There are two key drawbacks in using the Wesenheit pseudo magnitudes.

a)–Universality of the reddening law– The current empirical and theoretical evidence indicates that the reddening law changes in stellar systems that experienced different chemical enrichment histories (Calzetti et al, 2021). However, the use of either optical-NIR or optical-MIR magnitudes has the key advantage that the coefficients of the color term are tracing the derivative of the reddening law rather than "local" value (Marconi et al, 2015; Braga et al, 2015; Bono et al, 2019).

b)–Accuracy of mean colors– The observing strategy of long-term photometric surveys is mainly based on a single band photometric survey. This band is used to identify and characterize the variables. The number of measurements in the companion band(s) is more limited, and in some cases they do not uniformly cover the entire pulsation cycle. As a consequence, mean colors are affected by photometric errors that are slightly larger than the repeatability errors.

5.2.1 Highlights concerning observed optical-NIR PL and PW relations

The current empirical evidence indicates that PL and PW relations for CCs are linear over the entire period range. However, there is a vast literature concerning the possible occurrence of non-linearity in PL, Period-Color (PC) and Amplitude-Color relations of CCs based on mean magnitudes (Ripepi et al, 2022b). The same outcome applies to predicted (Das et al, 2020) and observed (MW, MC) diagnostics at maximum and minimum light (Kanbur et al, 2007). More specifically, Ngeow and

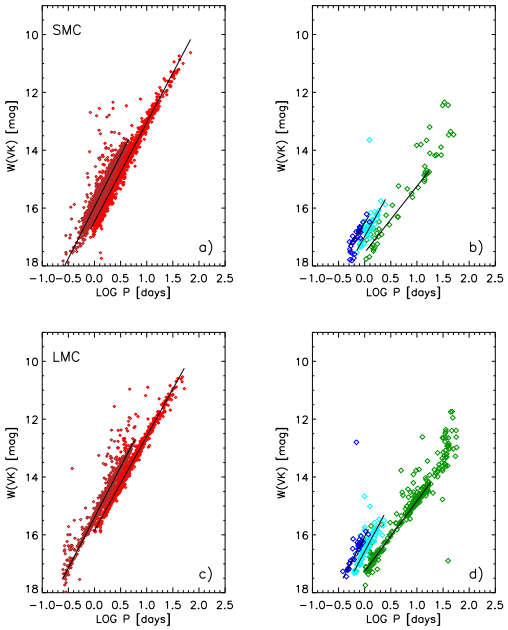

Fig. 18 Top: Optical–NIR K,$V-K$ PW relations (see Table B2 (Appendix)) for SMC CCs (panel a) and for ACs plus TIICs (panel b). Symbols and color coding are the same as in Fig. 16. Bottom: Same as the top, but for LMC Cepheids (CCs, panel c; ACs plus TIICs, panel d).

Kanbur (2005, 2006) by using optical (OGLE, MACHO) and NIR (2MASS) mean magnitudes found that LMC CCs display either a break or a non–linearity for periods around 10 days. They both adopted a chi-squared test and an F-test and found that V,R,J,H PL relations show evidence of non-linearity for P≈10 days, whereas the K-band PL relation appear to be consistent with a single-line regression.

A similar investigation was also performed by Subramanian and Subramaniam (2015) by using optical (V,I) band photometry provided by OGLE to investigate the PL relations of SMC Cepheids. They found that optical PL relations of both FU and FO CCs show a break for periods around 2.95 days and around 1 day, respectively. These findings were supported and complemented by Bhardwaj et al (2016b,a) using optical (V,I; OGLE) and NIR (J,H,K Macri et al, 2015) photometry and several robust statistical tests. They found that optical PL, PW and PC relations for LMC FU CCs are non-linear at periods around 10 days, while the NIR PL and the optical-NIR, triple band PW relations are non-linear around 18 days. Furthermore, they found that PL, PW and PC relations for FO CCs display a significant change in the slope for periods around 2.5 days only at optical wavelengths. More recently, Ripepi et al (2022b) provided a variety of PL and PW relations for LMC CCs, by using data collected by the VISTA NIR survey of the MCs, they found for the first time a break for FO CCs at periods of 0.58 days. The reader interested in a more detailed discussion addressing theoretical and empirical evidence concerning breaks in PL relations and multi-phase relations is referred to Kurbah et al (2023)

A few general considerations in dealing with this wealth of empirical evidence. Photometric accuracy and completeness are two major issues which can affect the slope of both PL/PW relations. Fortunately, long-term photometric surveys (OGLE, Gaia) and space photometry (HST Riess et al, 2019) are providing complete and accurate samples. However, we still lack accurate estimates of the star formation episodes during the last 300 Myr in the MCs. Moreover, spectroscopic surveys are still lagging, and we also lack accurate estimates of the impact that chemical composition, and in particular iron abundance, has on the slope of the PL/PW relations. Moreover, Soszyński et al (2015a) suggested that the cleaning of the sample is a possible source of systematics in the identification of break(s) in PL relations. He found that a solid identification of ACs among SMC Cepheids significantly reduces the evidence of a break for periods around 2.5 days among SMC FU CCs.

This is the case in which the use of the Occam's razor can help in dealing with this heuristic hypothesis. This precaution is supported by evolutionary models: there is agreement on the evidence that the slope of the mass–luminosity relation does not change, at fixed chemical composition, for stellar masses typical of CCs (Bono et al, 2000b; Anderson, 2002; De Somma et al, 2021).

The lively discussion concerning the linearity of PL/PW relations of CCs does not apply to TIICs, indeed, the RV Tauri (long-period TIICs) appear to be in the optical regime, at fixed pulsation period, brighter than expected on the basis of the global PL relation. The difference is still present, but reduced in the NIR regime and in the $I,V-I$ PW relation. This issue has been widely discussed in the literature (Matsunaga et al, 2006; Soszyński et al, 2018; Ripepi et al, 2014; Bhardwaj, 2022). In order to overcome these difficulties, in the estimate of both PL and the PW relations, we only included TIICs with periods shorter than 20 days.

Interestingly enough, data plotted in Fig. 16 and in Fig. B10 (Appendix) display that SMC ACs pulsating in the FO appear to be for $\log P \sim -0.30$ (short period tail) systematically fainter than expected, according to the slope of the PL relation. The same outcome applies to short period FU ACs, but the difference is smaller. On the other hand, LMC ACs show a well-defined slope over the entire period range.

The evidence that the change in SMC FO ACs occurs both in optical (V,I) and in NIR (J,K) PL/PW relations further supports that it is intrinsic. In order to detect the possible occurrence of a change in the slope, we computed the PL and the PW relations, while neglecting the short period tail, and we found that the slopes are significantly shallower (see Tables B1 B2 (Appendix) and Figs. 20, 21). The current data do not allow us to constrain whether the difference is caused by a difference in chemical compositions and/or in the ML relation.

The difference among optical, NIR and optical-NIR PW relations listed in Table B2 (Appendix) and plotted in Figs. 17 and 18 are mainly due to the adopted color index, and to the coefficient of the color index. Optical-NIR colors cover a broad range in wavelength, this means a larger sensitivity in temperature. The range in $V-K$ color of LMC CCs is, on average, a factor of 2.5 larger than the range in $J-K$ color. The use of optical–NIR magnitudes provides the unique opportunity to use color coefficients in the Wesenheit magnitudes smaller than one, therefore limiting possible uncertainties in the adopted mean colors.

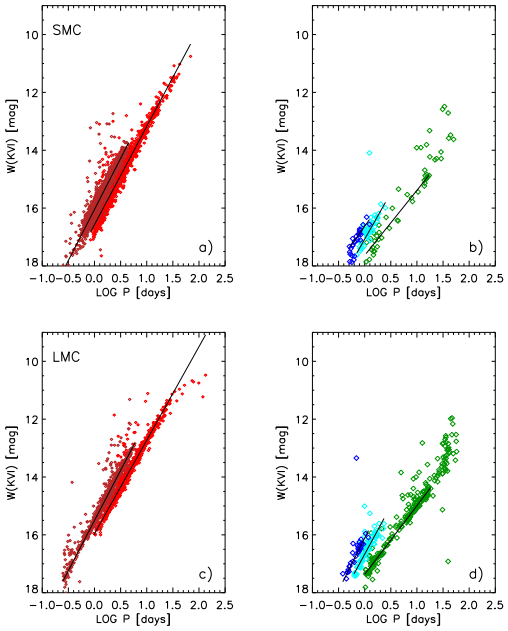

Fig. 19 Top: Optical–NIR, triple-band $K,V-I$ PW relations (see Table B2 (Appendix)) for SMC CCs (panel a) and for ACs plus TIICs (panel b). Symbols and color coding are the same as in Fig. 16. Bottom: Same as the top, but for LMC Cepheids (CCs, panel c; ACs plus TIICs, panel d).

5.3 Global trend in the slopes of PL and PW relations

In order to investigate on a more quantitative basis, the use of the triple-bands in the definition of the Wesenheit pseudo magnitude, Fig. 19 shows the $K,V-I$ PW relations for Cepheids in the Magellanic Clouds. The key advantage in using this optical-NIR diagnostic is three-fold. *a)*– The mean K-band magnitude is minimally affected by reddening. *b)*– The $V-I$ color has a good sensitivity to the effective temperature. *c)*– The standard deviation is slightly smaller when compared with similar optical-NIR PW relations (see Table B2 (Appendix)).

The current optical (OGLE-IV) and NIR (priority: VISTA (Cioni et al, 2011), secondary: IRSF (Ita et al, 2004), both converted to the 2MASS system by using the transformations provided by Kato et al (2007); González-Fernández et al (2018)) photometric data sets for Magellanic variables allow us to investigate on a more quantitative basis several interesting features of the PL relations.

Data plotted in panel a) of Fig. 20 show the slopes of both optical (V,I) and NIR (J,H,K) PL relations by using the same SMC fundamental variables plotted in Fig. 16 and in Fig. B10 and listed in Table B1 (Appendix). The size of the symbols is correlated with the standard deviation of the relations, while the error bars display the uncertainties on the slopes. The slope, as expected, steadily increases when moving from optical to NIR bands. The increase is of the order of 20% in the transition from optical to NIR, and it becomes negligible in the longer wavelength regime. Therefore the intrinsic accuracy of K-band PL relation improves because the slope is steeper,

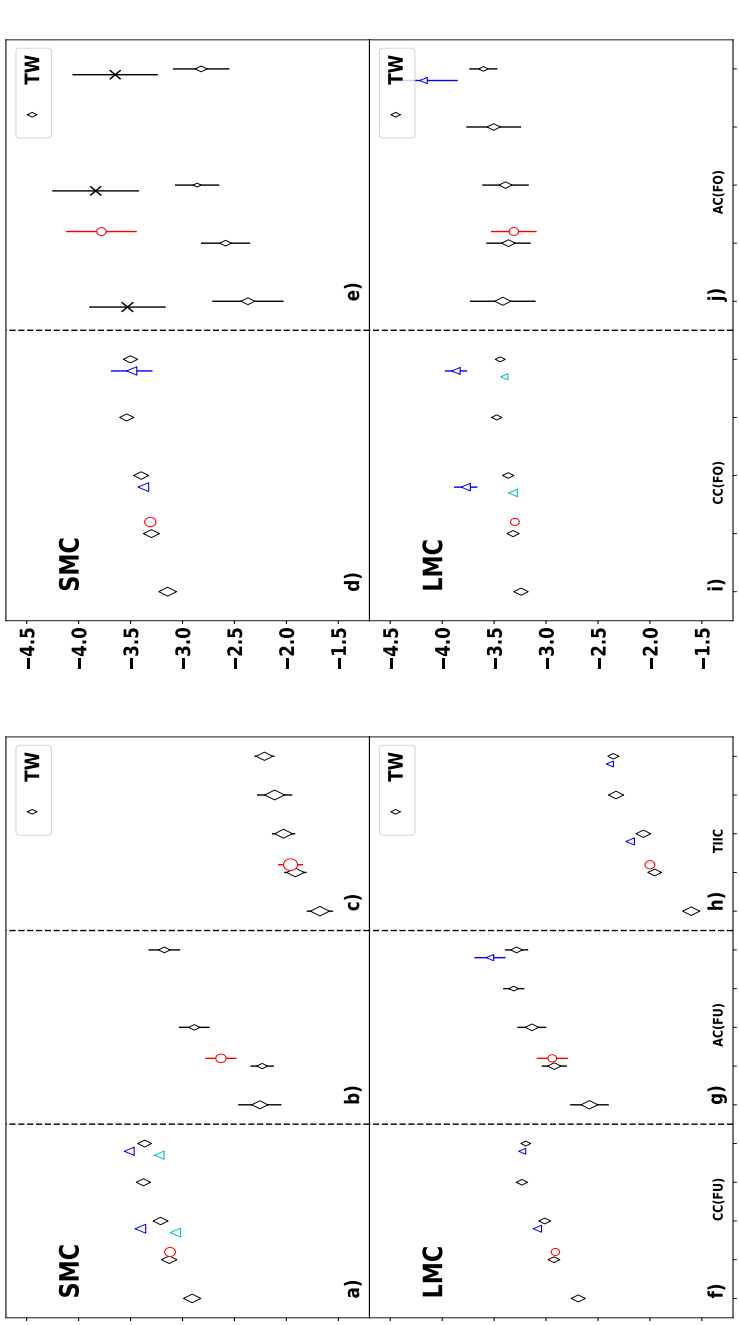

Fig. 20 Top-left: from left to right the slope of the PL relations for SMC fundamental Cepheids: CCs (panel a), ACs (panel b), TIICs (panel c). The size of the symbol is proportional to the error on the slope. The error bar shows the standard deviation of the individual PL relation (see also Table B1 (Appendix)). Black diamonds display our own estimates of the PLs, while red circles show the estimates by Soszyński et al (2015a), triangles (both blue and cyan) the estimates by Ripepi et al (2014, 2015, 2017, 2022b). The blue triangles display the slope of the PL relation for CC(FU) with logP<0.47; the cyan triangles display the slope of the PL relation for CC(FU) with logP>0.47. Top-right same as the top-left, but for SMC first-overtone CCs (panel d) and ACs (panel e). Bottom-left: same as the top-left, but for the LMC fundamental CCs (CCs, panel f; ACs, panel g; TIICs, panel h). Bottom-right: same as the top-right, but for LMC first overtone CCs ((panel i) and ACs (panel j). According to Ripepi et al (2022b) the blue triangles display the slope of the PL relation for FO CCs with P<0.58 days while the cyan triangles display slope of the PL relations for FO CCs with P>0.58 days.

and because they are minimally affected by uncertainties on reddening (Bono et al, 2008).

The agreement with the slopes estimated by (Soszyński et al, 2015a, red circles) is quite good, since it is based on the same data, but using different selection criteria. The same outcome applies to the slopes (blue triangles) of the NIR CC PL relations provided by Ripepi et al (2017, 2022b). In this case we used the NIR mean magnitudes, based on the fit of the light curves provided by Ripepi et al (2017, 2022b), together with the mean of the NIR measurements provided by IRSF (Ita et al, 2004, 2018). The red circles and the blue triangles have been slightly shifted along the X-axis to avoid the overlap with symbols used for the current estimates (diamonds).

Panel b) of Fig. 20 shows the optical NIR slopes for SMC FU ACs. The symbols are the same as in the left panel. The trend when moving from the optical to the NIR bands is similar to the CCs and the slopes also attain similar values, whereas the uncertainty on the slope and the standard deviations are systematically larger (see Table A1 (Appendix)). The uncertainty in the H-band is higher, because in this band fewer measurements have been collected compared with the J and the K-band.

Panel c) of Fig. 20 show the slopes for fundamental SMC TIICs. The trend is, as expected, similar when moving from the optical to the NIR bands. However, the slope of the PL relations are, on average, 30–40% shallower than the slopes of ACs and CCs, while the standard deviations are 1.5–2 times larger. The reasons for the difference have already been discussed in section 5.2.

Bottom left panels of Fig. 20 display the same slopes of the top panels, but for LMC Cepheids. The trend is similar when moving from the optical to the NIR bands as originally suggested by Matsunaga et al (2006, 2009). The blue and the cyan triangles for CCs (panel f) display the comparison with Ripepi et al (2017). The two estimates refer to the PL relations they derived for variables with periods longer/shorter than 4.7 days and they agree, within the errors, quite well. The agreement with similar estimates in the literature is, once again, quite good. The similarity in the slope for LMC and SMC FU TIICs was also suggested by Matsunaga et al (2011). The slopes for both ACs (panel g) and TIICs (panel h) have larger errors due either to small statistics (ACs), or to a large dispersion at a fixed pulsation period (TIICs). Moreover, the slopes of both ACs and TIICs in the NIR bands appear to be either constant, or display a mild decrease. They need to be cautiously treated, since this is probably an observational bias caused by the limited accuracy of NIR mean magnitudes in the short period range (fainter limit) of ACs.

The right panels of Fig. 20 display the same optical, NIR PL relations of the left panels, but for first overtone CCs and ACs. The trends are similar, but there are three distinctive features worth being discussed.

a)– The slopes are on average larger, when compared with fundamental variables (panels d, i), since they range from ∼3 to ∼3.5. Moreover, the current estimates are in remarkable agreement with literature estimates.

b)– The standard deviations of both optical and NIR PL relations are, on average smaller, when compared with the FU CCs. This means that at a fixed chemical composition and photometric band, the width in temperature of the instability strip in which FOs are pulsationally stable is systematically narrower than for FU CCs.

These findings indicate that individual distances based on PL relations for FO CCs are, at fixed chemical composition, intrinsically more accurate (optical), or with an accuracy similar (NIR) to individual distances for FU CCs. This evidence further supports predictions provided by Bono et al (2001) by using pulsation models.

c)–Panel e) of Fig. 20 displays the slopes for SMC FO ACs. The empirical scenario concerning the slopes of SMC FO ACs is more complex. Indeed, the slopes based on the entire sample (crosses) display values similar to the slopes of FO CCs. However, optical and NIR slopes become systematically shallower once the short period tails are neglected (diamonds). The former values agree, as expected, quite well with the estimates provided by Soszyński et al (2015a, red circles). The slope of the H-band was not included, because the number of measurements in this band is either missing (VVV) or limited (IRSF).

Figure 21 shows the coefficients of the logarithmic period in both optical, optical-NIR and NIR PW relations. The key feature of the data plotted in this figure for both FU and FO Cepheids is that the slope is almost constant even if the coefficient of the color term decreases by one order of magnitude when moving from $I,V-I$ to $K,V-K$ (1.38 versus 0.13). Note once again that the PW relations are pseudo PLC relations, in which the coefficient of the color term is only fixed by the reddening law.

The comparison with similar estimates available in the literature is, within the errors, quite good for the different variable groups and distance diagnostics. The only difference is with slopes for FO CCs provided by Ripepi et al (2017), but it is due to the split of the sample in short and long period sub-sample. Indeed, the slopes they found using the entire sample (green triangles) agree quite well.

The similarity between the slopes of the PW relations for FU and FO MC CCs is quite remarkable and applies to optical, optical-NIR and NIR PW relations. This similarity fully supports the simultaneous use of both FU and FO CCs (fundamentalization of the periods) to estimate distances.

Finally, the PW relations for ACs including NIR bands need to be cautiously treated for the same reasons we already mentioned for the NIR PL relations.

5.4 PL versus PLC relations

The pulsation relation dictates that the period of a variable depends on the stellar mass, luminosity and effective temperature. Stellar mass and luminosity are tightly correlated and provided by evolutionary predictions through the so-called mass–luminosity relation. This means that pulsation periods, if we neglect the dependence on the chemical composition, mainly depend on luminosity and effective temperature. Therefore, an individual correlation among the physical parameters governing the pulsation properties of a radial variable requires the knowledge, together with the pulsation period and the pulsation mode of both mean magnitude and color.

Intermediate-mass stars during core helium burning phases cross from one to three times the instability strip. In multiple crossings CCs can have the same effective temperature, and the same radius, and therefore the same luminosity, but different masses. The consequence is a difference in the mean density, and in turn in the pulsation period. In order to address this issue on a more quantitative basis, we investigated

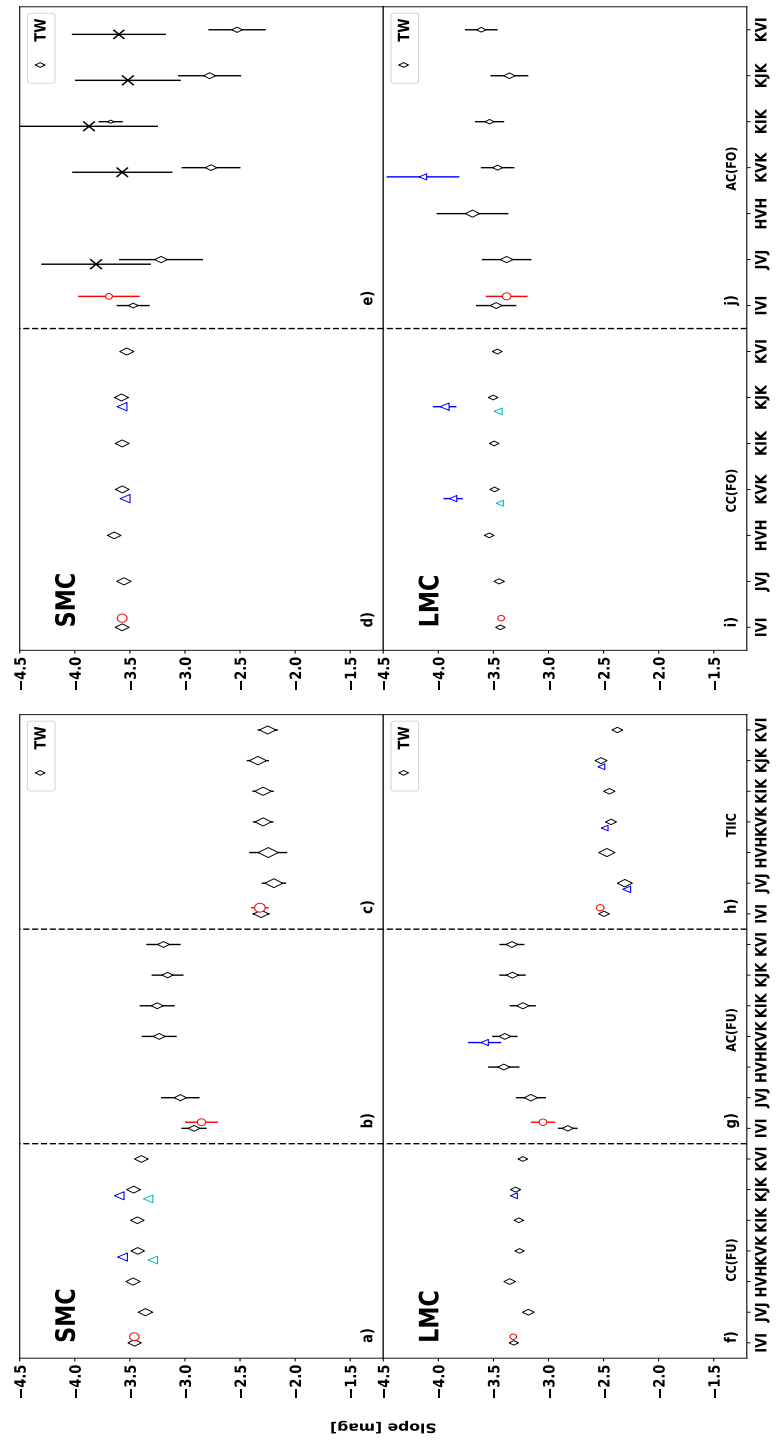

Fig. 21 Top-left: from left to right the slope of optical, NIR and optical-NIR PWrelations for SMC fundamental Cepheids: CCs (panel a), ACs (panel b), TIICs (panel c). The symbols are the same as in Fig. 20. Top-right same as the top-left, but for SMC first-overtone CCs (panel d) and ACs (panel e). Bottom-left: same as the top-left, but for the LMC fundamental CCs (CCs, panel f; ACs, panel g; TIICs, panel h). Bottom-right: same as the top-right, but for LMC first overtone CCs ((panel i) and ACs (panel j).

the difference in luminosity among different crossings for chemical compositions representative of MC and MW CCs (see Fig. 22). Predictions plotted in this figure and listed in Table C3 (Appendix) are based on evolutionary models taking into account mild convective core overshooting during central hydrogen burning phases and at the bottom of the convective envelope along the red giant phases, show that the difference in the mean luminosity across the instability strip between 2nd and 3rd crossing are at most of the order of a few hundredths of a dex. The difference between 1st and 2nd/3rd is larger and of the order of 0.25–0.30 dex, slightly increasing from low to high metallicities. However, the 1st crossing plays a marginal role, since the evolutionary time spent along this crossing is one/two order of magnitude shorter than 2nd+3rd crossing. According to the mass–luminosity relation provided by Bono et al (2000a) the quoted difference ($\Delta \log(L/L_{\odot}) \leq 0.05$) implies a difference in stellar mass of 0.08 $M_{\odot}$ for $M = 5\,M_{\odot}$. The pulsation relation for fundamental CCs correlating stellar mass, luminosity and effective temperature, the so-called van Albada & Baker relation (van Albada and Baker, 1971), provided by Bono et al (2000b, see their Table 6) gives, at fixed effective temperature, a difference in logarithmic period of 0.06 dex. The current analysis is suggesting that the spread either in mass or in luminosity introduced by 2nd and 3rd crossing is negligible.

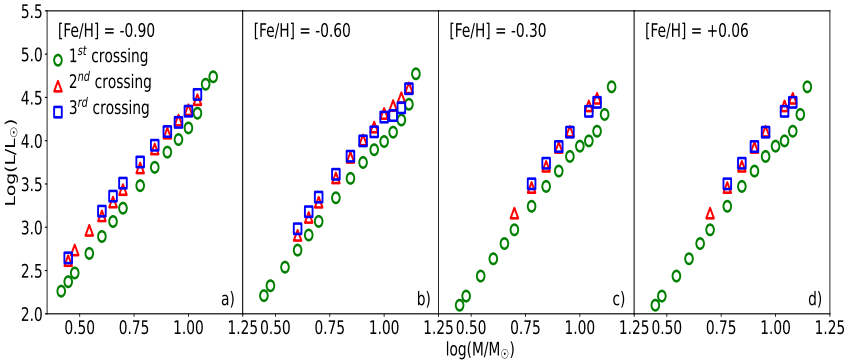

Fig. 22 Panel a) – Logarithmic stellar mass versus logarithmic luminosity for the different crossings of the instability strip. Predictions plotted in this panel have been computed for a scaled solar mixture and at fixed chemical composition ([Fe/H]=-0.90) representative of CCs in metal–poor disk galaxies. The three different crossings are plotted with different colors and symbols. In the less massive regime only the 1st crossing is present, because in these stellar structures the blue loop does not cross the instability strip. In the more massive regime, only the 1st crossing is present because these stellar structures already ignited core helium burning and they cross once the instability strip. Panel b) – Same as Panel a), but for a chemical composition representative of LMC CCs. Panel c) – Same as Panel a), but for a chemical composition representative of SMC CCs. Panel d) – Same as Panel a), but for a chemical composition representative of MW CCs.

The difficulties in using mean colors have already been discussed in section 2.1. Note that random-phase measurements in different bands introduce systematic offsets in the mean color. Moreover, PLC relations are more affected by reddening uncertainties, because they require dereddened magnitudes and colors. These are the main

reasons why individual Cepheid distances are estimated by using either PL or PW relations.

In passing, it is worth mentioning that, on some occasions, the coefficient of the color term in optical (I, V-I) and in optical-NIR (K,$V-K$; Ripepi et al, 2017) PLC relations are, within the errors, quite similar to the ratio between selective absorption coefficient and color excess. It is still not clear whether this similarity is fortuitous, but the quoted PLC relations are also minimally affected by uncertainties in reddening uncertainties.

5.5 Metallicity dependence

We have already discussed in section 2.1 that the pulsation properties of Cepheids depend on the metal content. As a consequence, pulsation diagnostics (PL/PW/PLC relation) adopted to estimate individual Cepheid distances are not Universal. This working hypothesis implies that not only the slope but also the zero-point of the adopted relations depend on the metallicity and they must be properly calibrated.

There are two different paths that we can take in order to analyze the dependence of Cepheid pulsation properties on the metallicity.

The first path relies on circumstantial empirical evidence. We can use either Galactic or Magellanic Cepheids to investigate the impact that metallicity has on individual distance determinations. This approach is still affected by systematics, because quantitative constraints on the metallicity dependence require accurate and homogeneous iron abundances and distances. Accurate iron abundances based on high-resolution spectra are available for a significant fraction of Galactic Cepheids. However, the current estimates are far from being homogeneous. Different investigations rely on different line lists and physical assumptions to estimate physical parameters (effective temperature, surface gravity, micro-turbulent velocity) and elemental abundances (da Silva et al, 2022). However, the strong limitation in the estimate of the metallicity dependence for Galactic Cepheids is the need for accurate (1–2% level) individual geometrical distances.

Accurate trigonometric parallaxes for a dozen Galactic CCs were originally provided by HST, and more recently Gaia is significantly increasing the accuracy and the sample size (Breuval et al, 2021). However, the role that the current sample of Galactic Cepheids can play to assess the metallicity dependence is still lively debated. In a recent investigation, Owens et al (2022) derived new PL relations by using optical (B,V,I), NIR (J,H,K,) and MIR ([3.6], [4.5]) photometric bands for three dozen Galactic CCs with periods ranging from 4 to 60 days and Gaia trigonometric parallaxes. The distances they obtain by applying the new PL relations to the MCs are discrepant when compared with geometrical distances based on detached eclipsing binaries. Their main conclusion is that the coupling between systematics affecting Gaia DR3 trigonometric parallaxes and uncertainties on the metallicity dependence causes the error budget to be at the level of 3%. The current findings indicate that there are still some limitations in using bright Galactic CCs close to the saturation limit, but these thorny problems will be solved in a few years.

In this context, MC Cepheids play a crucial role, because they are located, in first approximation, at the same distance. This means that they are a perfect laboratory to

study the metallicity dependence. However, the number of Cepheids for which accurate iron abundances are available, based on high-resolution spectra, is only limited to less than one hundred LMC Cepheids (Romaniello et al, 2022). The current estimates indicate a modest spread in iron abundance. This finding is also supported by a large sample of metallicity estimates based on the shape of both V- and I-band light curves (Fourier parameters) provided by Hocdé et al (2022). However, the metallicity distribution of B-type stars (progenitors of Cepheids) indicate a spread in N abundance of the order of one dex (Trundle et al, 2007; Hunter et al, 2008, 2009)

Accurate spectroscopic abundances for SMC Cepheids are only available for a few tens Cepheids and they suggest a modest chemical enrichment (Lemasle et al, 2017). The same outcome applies to metallicity estimates of SMC CCs based on photometric indices (Hocdé et al, 2022) and to the metallicity distribution based on spectroscopy of A- and B-type stars (Venn and Przybilla, 2003; Trundle and Lennon, 2005; Hunter et al, 2009)

The second path relies on theoretical predictions. This approach is based on nonlinear, time-dependent convective models of CCs. The current hydro-dynamical codes allow us to construct several series of pulsation models covering a broad range in stellar masses, stellar luminosities and effective temperatures typical of CCs. Moreover, the same calculations can be performed for chemical compositions typical of both Galactic and Magellanic CCs pulsating both in the fundamental and in the first overtone. The key advantage of this approach concerning the metallicity dependence is that pulsation predictions are used to estimate the difference in metallicity and not their own metallicities.

The current predictions indicate that the visual magnitude of CCs, at fixed pulsation period, becomes systematically fainter when moving from metal-poor to more metal-rich stellar structures.

Empirical evidence based on individual heavy element abundances and on both Galactic and Magellanic Cepheids covering a broad range in pulsation periods also indicate that metal-rich CCs are, at a fixed pulsation period, fainter than metal-poor ones. However, no general consensus has been reached on this effect. This applies not only to the derivative, the so-called gamma coefficient, but also to the sign of the coefficient (Storm et al, 2011; Groenewegen, 2018; Ripepi et al, 2021; Breuval et al, 2022; Trentin et al, 2023). This is the typical long-standing open problem which requires a significant improvement in the accuracy and in the sample size of the spectroscopic measurements before we can reach a firm conclusion.

6 Cepheids as stellar tracers

6.1 High-resolution spectroscopy

Cepheids are typically bright stars, therefore we are dealing with very high S/N, broad-wavelength range spectra[9]. The precision of the atmospheric parameters and of the chemical abundances, however, depend not only on the quality of the spectra,

[9] In a short communication to the National Academy of Sciences P.W. Merrill wrote: *... Spectrograms ... show several lines of neutral technetium in the spectra of S-type stars especially of long-period variables. ... It is surprising to find an unstable element in the stars. ... S-type stars somehow produce technetium as they go along ... (Merrill, 1952b, see also Merrill (1952a)).* These are probably the most dry sentences in the history of Astronomy. The content of these sentences

but also on the quality of the adopted line list. With this in mind, a large portion of the investigation by da Silva et al (2022) was dedicated to finding the best atomic transitions for iron and α–elements that can be detected in Cepheids. This means i) collecting the most precise transition parameters, ii) removing absorption lines which are blended with other lines, and iii) eliminating lines that for any reason deviate significantly from the average value for their chemical species, or that display a dependence on effective temperature, surface gravity and micro-turbulent velocity across the pulsation cycle.

The first point is typically addressed by using a list of hundreds of atomic transitions for iron and α–elements commonly employed in the literature. Their transition parameters were updated, whenever possible, with laboratory measurements from Ruffoni et al (2014), Den Hartog et al (2014) and Belmonte et al (2017) for Fe I, (Den Hartog et al, 2019) for Fe II, (Lawler et al, 2013) for Ti I, and for Ti II (Wood et al, 2013). The astrophysical, but homogeneous and precise compilation of Meléndez and Barbuy (2009) for Fe II lines was also adopted. For the remaining lines, the transition parameters collected and updated by the National Institute of Standards and Technology (NIST) Atomic Spectra Database (Kramida et al, 2020) were used. If a line is not available in any of these sources, it is eliminated from the preliminary list and not used for the computation of atmospheric parameters, nor chemical abundances.

The second point was addressed by removing blended lines, using as a reference the Solar spectrum table by Moore et al (1966) and synthetic spectra. Then, da Silva et al (2022) measured their equivalent width (EW) using the Automatic Routine for line Equivalent widths in stellar Spectra (ARES, Sousa et al, 2007, 2015).

Finally, the third point was taken into account by removing deviant lines. At first, the initial values were estimated for the atmospheric parameters and the chemical abundances. Lines are considered deviant if their abundances differ by at least 3σ from the mean for a given element, or if their behavior across the pulsation cycle is irregular. This latter situation is investigated by plotting all line-by-line measurements for each chemical species and individual exposure of the calibrating stars versus phase, effective temperature, and equivalent width, and removing lines that show strong trends in any of those planes. The calibrating stars mostly used are those with the largest number of individual spectra covering the whole pulsation cycle, such as β Dor, ζ Gem, and FF Aql.

The reader interested in the final clean lists adopted for the estimate of the atmospheric parameters and the chemical abundances (quality flag 1) and for comparison purposes (quality flag 0) is referred to Tables 2 and 3, and to Appendix A by da Silva et al (2022).

not only explained the observations of Tc in AGB stars, but also paved the way to modern nuclear Astrophysics, to stellar nucleo–synthesis and to the Astrophysical origin of the Periodic Table.

6.2 Atmospheric parameters

6.2.1 Effective temperature, surface gravity and micro-turbulent velocity

The approach typically adopted to estimate the atmospheric parameters (i.e., the effective temperature, the surface gravity, and the micro-turbulent velocity, [ξ]) was already discussed in detail by Proxauf et al (2018). Here we only recap the key points. The $T_{\rm eff}$ along the pulsation cycle was estimated by using the LDR method, which relies on the correlation between the line-depth ratios of pairs of absorption lines in the spectra of different stars and the effective temperature of the same stars. The surface gravity was derived through the ionization equilibrium of Fe I and Fe II lines, and the micro-turbulent velocity was obtained by minimizing the dependence of the abundances provided by single Fe I lines on their EWs. During this procedure, the effective temperature was kept fixed, whereas $\log g$ and ξ were iteratively changed until convergence. The metallicity used as input by our algorithm is updated at each step, and the adopted value is [Fe I/H], which is the mean iron abundances provided by individual Fe I lines. The uncertainties on $T_{\rm eff}$ are the standard deviations calculated using the LDR method, they are typically of the order of 150 K while the uncertainties on the individual estimates of $\log g$ and ξ are assumed to be ~0.3 dex and 0.5 km s^{-1} (see Genovali et al (2014) for a detailed discussion).

Thanks to these improvements, the errors on the derived amplitudes for the effective temperature curves are a factor of two smaller than our previous estimates, whereas for the surface gravity the differences are even more significant, with typical errors almost three times smaller. Concerning the micro-turbulent velocity variation, the errors on the current amplitude estimates are, on average, more than twice smaller (Proxauf et al, 2018).

The improvement in the estimate of $\log g$ and ξ is mainly due to the improvement in the line list, which reduced the number of spurious abundance values provided by unreliable iron lines. Together with the removal of blended lines, and of lines that display a well-defined trend with effective temperature or with equivalent width. The estimate of $T_{\rm eff}$ is based on the same line list that we previously used, therefore the improvement is mainly due to the larger number of spectra analyzed by da Silva et al (2022). The reader interested in a more detailed discussion concerning the estimate of the intrinsic parameters of classical Cepheids is referred to Vasilyev et al (2018).

In this context, it is worth mentioning that the improvement in the accuracy and in the sampling of the pulsation cycle improved the empirical framework concerning the variation of atmospheric parameters along the pulsation cycle. Indeed, the minimum in the effective temperature is often approached across the same phases in which the minimum in surface gravity is also approached. Moreover and even more importantly, these phases across the minimum anticipate the increase in micro-turbulent velocity. This parameter, as expected, attains its maximum just before the maximum in effective temperature (see Figs. B.2 and B.4 in da Silva et al 2022).

A new and innovative approach to constrain the temperature scale of classical Cepheids was recently suggested by Lemasle et al (2020). The new approach relies on a data-driven machine-learning technique applied to observed spectra, in which

the flux ratios were tied to temperatures derived using the infrared surface-brightness method.

6.2.2 Effective temperature curve templates

By taking advantage of the substantial phase coverage of the sample of calibrating Cepheids, the effective temperature measurements based on LDRs were also adopted to compute new templates for different bins of pulsation periods (da Silva et al, 2022). However, instead of using the $T_{\rm eff}$ curves directly, they preferred to provide templates for the θ parameter – defined as $\theta = 5040/T_{\rm eff}$ – given its linear dependence on the Johnson–Cousins $R - I$ color index (Taylor, 1994).

The approach is similar to the NIR light-curve templates provided by Inno et al (2015): first, periods and reference epochs are adopted to fold the θ curves (θCs). Subsequently, the folded θCs were normalized by subtracting their average and dividing by their amplitudes. The θCs curves are well sampled, meaning that the phase points are large enough to separate the Cepheids into different period bins and to provide analytical relations for the θ curve templates in each bin. We adopted the same period thresholds introduced by Inno et al (2015). Therefore, based on their Table 1, da Silva et al (2022) generated four cumulative and normalized theta curves for the bins 2 (3–5 days, three Cepheids), 3 (5–7 days, three Cepheids), 4 (7–9.5 days, two Cepheids), and 5 (9.5–10.5 days, two Cepheids). By adopting the same period bins, they were able to provide θC templates homogeneous with those adopted for the NIR light curve templates. The reader interested in a more detailed and quantitative discussion about the use of both cumulative and normalized curves to derive the analytical fits, together with the adopted thresholds for the different period bins, is referred to Inno et al (2015).

The normalized θ curves for the four period bins are plotted in Fig. 23 together with the analytical fits (black lines), based on Fourier series, to the data (see Fig. 7 in da Silva et al, 2022). The separation of the Cepheids into different period bins is a mandatory step, because not only the amplitude of the θ curves, but also their shape changes with period. Note that spectroscopic data for Cepheids with periods outside the selected period bins are available, but they are either not as well-sampled as the data for the other Cepheids, or the θ curves do not overlap very well because of the limited number of measurements. More accurate and homogeneous data for FU and FO CCs are required in order to overcome this limitation.

The use of the effective temperature curve templates to derive the mean effective temperature requires the ephemerides, the luminosity amplitude (ΔV), and a single spectroscopic measurement of the $T_{\rm eff}$ together with a linear relation between ΔV and $\Delta\theta$: $\Delta\theta = (0.184 \pm 0.014)\Delta V + (0.000 \pm 0.011)$; ($\sigma = 0.013$).

The estimate of the $\Delta\,\theta$ amplitude must be applied to the normalized template as a multiplier factor. Only after this re-scaling operation can the template be anchored to the empirical data and used to derive the mean $T_{\rm eff}$.

However, the effective temperature curve templates are far from being an academic issue, since once a period–mean temperature relation is known, they can also provide the estimate of the effective temperature along the pulsation cycle. This

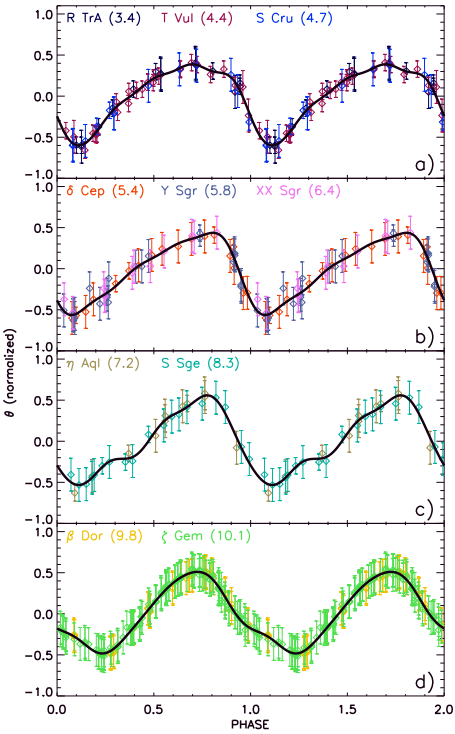

Fig. 23 From top to bottom: Normalized $\theta = 5040/T_{\rm eff}$ curves of CCs in different period bins (3–5 days, panel a; 5–7 days, panel b; 7–9 days, panel d; 9–11 days, panel e). Different colors are associated to different CCs. The names of the CCs are labelled and the numbers in parentheses show the pulsation period in days. The black line is the analytical fit to the θ-curve template. Adapted from da Silva et al (2022, Fig. 5). Image credit: R. da Silva.

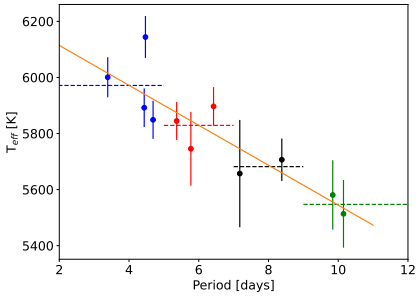

Fig. 24 Effective temperature versus period for CCs with full coverage of the pulsation cycle. The different colors indicate the different period bins of the temperature curve templates. The dashed lines indicate the average temperature for each bin in period. The orange line shows the linear fit to the data.

is a far-reaching opportunity, since effective temperature estimates based on color-temperature relations are hampered by uncertainties affecting reddening estimates.

This is a trivial effort in the optical regime with high-resolution and high signal-to-noise spectra, but it becomes more difficult either in the NIR, or at low spectral resolution, or in the very metal-poor regime due to the paucity of lines. Therefore, we performed a linear fit between pulsation period and mean effective temperature (see Fig. 24) and we found:

$$T_{\rm eff}[K] = 6256.73(\pm 89.45) - 71.23(\pm 13.29) \times P \quad (1)$$

with a standard deviation of 286 K. Once the mean $T_{\rm eff}$ is available, one can anchor the temperature template to the phase of the spectroscopic measurement and provide an estimate of the $T_{\rm eff}$ at any phase.

Optical and NIR light curves of the calibrating Cepheids, together with effective temperature and radial velocity curves, can be adopted to perform a detailed comparison with nonlinear, convective hydrodynamical models of classical Cepheids. Dating back to Natale et al (2008), it has been found that the simultaneous fit of both luminosity and radial-velocity variations provides solid constraints on the physical assumptions adopted to build pulsation models (Marconi et al, 2013). Moreover, the use of the effective temperature curves (shapes and amplitudes), covering a broad range of pulsation periods, brings forward the opportunity to constrain, on a quantitative basis, the efficiency of the convective transport over the entire pulsation cycle.

6.3 Metallicity distribution in the Galactic thin disk

In discussing the metallicity distribution of Cepheids, we are following a series of papers (Romaniello et al, 2008; Pedicelli et al, 2010; Lemasle et al, 2013, 2017; Inno et al, 2019; Genovali et al, 2013, 2014; da Silva et al, 2016; Proxauf et al, 2018; da Silva et al, 2022) focused on the metallicity distribution of CCs. We are following these papers because they rely on the same strategy for the estimate of the atmospheric parameters and of the abundances.

Spectroscopic abundances discussed in the following rely on 1D LTE analysis. These investigations are based on different sets of 1D LTE atmosphere model provided by Castelli and Kurucz (2004), and by Gustafsson et al (2008). Theory and observations suggest that this approach is prone to systematics when compared with 1D and/or 3D NLTE analysis. This effect becomes larger when moving from dwarfs to giants and from metal-rich to more metal-poor stellar populations (Thévenin and Idiart, 1999; Idiart and Thévenin, 2000; Bergemann et al, 2012; Hansen et al, 2013; Fabrizio et al, 2021). Different lines of the same element have different NLTE corrections (Collet et al, 2005; Merle et al, 2011) and neutral lines are more affected than ionized lines. Theory and observations indicate that Fe II lines are minimally affected by NLTE effects (Lind et al, 2012; Hansen et al, 2013). Moreover, the forbidden [O I] line at 6300.3 Å is not subject to any NLTE effect in cool stars (Kiselman, 2001; Tautvaišienė et al, 2015) and the same outcome applies to the S I triplet at 6757 Å as thoroughly discussed by Duffau et al (2017). Fortunately, CCs are GK-type giants and they display in high resolution and high signal-to-noise ratio spectra from several to a few dozen of FeII lines. Moreover, the S I triplet is unblended and relatively

strong and the quoted forbidden line can be measured over a significant fraction of Galactic CCs (da Silva et al, 2023). The Galactic metallicity gradients based on other elements should be cautiously treated until the 1D and the 3D NLTE analysis will be performed.

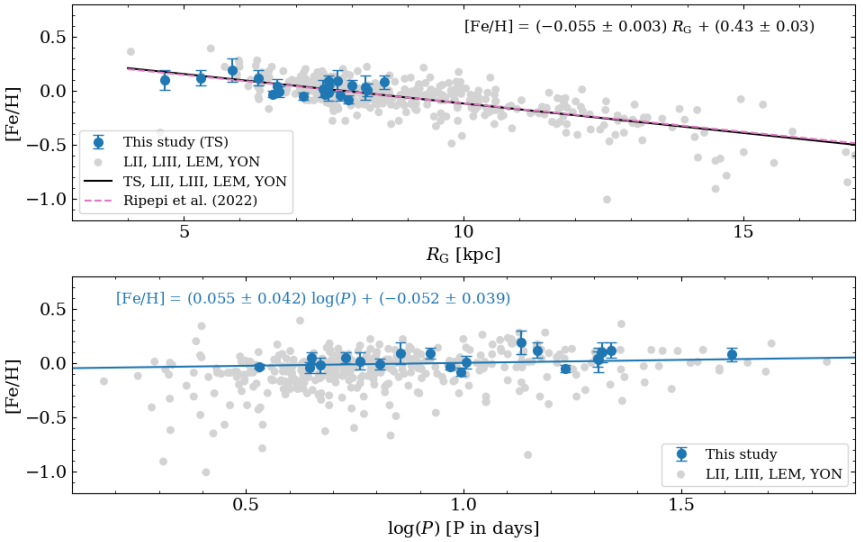

Fig. 25 Top: Iron abundances as a function of the Galactocentric distance for a sample of 20 calibrating Cepheids (blue circles) compared with results from the literature (gray circles): Luck et al (2011, LII); Luck and Lambert (2011, LIII); Lemasle et al (2013, LEM); Yong et al (2006, YON). A linear regression (solid black line plus equation) fitted to the entire sample is compared with the radial gradient provided by Ripepi et al (2022a) (dashed magenta line). The latter was artificially shifted in order to coincide with the current radial gradient at R_G = 10 kpc. The R_G values are from Genovali et al (2014). Bottom: same as the top, but as a function of the logarithmic pulsation period. The solid blue line plus the equation show the linear regression fitted to the current sample. Image reproduced with permission from da Silva et al (2022, Fig. 10), copyright by ESO.

6.4 The iron distribution

During the last few years, several investigations have addressed the open problem concerning the space and age dependence of the metallicity gradient in the Galactic thin disk. This issue has been studied not only from the empirical (see, e.g., Maciel et al, 2003; Nordström et al, 2004; Henry et al, 2010; Yong et al, 2012) but also from the theoretical point of view. In particular, the role that different stellar tracers can play in constraining the chemical tagging in spatial distribution and in age distribution (Freeman and Bland-Hawthorn, 2002).

In order to investigate the iron distribution of the calibrating Cepheids (blue circles) provided by da Silva et al (2022), the top panel of Fig. 25 shows the individual iron abundances as a function of Galactocentric distance R_G. Note that da Silva et al (2022) defined calibrating CCs only variables whose entire pulsation cycle is covered by high-resolution spectra. The gray circles display similar Cepheid abundances, but

only for CCs available in the literature. A linear fit over the entire sample gives the following relation:

$$[\mathrm{Fe/H}] = (-0.055 \pm 0.003)\, R_G + (0.43 \pm 0.03) \quad (2)$$

The current slope agrees quite well with similar estimates available in the literature and, in particular, with the recent estimate of the iron radial gradient (dashed line) provided by Ripepi et al (2022a). To overcome variations in the zero-point, mainly introduced by the sampling of innermost and outermost Cepheids, the gradient from Ripepi et al (2022a) was artificially shifted, so as to coincide with the current radial gradient at $R_G = 10$ kpc.

The bottom panel of Fig. 25 shows the iron abundance as a function of the logarithmic pulsation period. Data plotted in this panel agree quite well with similar estimates available in the literature. Moreover, they do not show any significant variation in iron abundance when moving from young (long-period) to less young (short-period) classical Cepheids.

6.5 Light metals and α-element distribution

This section deals with light metals and α-element gradients traced by CCs across the Galactic thin disk. Fig. 26 shows the abundances of Na, Al and of three α-elements (Mg, Si, Ca) as a function of the Galactocentric distance. The five investigated elements display well-defined radial gradients. The difference in standard deviations is mainly correlated with the number of lines adopted to estimate the abundances. The dispersion of the Mg gradient is almost a factor of two larger than the Si gradient, because the former is based on a single line, while the latter on more than a dozen. The radial gradients of the five investigated elements attain, within the errors, quite similar slopes as originally found by Lemasle et al (2007, 2013) and by LII+LIII. The above result becomes even more compelling if we consider the similarity with the iron radial gradient (-0.060 ± 0.002 dex kpc^{-1}) found by G14 using the same CCs. The current radial gradients seem to show a flattening for distances greater than ~13 kpc. This supports a similar trend, but based on open clusters (Carraro et al, 2007; Yong et al, 2012; Magrini et al, 2023). However, firm conclusions are hampered by the increased spread in abundance and by the scarcity of outer-disk CCs.

One of the most relevant issue in dealing with the chemical enrichment history of the thin disk is the age dependence. Indeed, chemo-dynamical models suggest a significant flattening of the metallicity gradients for ages older than 1-3 Gyr (Minchev et al, 2014; Kubryk et al, 2015). This means a steady decrease in the metallicity with increasing age. The same models also predict a strong dependence on stellar migrations. To constrain the age dependence of the metallicity gradients, Fig. 2 in Genovali et al (2015) shows the same elemental abundances of Fig. 26, but as a function of the logarithmic period. Data plotted in their figure show a well-defined positive gradient for increasing pulsation period. The slopes of the α-elements attain similar values, while for Na and Al they are systematically larger (see labelled values). This evidence further supports the hydrostatic nature (Arnett, 1979; Limongi and Chieffi, 2018) of

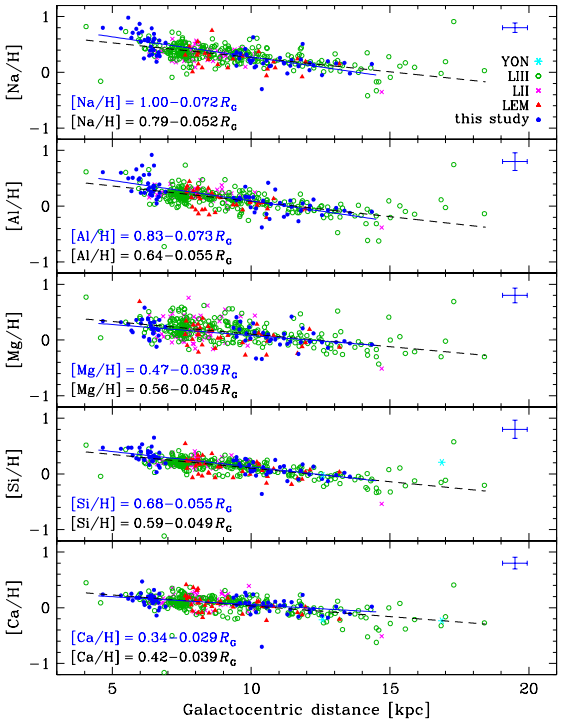

Fig. 26 From top to bottom: Abundances for CCs of Na, Al, and α elements (Mg, Si, Ca) as a function of Galactocentric distance. The abundances by G15 (filled blue circles) are compared with those of Yong et al (2006, YON, cyan asterisks), Luck et al (2011, LII, magenta crosses), Luck and Lambert (2011, LIII, open green circles) and Lemasle et al (2013, LEM, red triangles)). The solid and the dashed lines display the linear regressions to only G15 data and to the entire sample. Image reproduced with permission from Genovali et al (2015, Fig. 2), copyright by ESO.

both Na and Al, owing to their steady increase correlated with the pulsation period (stellar mass).

Data plotted in Fig. 5 of Genovali et al (2015) show that the ratio [element/Fe] is, on average, quite flat across the entire thin disk. They performed a bi-weight linear least squares fit over the entire sample, and they found evidence of a positive slope for Ca. This finding brings forward a few interesting consequences.

i)–Chemical enrichment history– Iron and the other five elements have had quite similar chemical enrichment histories across the Galactic thin disk. Moreover, the quoted ratios have small standard deviations suggesting that it is dominated by measurement errors. The [α/Fe] ratios are typically considered as tracers of the star-formation activity and the lack of a clear negative gradient between the high (inner) and the low (outer) density regions of the thin disk suggests that either the iron and the quoted elements are produced by the same polluters, or the [α/Fe] radial gradients are affected by other parameters, such as radial migration of stars or radial gas flows.

ii)–Radial gradients– The occurrence of a mild positive gradient in [Ca/H] as a function of period, and of a negative gradient of [Ca/H] as a function of Galactocentric distance are not correlated, since CCs located in the outer disk have a canonical period distribution (mostly between 2 and 20 days). The negative trend shown by Ca when moving from older to younger CCs remains unclear.

In order to further investigate the ratio between hydrostatic and explosive elements, the left panel of Fig. 11 in Genovali et al (2015) shows [Mg/Ca] as a function of the iron abundance. The CCs display typical solar abundances for iron abundances that are more metal-poor than the Sun, but the spread increases to 0.5–0.7 dex for iron abundances more metal-rich than the Sun. On the other hand, the abundance ratio of thin- and thick-disk dwarfs (B05, M14) display the typical decrease when moving from metal-poor to more metal-rich objects. The metal-rich regime shows a similar trend, and indeed the metal-rich dwarfs (green diamonds, B05) display a mild increase in the [Mg/Ca] abundance ratio for [Fe/H]≥0.15.

The reasons for the above difference are not clear, therefore G15 searched for a possible radial dependence. Data plotted in the middle panel of their Fig. 11 display that a significant fraction of the spread in [Mg/Ca] abundance (∼0.7 dex) showed by metal-rich CCs is evident among objects placed either across or inside the solar circle (∼8 kpc). However, the abundance ratio is quite constant across the disk regions covered by CCs and dwarfs. This trend is slightly counter intuitive, since the increase in iron, typical of the innermost disk regions, should also be followed by a steady increase in Ca, since they are explosive elements. Namely, there is a steady decrease in the [Mg/Ca] abundance ratio when approaching the innermost disk regions.

The right panel of their Fig. 11 shows the [Mg/Ca] abundance ratio of CCs as a function of the logarithmic period. Data plotted in this figure show no clear trend. The spread in the [Mg/Ca] abundance ratio is almost constant over the entire period range, thus suggesting that there is no solid evidence of a dependence on stellar mass.

The scientific impact of the α-element abundances on the chemical enrichment of the Galactic thin disk, and the difference between explosive and hydrostatic elements have been recently addressed by Trentin et al (2023).

6.6 Neutron capture distribution

In the following, we discuss the radial gradients of four s-process (Y, La, Ce, Nd) elements and a single r-process element (Eu). The n-capture elements can be split according to solar system abundances in pure s-process, pure r-process, and mixed-percentage isotopes. Among them, Eu is a pure r-process element, since the r-fraction abundance is 97% (Burris et al, 2000; Simmerer et al, 2004), while for the s-process elements the s-fraction ranges from roughly 50% (Nd, 58%, Sneden et al, 2008) to more than 70% (Y, 72%; La, 75%; Ce, 81%). The quoted s- and r-fraction abundances should be treated cautiously since Bisterzo et al (2011), by using a different approach, found similar fractions for Eu (94%), Nd (52%), La (71%), and Ce (81%), but a significantly larger s-fraction for Y (92%).

Figure 27 shows the abundance of the five selected neutron capture elements as a function of the Galactocentric distance. Data plotted in this figure bring out several interesting results.

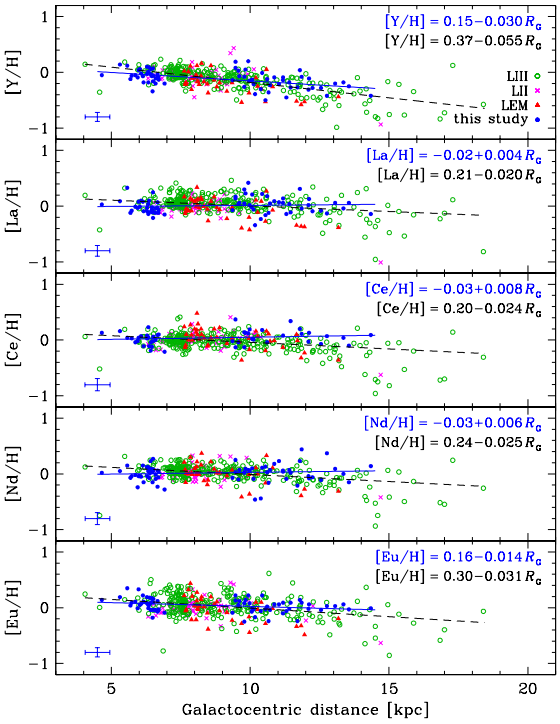

Fig. 27 From top to bottom: Abundances for CCs of neutron capture elements (Y, La, Ce, Nd, Eu) as a function of the Galactocentric distance. Abundances provided by da Silva et al (2016, filled blue circles) are compared with those of LII (magenta crosses, Luck et al, 2011), LIII (open green circles, Luck and Lambert, 2011), and LEM (red triangles, Lemasle et al, 2013). The blue solid line shows the linear regression of our Cepheid sample, while the black dashed line the linear regression of the entire Cepheid sample. The blue error bars display the mean spectroscopic error of the current sample. The abundances available in the literature have similar errors. Adapted from da Silva et al (2016, Fig. 2). Image credit: R. da Silva.

i)–Neutron-capture radial gradients– The five investigated neutron-capture elements display well-defined radial gradients. This evidence, combined with similar results concerning iron peak and α-elements (LII, LIII) further indicates that young stellar tracers show radial gradients across the Galactic thin disk. There is only one exception, Andrievsky et al (2014) and Martin et al (2015) found that Ba does not display a radial gradient. However, Ba abundances in classical Cepheids are affected by severe limits. In particular, Luck (2014) noted that strong BaII lines are affected by line-formation effects, while Andrievsky et al (2013) discussed isotopic shift effects. The reason for the lack of a Ba gradient remains unclear.

ii)–Slopes of the radial gradients– The slopes are quite similar, on average -0.025 ± 0.004 dex kpc^{-1} for La, Ce, Nd, and Eu. The only exception is Y, for which the slope is more than a factor of two steeper (-0.053 ± 0.003 dex kpc^{-1}). The current slopes agree quite well, within the errors, with similar estimates available in the literature.

iii)–Spread of the radial gradients– The spread of the individual abundances attains similar values across the thin disk. The outermost disk regions are an exception, since the spread increases for R_G larger than 13 kpc. The neutron-capture elements display the same trend of iron and α-element abundances. Among the investigated elements, Y once again seems to be an exception, since the spread is homogeneous across the disk regions covered by the current CC sample.

iv)–Theory and observations– Radial gradients for La ($\sim 0.020 \pm 0.003$ dex kpc^{-1}) and for Eu ($\sim 0.030 \pm 0.004$ dex kpc^{-1}) agree quite well with theoretical predictions by Cescutti et al (2007) for Galactocentric distances covering the entire thin disk ($4 \leq R_G \leq 22$ kpc). They found a slope of ~ 0.021 dex kpc^{-1} for La and of ~ 0.030 dex kpc^{-1} for Eu. The predicted slopes become steeper for Galactocentric distances shorter than 14 kpc, and shallower for distances larger than 16 kpc (see their Table 5).

6.7 CNO distribution

CNO abundances are a solid diagnostic to constrain evolutionary predictions, based on different physical assumptions, concerning the size of the helium core and the efficiency of the first dredge-up. The key issue is that evolutionary models accounting for core rotation display an enhancement in N that is significantly larger when compared with models neglecting rotation and only accounting for semi-convection and/or convective core overshooting during central H-burning phases. This means that CNO abundances are a solid observable to constrain the input physics of intermediate-mass models (Anderson et al, 2014). Even though the abundances of these three elements can play a key role to constrain the physics of intermediate-mass stars, we still lack accurate and homogeneous measurements of short and long-period Galactic and Magellanic CCs (Andrievsky et al, 2005; Kovtyukh et al, 2005; Luck and Lambert, 2011; Romaniello et al, 2022; Trentin et al, 2023), to constrain the impact that mixing due to the first dredge-up (see section C.3 in Appendix) have on the surface abundances of CCs.

6.8 A new spin on iron and α-element abundance gradients

In a recent investigation da Silva et al (2023) provided a new homogeneous and accurate investigation of the radial gradients (iron, α-elements [O, S]) across the Galactic thin disk by using CCs. This paper offers several new insights concerning the MW chemical enrichment history. The main novelties when compared with similar investigations in the literature are the following.

i)–Sample selections– High-resolution, high SNR spectra for CCs were secured with four different spectrographs, the sample includes more than 1100 spectra for 356 variables. For 77 CCs accurate abundances are provided for the first time. The heliocentric distances are mainly based on Gaia EDR3 distances (Bailer-Jones et al, 2021) complemented with NIR and MIR diagnostics available in the literature. Their Galactocentric distances range from the inner disk (R_G=5 kpc) to the outskirts of the disk (R_G=30 kpc) with a handful (eight) of Cepheids located at distances larger than 18 kpc. Moreover, they also investigated the orbital properties of their spectroscopic

sample and they found that the bulk of them have orbits typical of thin disk stars. The sample of open clusters is from Randich et al (2022) and includes 62 stellar systems observed by the Gaia-ESO Survey (GES) plus 18 OCs retrieved from the ESO archive (Viscasillas Vázquez et al, 2022). The age of the OCs ranges from a few Myrs to ∼7 Gyr, while their Galactocentric distances range from ∼6 to 21 kpc.

ii)–Homogeneous abundances– Atmospheric parameters and elemental abundances over the entire spectroscopic sample were based on individual spectra. The abundances for each spectrum are the mean value computed from individual lines. The final abundances for variables with multiple spectra are the mean over the individual spectra.

iii)–Spectroscopic diagnostics– The O abundances are based on the forbidden [O I] line at 6300.3 Å, in the LTE approximation, while S abundances are based on the S I triplet at 6757 Å.

The radial gradient for iron, oxygen and sulphur are plotted as a function of the Galactocentric distance in Fig. 28. Simple inspection to the data plotted in this figure disclose several new findings.

i)–Linearity of the radial gradient– The iron radial gradient is linear for Galactocentric distances smaller than ∼12 kpc, but it becomes flatter at larger distances ($R_G \geq$15 kpc). They also found that a logarithmic fit takes into account the linear gradient of the inner disk and for the flattening of the outer disk. Their estimates of both linear and logarithmic fits agrees quite well with similar estimates available in the literature (Carraro et al, 2007; Yong et al, 2012; Donor et al, 2020; Magrini et al, 2023). However, the iron radial gradient provided by da Silva et al (2023) shows a well defined departure from linearity for Galactocentric distances larger than 12–14 kpc. A more quantitative analysis requires a larger sample to assess whether the radial gradient shows either a change in the slope, or a steady variation with distance, as suggested by the logarithmic fit.

ii)–Comparison between CCs and OCs– Data plotted in the top panel of Fig. 28. show that CCs and OCs show similar iron radial gradients. Moreover, the ages of the GES OC sample cover more than one order of magnitude, whereas their radial distributions are similar. However, the flattening of the radial gradient in the outer disk is only partially supported by OCs, since they typically have Galactocentric distance smaller than ∼15 kpc with a single cluster located at ∼20 kpc.

iii)–Oxygen radial gradient– A glance at the oxygen abundances plotted in the middle panel of Fig. 28 shows that the oxygen radial gradient is 25% shallower than the iron gradient. CCs and OCs display very similar radial trends and a vanishing, if any, dependence on the cluster age. To overcome possible systematics, da Silva et al (2023) used the same data provided by Magrini et al (2023) and performed an independent fit following the same approach adopted for CCs. They found that the two gradients, within the errors, agree quite well with each other. The comparison with similar estimates available in the literature based on CCs indicates that the current slope is shallower (Luck and Lambert, 2011; Trentin et al, 2023). However, the comparison should be used carefully, since the difference could be due to the different lines adopted for measuring oxygen abundances, and to the spectroscopic analysis.

iv)–Slope of the sulfur radial gradient– Data plotted in the bottom panel of Fig. 28 show that the linear fit of the sulfur radial gradient is twice steeper than the slope of the iron gradient, while the difference in the logarithmic fit is ≈0.7 dex $(\log \mathrm{kpc})^{-1}$. It is noteworthy that the sulfur radial gradients for both CCs and OCs agree quite well. Indeed, the zero-points and the slopes of the linear fits attain very similar values (see labels). This circumstantial evidence brings forward an α-element with a radial gradient steeper than the iron gradient, and points toward a more significant role played by massive stars in iron and sulfur chemical enrichment.

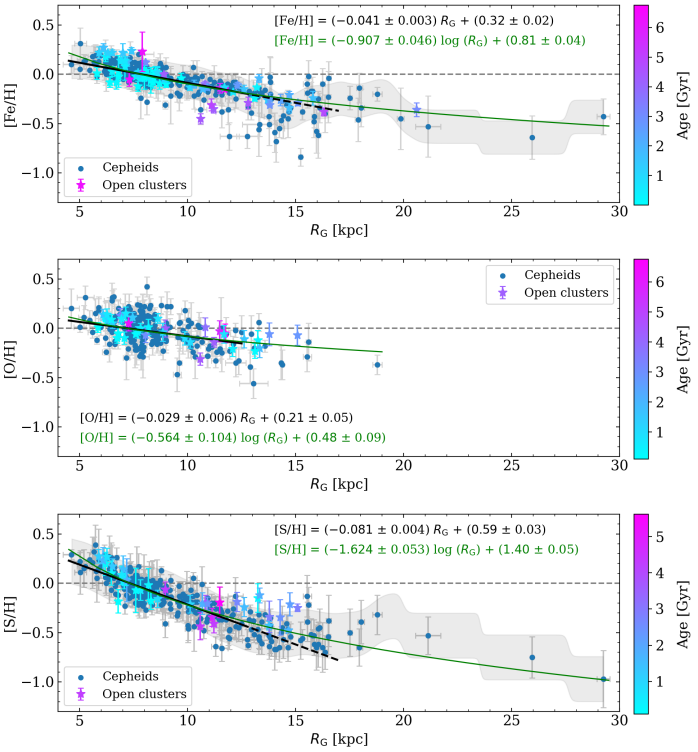

Fig. 28 Top: Iron abundances for CCs as a function of the Galactocentric distance (kpc). CCs are marked with blue circles while OCs with colored symbols. Iron abundances for OCs are from Magrini et al (2023). The solid black line shows the linear regression for CCs with Galactocentric distances ranging from 4 to 12.5 kpc, while the dashed black line is the extrapolation up to 17 kpc. The green line displays the logarithmic fit over the entire sample of CCs. The coefficients of the analytical relations are labelled. The shaded area shows the running average, and its standard deviation, weighted with a Gaussian function taking into account the errors. Middle: same as the top, but for O abundances. Bottom: Same as the top, but for S abundances. Adapted from da Silva et al (2023, Fig. 2). Image credit: R. da Silva.

The same authors also performed a detailed comparison between observations and chemical evolution models of the Galactic thin disk. They adopted the best-fit model recently provided by Palla et al (2020) and they found that the use of a constant star formation efficiency for $R_G \geq 12$ kpc takes into account the flattening observed

in iron and in α-element radial gradients. Moreover, they found that inside the solar circle the current [S/H] and [S/Fe] gradients are well reproduced by canonical yield prescriptions by Kobayashi et al (2006) and by Kobayashi et al (2011). The same comparison indicates that a decrease of a factor of four in the current S predictions is required to explain the flattening in the outermost regions. This means a relevant decrease in the S yields in the more metal-poor regime.

Finally, Matsunaga et al (2023) took advantage of high resolution, near infrared spectra, covering the Y,J-bands, collected with WINERED at the Magellan telescope to investigate the iron abundance of 16 CCs located in the inner disk (R_G=3–5.6 kpc). They found that the iron radial gradient in this region is either shallower or even flat (see their Fig. 2 and also Kovtyukh et al 2022).

7 Omne ignoto pro magnifico

The next two subsections are focussed on open problems concerning Cepheids with possible/challenging near-term solutions.

7.1 Open problems with possible near future solutions

The most interesting open problems at the crossroad between theory and observations appear to be the following.

i)–Nonlinear, convective models for long-period TIIC Cepheids– The current generation of nonlinear, convective hydrodynamical models of variable stars shacked off their speculative nature and are providing solid predictions of the current properties of radial variables. However, we are still missing detailed pulsation predictions concerning long-period W Virginis and RV Tauri.

ii)–Metallicity dependence of both PL, PLC and PW relations– This is a sort of message in the bottle for future spectroscopic surveys. Gaia and long-term ground-based variability surveys (ASAS-SN[10], OGLE-IV[11], ZTF[12], PTF[13], KISOGP (Takase and Miyauchi-Isobe, 1984) will provide solid identification of thousands of Galactic Cepheids. In a few years, Gaia will also provide accurate geometrical distances for a good fraction of them. Moreover, the use of high resolution images collected with NIRCam on board James Webb Space Telescope[14] is providing the unique opportunity to test the crowding affecting extragalactic Cepheids and to validate earlier results based on HST photometry (Riess et al, 2023, 2024) and in the near future to improve the accuracy of the extragalactic Population I and Population II distance scale (Madore and Freedman, 2023, and references therein).

Moreover, the unique opportunity of using the panoramic imaging capabilities of NIRCam on board James Webb Space Telescope[15] will provide accurate NIR and

[10] https://asas-sn.osu.edu/
[11] http://ogle.astrouw.edu.pl/
[12] https://www.ztf.caltech.edu/
[13] https://www.ptf.caltech.edu/page/ptf_about
[14] https://webb.nasa.gov
[15] https://webb.nasa.gov

MIR photometry to significantly improve the accuracy of the extragalactic Population I and Population II distance scale (Madore and Freedman, 2023, and references therein).

The near-future challenge for ongoing and forthcoming optical (SDSS V[16], GALAH[17], WEAVE[18], 4MOST[19], MAVIS@VLT (Monty et al, 2021)[20]) and NIR (MOONS@VLT[21], APOGEE[22], ERIS@VLT[23], WINERED@Magellan[24]) spectroscopic surveys is to provide accurate and homogeneous abundances for iron peak, α and neutron capture elements. All of this will bring forward reliable predictionss for the impact of metallicity on pulsation properties and on the different diagnostics to estimate individual distances. In his seminal review on the absolute magnitude of CCs Bob Kraft suggested, on the basis of preliminary evidence, that MC and MW open clusters hosting CCs should cover a range in chemical compositions (Kraft, 1963). In particular, more than half century ago, he argued

Would we then be justified in assuming universality of the period-luminosity law even among so-called classical Cepheids?

This *vexata questio* has not been solved yet, but the solution, sixty years later, seems just around the corner.

iii)–Hertzsprung et similia– Homogeneous and accurate photometric data collected by microlensing (MACHO, EROS, OGLE) experiments paved the way for a new golden age for the physics of stellar oscillations and for the use of variable stars as stellar tracers. These surveys collected data mainly in a single band, plus an ancillary secondary band. The same area is going to experience a quantum jump in a couple of years thanks to the Vera C. Rubin Observatory and the LSST survey. This survey is going to observe the entire southern sky every three nights in six different photometric bands (u, g, r, i, z, y). In a time interval of ten years, the VRO will collect on average more than eighty phase point per objects in each band down to limiting magnitudes of 24–27. This will provide a complete census of helium-burning variables across the Local Group, and of CCs and Miras across the Local Volume. There will be the unique opportunity to study long-term secondary modulations (mixed-mode, Blazhko), and in particular, pulsation phenomena showing amplitude modulations over a broad range in wavelengths. In this context, the spectroscopic follow-up will play a crucial role not only to provide radial velocity measurements (low spectral resolution) and individual elemental abundances (medium/high spectral resolution), but also to further constrain the physics of variable stars. The most recent investigation concerning the phase lag between light and radial velocity curves in CCs dates back to Szabó et al (2007) and is based on a few dozen Galactic Cepheids. More accurate data can shed new light on the role that the different ionization regions play in shaping the light curves.

[16] https://www.sdss.org/
[17] https://www.galah-survey.org/
[18] https://ingconfluence.ing.iac.es/confluence/display/WEAV/The+WEAVE+Project
[19] https://www.4most.eu/cms/home/
[20] https://mavis-ao.org/mavis/
[21] https://vltmoons.org/
[22] https://www.sdss.org/instruments/apogee-spectrographs/
[23] https://www.eso.org/public/teles-instr/paranal-observatory/vlt/vlt-instr/eris/
[24] http://lihweb.kyoto-su.ac.jp/WINERED/overview_winered.html

iv)–Homogeneous spectroscopic abundances – Radial gradients appear to show quite similar trends when moving from the inner to the outer disk. Typically, they agree quite well with predictions based on chemical and on chemo-dynamical evolution models. There are a couple of exceptions like Ca among the α-elements and Y among the neutron capture elements. The current empirical and theoretical evidence do not allow us to understand whether this is a limit in the atomic data we are using for these elements, or whether they are suggesting different paths in the chemical enrichment of the thin disk. Homogeneous, high-resolution spectra based on a sizable number of lines can shed new light on the nature or nurture of the quoted elements.

It is worth mentioning that the current abundances analyses are mainly based on 1D stellar atmosphere models in LTE approximations, but the transition to spectroscopic abundances based on 3D stellar atmosphere models in NLTE approximations and with time-dependent convective energy transport is a scientific goal, achievable in the next few years (Magic et al, 2015; Chiavassa et al, 2018; Gerber et al, 2023). This transition is more difficult in dealing with Cepheids, since they experience along the pulsation cycle variations in effective temperature of several hundred degrees, in surface gravity of half dex and almost a factor two in micro-turbulent velocity (see section 6.2.1). Indeed, in a recent investigation Vasilyev et al (2019), by using radiation hydrodynamics simulations of Cepheid atmospheres (2D NLTE line formation), found a significant variation in the oxygen abundance (O I triplet at 7774 Å) along the pulsation cycle.

Moreover, large and homogeneous open cluster parameters (distance, reddening, proper motion, chemical composition) are required to trace the age dependence of the radial gradients across the thin disk. This seems well within the reach of Gaia and near future-optical/NIR spectroscopic survey.

7.2 Open problems with challenging near future solutions

Thinking about significant near-term achievements in the field of radial variables, some of the most interesting open problems appear to be the following.

i)–To loop or not to loop?– We are still missing the micro and macro physics driving the morphology of the blue loops. The same drawback applies to the efficiency of the mass loss during the red giant branch phase. Therefore, the comparison between predicted and observed period distributions does depend on the physical assumptions adopted to deal with these phenomena.

ii)–What is the physical mechanism driving the occurrence of bump Cepheids?– In spite of the paramount theoretical and observational effort, we still lack *ab initio* calculations to explain the occurrence of secondary features (bumps, dips) along the pulsation cycle.

iii)–What is the physical mechanism driving the occurrence of mixed-mode Cepheids? Is there any connection with Blazhko RR Lyrae?– The same outcome applies to the physical mechanism(s) driving the occurrence of secondary modulations. In particular, it is not clear whether the secondary modulations present in RR Lyrae and in Cepheids have a common origin.

iv)–Reddening estimates– Accurate estimates of the extinction in low and high reddened regions has been one the toughest problems in quantitative astrophysics.

Even in the era of Gaia, as well as of large spectroscopic surveys, we are dealing with this long-standing problem. A significant and quantitative improvement has been provided by diffuse interstellar bands (Munari et al, 2008; Zhao et al, 2021; Saydjari et al, 2022), but this approach requires at least medium resolution spectra. The photometric diagnostics based either on variables stars, (Sturch, 1978) or on narrow-band photometry (Strömgren) require large amount of telescope time. A diagnostic that is solid and easy to use is still lacking.

8 Summary and future developments

This review deals with different aspects of Cepheid variable stars. the content can be split into five different broad topics.

Phenomenology of variable stars– Ongoing space (Gaia, WISE) and ground-based long-term variability surveys (OGLE IV) provided the opportunity to investigate the phenomenology of variable stars. In particular, the occurrence of single and mixed-mode variables in the MW and in the Magellanic Clouds. This means a detailed investigation of the diagnostics adopted for the identification (periods, pulsation amplitudes, shape of the light curves) of the pulsation mode. Moreover, the opportunity to use homogeneous data for the three different stellar systems, characterized by different chemical enrichment histories, allowed us to investigate the dependence of the pulsation parameters on the metal content. The circumstantial evidence concerning the pulsation parameters are the following.

The period distribution of CCs steadily moves towards shorter periods when moving from more metal-rich (MW) to more metal-poor (SMC) stellar systems. Moreover, the mean colors of CCs become systematically bluer for a decrease in the metal content.

The luminosity amplitude for FU and FO CCs display well-defined primary and secondary peaks moving towards shorter periods for a decrease in the metal content.

The use of different populations ratios among single-mode variables and/or among mixed-mode variables provide an unique opportunity to analyze, on a quantitative basis, pulsation (topology of the instability strip) and evolutionary (the stars formation episodes) properties, together with the chemical enrichment histories of the different stellar systems.

i)–The population ratio between second overtone and fundamental CCs decreases for an increase in metallicity (0.03 [SMC] vs 0.01 [LMC]) and it is vanishing for the MW. The fraction of mixed-mode variables, instead, does not seem to depend on metallicity (0.11±0.01, [SMC]; 0.17±0.01, [LMC]; 0.14±0.01, [MW]).

ii)–The population ratio between first overtone and fundamental ACs is clearly higher in the MW (0.76±0.11) than in the SMC (0.54±0.10) and in the LMC (0.44±0.08). However, the MC sample is limited and affected by large Poissonian uncertainties.

iii)–The relative number of different subgroups of TIICs does display a positive trend with metallicity for BLHer (0.28±0.01, [SMC]; 0.34±0.01, [LMC]; 0.38±0.02, [MW]) and a negative one for WVir (0.51±0.01, [SMC]; 0.46±0.01, [LMC]; 0.43±0.02, [MW]). On the other hand, the fraction of RVTau remains, within

the errors, constant: 0.21±0.01 (SMC), 0.19±0.01 (LMC) and 0.19±0.01 (MW). Note that only a few FOs have been currently identified among MW and MC TIICs.

Hertzsprung progression– A detailed analysis of the pulsation amplitude and of the difference between the bump and the minimum in luminosity, together with their difference in phase, allowed us to investigate on a quantitative basis the occurrence of the Hertzsprung progression in MW and Magellanic CCs. The pulsation amplitudes were adopted because, in a specific period range, the maximum of the light curve is given by the bump rather than by the pulsation maximum. We found that the center of the Hertzsprung progression is anti-correlated with the metal content. Indeed, the center moves from P(HP)=9.0 ± 0.2 days in the MW to P(HP)=9.4 ± 0.2 days in the LMC and to P(HP)=10.0 ± 0.2 days in the SMC.

Evolutionary constraints for Cepheids– The evolutionary properties of Cepheids were investigated by using optical, optical-NIR and NIR color–magnitude diagrams. In order to overcome possible systematics, we adopted homogeneous optical (OGLE IV) and NIR (IRSF) photometry for both variable stars and common stars in the MW and in the MCs. The comparison between observations and theory was performed by using homogeneous sets of stellar isochrones and evolutionary models available in the BASTI-IAC data base. The key advantage of this database is that we adopted cluster isochrones, either considering or neglecting convective core overshooting during central hydrogen-burning phases. Moreover, evolutionary predictions are available for scaled-solar and α-enhanced chemical mixtures. This is a crucial issue in dealing with young (CCs), intermediate (ACs) and old (TIICs) stellar tracers. The comparison provides ranges in age and in metallicity for the three different groups of variable stars, which agree quite well with similar estimates available in the literature.

We have studied in detail the transition between stellar structures that ignite helium in a core partially affected by electron degeneracy, and those that ignite helium quiescently. This difference marks the transition between low- and intermediate-mass stars. It goes without saying that the two groups obey to different mass-luminosity relations. The current circumstantial evidence indicates that the bright portion of the ACs is located across this boundary. This means that the brightest ACs are quite similar to CCs, whereas the others are the truly Anomalous Cepheids.

It is worth mentioning that the central hydrogen-burning evolutionary time in the quoted transition is only a factor of four longer than the central helium-burning lifetime. The hydrogen-burning lifetime is typically two order of magnitude longer in the low-mass regime, and roughly 6/8 times longer in the intermediate-mass regime. This is why stellar structures in the transition between low- and intermediate-mass stars are the main contributors of central helium-burning stellar populations (red clump stars).

We have also examined the impact of the first dredge-up among different evolutionary scenarios (classical, overshooting) to trace its efficiency. We further support the use of CNO abundances as a solid diagnostic to discriminate among the different physical assumptions driving the mixing during central hydrogen-burning phases in intermediate-mass stars.

Cepheids as primary distance indicators– The use of the different diagnostics have been investigated in detail. The current evidence based on MC Cepheids fully support the use of FOs as distance indicators. Moreover, pros and cons of different distance diagnostics PL, PW and PLC were addressed on a quantitative basis. We also discussed advantages and drawbacks in using optical, optical-NIR and NIR mean magnitudes.

Cepheids as stellar tracers– We studied the use of MW CCs as young stellar tracers of the Galactic thin disk. The current evidence indicates well-defined negative radial gradients in iron peak, α- and neutron capture elements. The only exception is barium, and we still lack a quantitative explanation. Plain physical arguments suggest that the chemical enrichment has been more efficient in the high-density regions of the inner disk, and then moved into the outermost disk regions (Spitoni et al, 2019; Matteucci, 2021, and references therein). Preliminary evidence based on both CCs and open clusters indicates a flattening of the gradient in the outskirts of the thin disk. This global trend is only minimally affected by the flaring of the disk (Lemasle et al, 2022).

Spectroscopic measurements based on high-resolution spectra indicate that the slopes of several α-elements are quite similar to the slope of iron. Indeed, the trend of the [α/Fe] abundance ratio is mildly positive across the disk. This suggests a similar chemical enrichment history. This evidence is further supported by the radial gradients of s- (La, Ce, Nd) and r- (Eu) process elements. The slopes of these elements are steeper than those of the α-elements, and the [n-capture/Fe] abundance ratios are slightly more positive across the entire disk. There is only one exception: Y shows a slope quite similar to iron, and in turn, the [Y/Fe] abundance ratio is flat.

Interestingly enough, the same abundance ratios display a flat trend as a function of the age (logarithmic period). The pulsation period is a solid analog of the individual age of CCs, since the longer the period, the younger is the Cepheid. Therefore, the chemical enrichment history of CCs has been quite homogeneous during the last 200/300 Myrs. There is one exception: Ca, showing a mild positive gradient as a function of the period. The positive gradient in [Ca/H] versus period and the negative gradient of [Ca/H] vs Galactocentric distance are not related, since outer disk CCs have a canonical period distribution.

Acknowledgments. We are grateful to two anonymous referees for their positive words concerning the content and the cut of an earlier version of the present paper, and for their very relevant suggestions, which improved its readability. They also provided specific and appropriate hints on a couple of sections which improved the content of the paper. Special thanks to G. Giobbi for her valuable editing of the manuscript and V. D'Orazi, G. Fiorentino, M. Marconi, N. Matsunaga and M. Salaris, for their detailed suggestions concerning the content and the layout of an early version of this manuscript. We are also happy to acknowledge informative interchanges and many interesting conversations with D. Lennon, W. Freedman, B. Madore, A. Udalski and their collaborators over more than 20 years.

It is a real pleasure to thank the many colleagues that supported me with suggestions and advice along my research activity (V. Castellani, F. Caputo, R. Buonanno,

R.F. Stellingwerf, A.J. Cox, P.B. Stetson, H. Smith, A.R. Walker, C. Sneden, H.-R. Kudritzki). Special thanks to my long-standing collaborators—M. Marconi, M. Dall'Ora, M. Monelli, M. Fabrizio, R. da Silva, B. Lemasle, L. Inno, V. D'Orazi, M. Marengo, J. Mullen, F. Thevenin, J. Storm, B. Chaboyer, S. Cassisi, M. Salaris, G. Coppola, V. Ripepi, I. Musella, M. di Criscienzo, G. Fiorentino, C. E. Martinez Vazquez, N. Matsunaga, W. Gieren, G. Pietrzynski, B. Pilecki, V. Kovtyukh, M. Tantalo, E. Valenti, M. Zoccali—who made and are still making the research in this field a fantastic adventure.

I am immensely grateful to my original family and to my current family, and in particular to F^2G^2, they never pointed me out for the many absences for astrophysical *otium*. This paper is dedicated to Francesco, who made our recent life "really something special". Special thanks to the A&A Review editorial board, and in particular, to Francesca Matteucci, Bengt Gustafsson and Frank Schulz for this unique opportunity, and for being so patient with us over many years. This investigation was partially supported by Project PRIN MUR 2022 (2022ARWP9C) "Early Formation and Evolution of Bulge and HalO (EFEBHO)", PI: M. Marconi, funded by European Union – Next Generation EU and by the Large grant INAF 2022 MOVIE (PI: M. Marconi). This research was also partially supported by the Munich Institute for Astro–Particle and BioPhysics (MIAPbP) which is funded by the Deutsche Forschungsgemeinschaft(DFG,GermanResearch Foundation) under Germany´s Excellence Strategy – EXC-2094 – 390783311.

Appendix A Metallicity dependence of the Hertzsprung progression

In order to investigate on a more quantitative basis the variation of the bump among UPDB and DORB Cepheids, Figs. A1 and A2 display the *I*-band light curves for LMC and Galactic bump Cepheids.

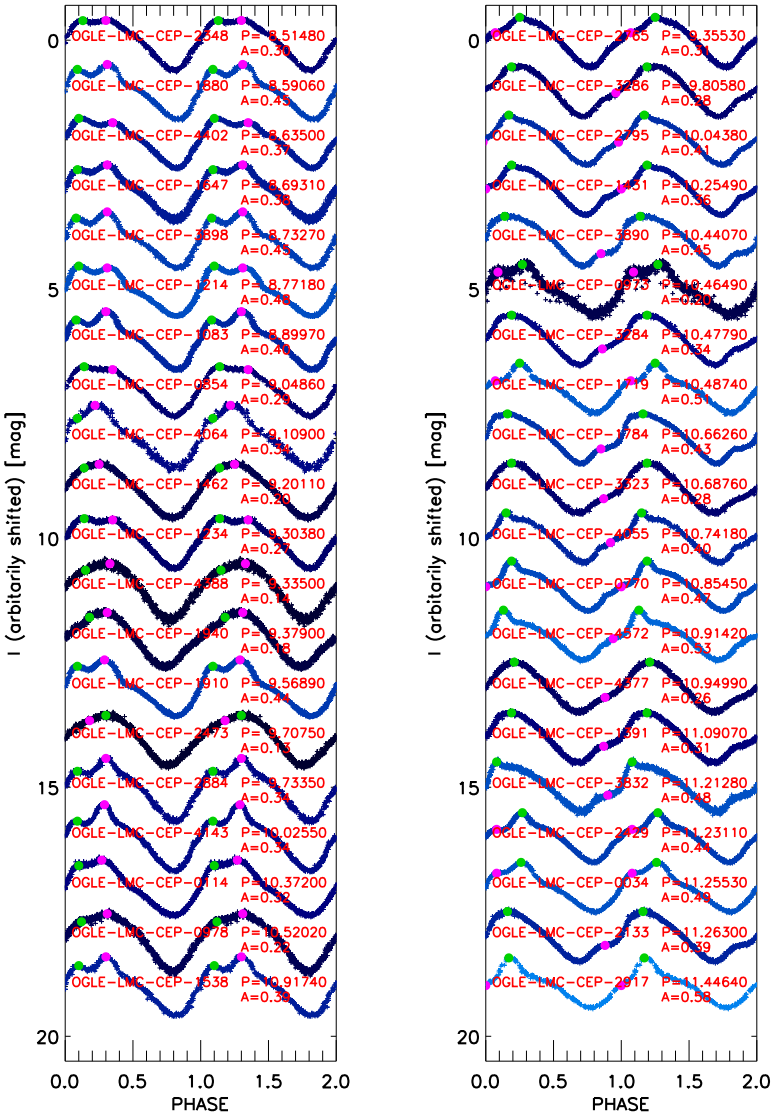

Fig. A1 Phased *I*-band light curves of LMC bump Cepheids with a bump moving either up along the decreasing branch (UPDB) or down along the rising branch (DORB).

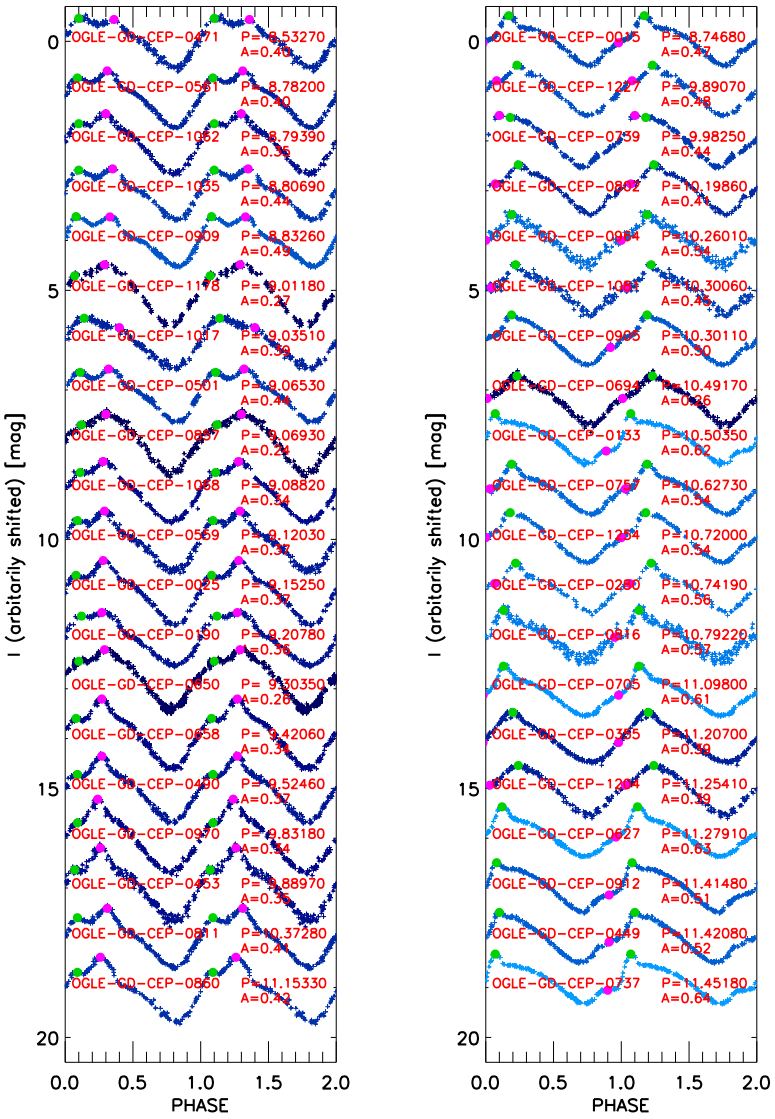

Fig. A2 Phased *I*-band light curves of LMC bump Cepheids with a bump moving either up along the decreasing branch (UPDB) or down along the rising branch (DORB).

Moreover, we also estimated the difference in phase between the pulsation maximum and the minimum in luminosity (ΦPuls) and the difference in phase between the bump and the minimum in luminosity (Φbump). Data plotted in the top panels of Fig. A3 show that UPDB Cepheids (squares) are characterized by an almost constant phase difference between the pulsation maximum and the minimum. The mean value are, within the errors, quite similar (0.26±0.02, SMC; 0.29±0.03, LMC; 0.30±0.03,

MW) when moving from the more metal-poor to the more metal-rich stellar systems. In the MCs there are a few outliers which attain larger values, but they are typically located beyond the HP.

Conversely, the DORB Cepheids (diamonds) display a steady decrease from ≈0.50 to ≈0.30 when moving from the short- to the long-period range. There is a range in period between 9.5 and 11 days in which the two subgroups overlap with each other. However, the separation between UPDB and DORB Cepheids, with the exception of a few transitional objects, appears quite clear.

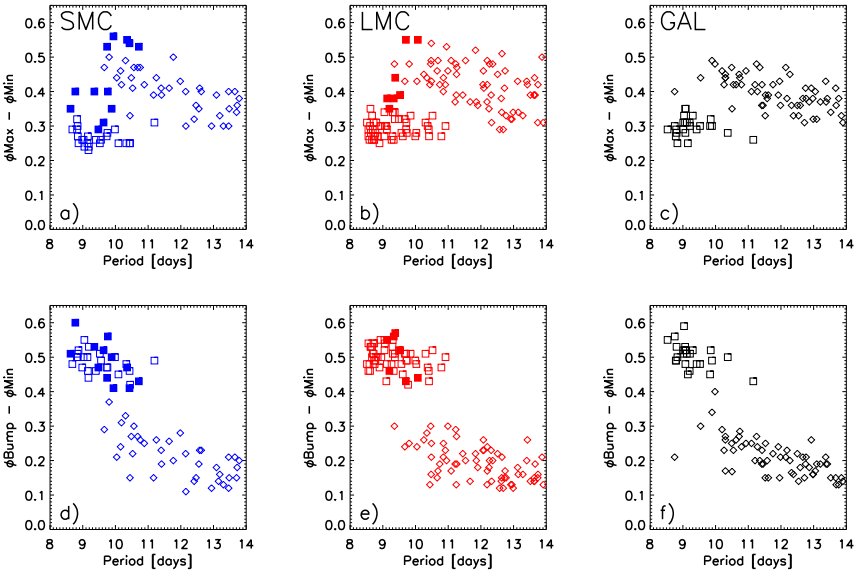

Fig. A3 Top: from left to right difference between the phase of the maximum and the phase of the minimum in *I*-band light curves as a function of the period for SMC (panel a), LMC (panel b) and Galactic (panel c) bump Cepheids. Squares and diamonds mark UPDB and DORB Cepheids. Bottom: Same as the top, but the difference is between the phase of the bump and the phase of the minimum along *I*-band light curves (SMC, panel d; LMC, panel e; Galactic, panel f).

The bottom panels of the same figure display the difference between the phase of the bump and the phase of the minimum in the *I*-band light curve. The separation between UPDB and DORB Cepheids becomes even clearer. Indeed, the UPDBs are clustering around a constant mean value ranging from 0.49±0.02 (SMC) to 0.50±0.03 (LMC) and to 0.51±0.03 (MW). The DORBs show a steady decrease when moving from the short- to the long-period range. Once again, the two subgroups display an overlap for periods ranging from 9.5 to 11 days, but they differ on average by a factor of two.

In order to further investigate on a quantitative basis the difference between the UPDB and DORB Cepheids, the top panels of Fig. A4 display the difference in magnitude between the pulsation maximum and the minimum in the *I*-band light curve (pulsation amplitude, ΔPuls). In this context, it is worth mentioning that ΔPuls is

not always the luminosity amplitude, i.e. the difference in magnitude between the absolute maximum and the minimum along the light curve. Indeed, there is a range in period in which the bump is brighter than the pulsation maximum (see Figs. 11, A1 and A2). Data plotted in these panels display quite clearly that the pulsation amplitudes attain a minimum that steadily decreases from 9.5–10 days for the SMC to 9.0–9.5 days for the LMC and to ≈9.0 days for the Galactic UPDB Cepheids (squares). The DORB Cepheids (diamonds) display a steady increase when moving from the short to the long-period regime, and the global trend is steeper when moving from metal-poor to more metal-rich stellar systems. They are characterized by a large spread at fixed pulsation period, but the spread in magnitude is intrinsic, because it is well beyond the typical photometric error along the light curve.

The center of the HP in the MW and in the MCs were marked with vertical black lines in Fig. A4. Data plotted in this figure display some outliers across the minimum. This variation across the center of the HP is intrinsic and expected. Indeed, MC and MW CCs are characterized by a well defined metallicity distribution, with a standard deviation of the order of 0.5 dex (Romaniello et al, 2008; Hocdé et al, 2022). In a recent investigation, Romaniello et al (2022) by using high resolution spectra of 89 LMC CCs suggested that the spread in iron abundance is quite modest. However, spectroscopic measurements based on B-type stars (Hunter et al, 2009) and on red giants (Dobbie et al, 2014) indicate a spread in chemical composition larger than 0.5 dex.

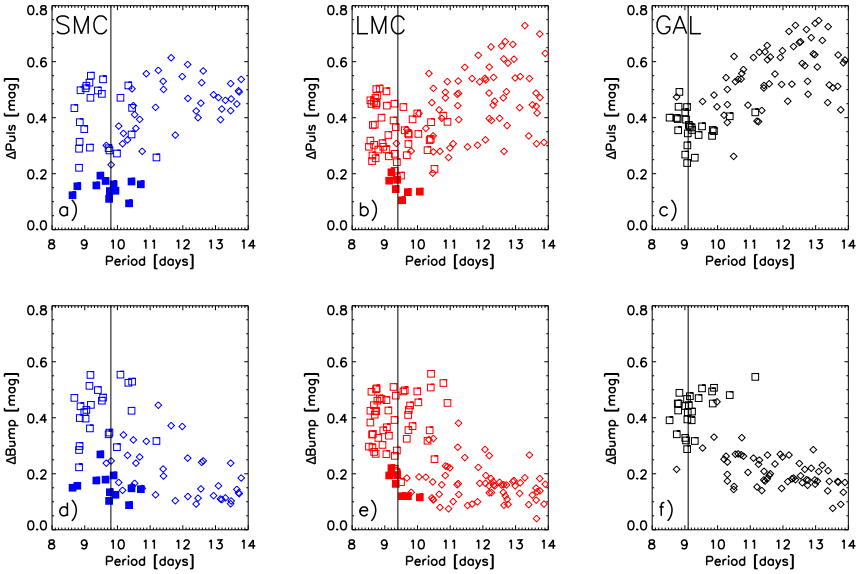

Fig. A4 Top: from left to right difference between the pulsation maximum and the minimum in the *I*-band light curves as a function of the period for SMC (panel a), LMC (panel b) and Galactic (panel c) bump Cepheids. The black vertical line shows the center of the HP. The symbols are the same as in Fig. A3. Bottom: Same as the top, but the difference is between the magnitude of the bump and the minimum along *I*-band light curves (SMC, panel d; LMC, panel e; Galactic, panel f).

The difference in magnitude between the bump and the minimum versus the pulsation period (bottom panels of Fig. A4) display an opposite trend. The UPDB Cepheids attain, as expected, the largest amplitudes, while DORB Cepheids show once again a steady decrease when moving from the short- to the long-period range. The bump Cepheids that trace the center of the HP, i.e. those with the smallest pulsation amplitudes, attain also the smallest bump amplitudes. However, the minimum is less clear, since UPDBs and DORBs partially overlap across the HP.

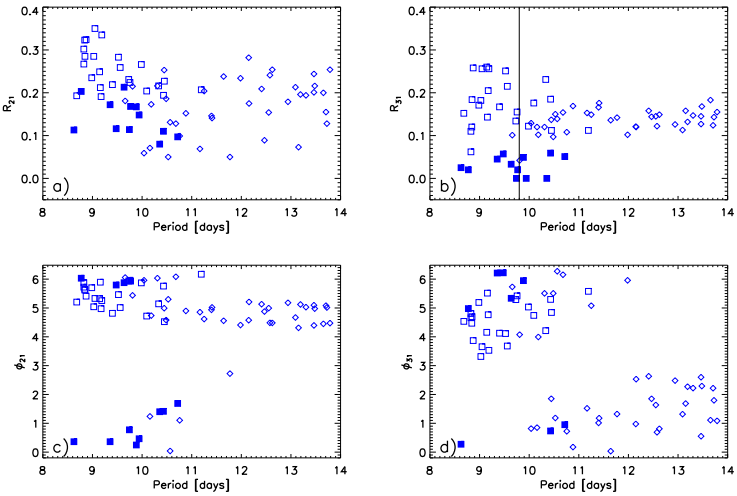

Fig. A5 Top: R_{21} (panel a) and R_{31} (panel b) Fourier parameters as a function of the pulsation period for I-band light curves of SMC bump Cepheids provided by OGLE IV. The symbols are the same as in Fig. A3. Bottom: Same as the top, but for ϕ_{21} (panel c) and ϕ_{31} (panel d) Fourier parameters .

The current findings concerning the use of the Bailey (pulsation amplitude) and pseudo-Bailey (difference in magnitude between the bump and the minimum) diagrams together with the phase difference diagrams allow us to further constrain the use of the Fourier parameters to trace the variation of the shape of the light curves across the HP. In order to analyze this issue in depth by using homogeneous and accurate estimates of the Fourier parameters, we took advantage of the Fourier analysis provided by OGLE IV (Soszyński et al, 2015a,b, 2017b, 2018). Data plotted in the top panels of Fig. A5, A6 and A7 display that the R_{21} (left) and the R_{31} (right) Fourier parameters associated with the amplitudes of the first three harmonics display either a mild quadratic trend (R_{21}), or an almost constant value (R_{31}) across the entire period range of the HP. The top right panels of these figures show that the R_{31} parameter shows minima similar to the minima we identified by using the difference in magnitude between pulsation maximum and minimum and the difference between bump and minimum. In order to help the eye identify the minima, we plotted the same black vertical lines plotted in Fig. A4. This suggests that the R_{31} parameter is a solid diagnostic to constrain the center of the HP.

The trend of the phase difference among the same harmonics, plotted in the bottom panels of the same figure, shows several interesting features. The distribution of the ϕ_{21} (left) has a wedge shape with two well-defined sequences. The horizontal sequence, which attains the largest values and it is almost constant over the entire period range, while the slant sequence moves from the center of the HP and approaches the horizontal sequence in the long-period range. The UPDB Cepheids partially overlap with DORB Cepheids. As a whole, the ϕ_{21} parameter does not seem to be a solid diagnostic to constrain the center of the HP. The separation between UPDBs and DORBs showed by the ϕ_{31} Fourier parameter plotted in the bottom right panel is a very solid diagnostic to separate bump Cepheids.

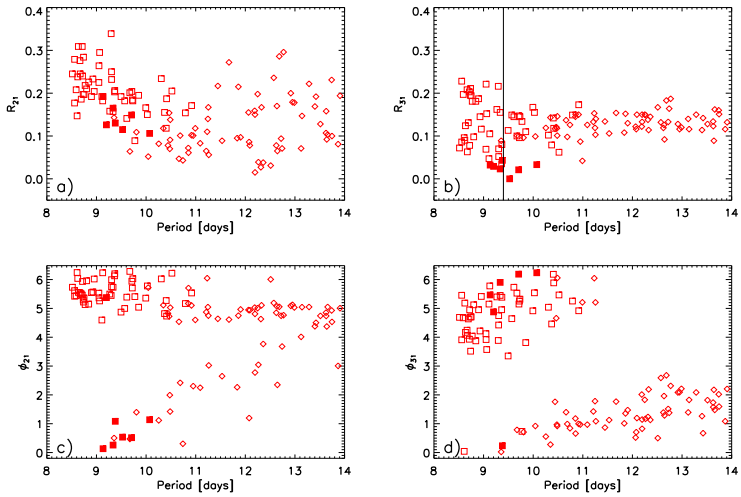

Fig. A6 Top: R_{21} (panel a) and R_{31} (panel b) Fourier parameters as a function of the pulsation period for I-band light curves of LMC bump Cepheids provided by OGLE IV (R_{21}, panel a; and R_{31}, panel b). Symbols are the same as in Fig. A3. Bottom: Same as the top, but for ϕ_{21} (panel c) and ϕ_{31} (panel d) Fourier parameters.

The key difference in the comparison between the Bailey and the pseudo-Bailey diagram with the R_{21} (left) and the R_{31} Fourier parameters is that the latter attain very similar values when moving from MC to Galactic Cepheids, whereas the former ones display a clearer trend when moving from more metal-poor to more metal-rich stellar systems. A similar outcome applies to the comparison between the phase difference of pulsation maximum and of the bump with the ϕ_{21} and ϕ_{31} Fourier parameters. The former parameters display well separated linear trends for Cepheids, with a bump located either along the decreasing or the rising branch of the light curve.

In closing this section it is worth mentioning that the HP can be considered as the fingerprint of CCs. To our knowledge there is no other group of variable stars showing a tight correlation of the phase of a secondary feature along the light and

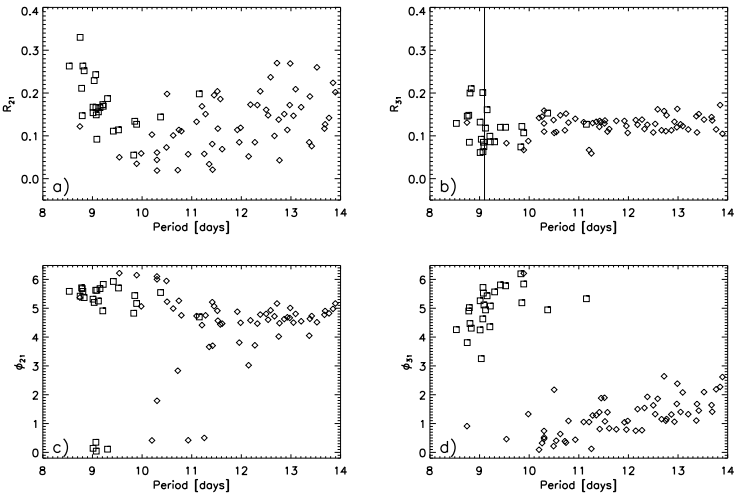

Fig. A7 Top: R_{21} (panel a) and R_{31} (panel b) Fourier parameters as a function of the pulsation period for I-band light curves of Galactic bump Cepheids provided by OGLE IV (R_{21}, panel a; R_{31}, panel b). Symbols are the same as in Fig. A3. Bottom: Same as the top, but for ϕ_{21} (panel c) and ϕ_{31} (panel d) Fourier parameters.

the radial velocity curves with a specific range of pulsation periods. This outcome applies to MW, MC and to extragalactic CCs.[25]

[25]This paragraph was triggered by a chat we have had with Adam Riess concerning the evolutionary and pulsation properties of extragalactic Cepheids.

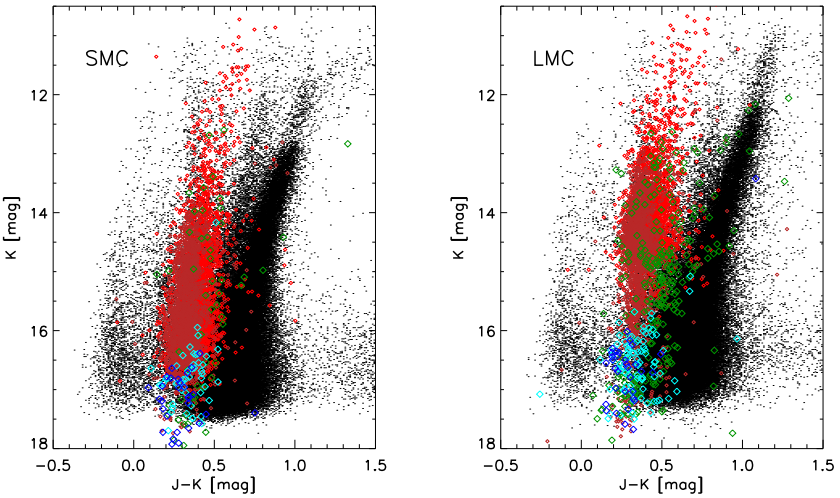

Fig. A8 Left: distribution of fundamental (light red) and first overtone (dark red) CCs, fundamental (light blue) and first overtone (dark blue) ACs and fundamental (green) TIICs in the NIR K,$J-K$ CMD of the SMC. The overlap among the different groups of Cepheids is even more severe, due to the reduced sensitivity of the $J-K$ color to the effective temperature. Data plotted in this panel come from the IRSF survey of the Magellanic Clouds (Ita et al, 2004, 2018). The mean magnitudes of variable stars were estimated as the mean of the measurements in magnitude. Right: Same as the left, but for LMC Cepheids.

Appendix B Optical/near-infrared and near-infrared diagnostics

B.1 Color magnitude diagrams

This section deals with optical/NIR and NIR diagnostics, namely the K,$V-K$ and the K,$J-K$ CMDs of MC stellar populations discussed in Sect. 4. Moreover, the K-band PL relations and the K,$J-K$ PW relations are further investigated (see Sect. 6.2). Figure A8 shows the same variables discussed in section~4, but in the NIR K,$J-K$, CMD. Data for both static and variables stars come from the NIR photometric survey of the MCs performed by IRSF (Ita et al, 2004, 2018). The mean magnitude of variable stars is the mean of the measurements. Data plotted in this figure display quite clearly that the degeneracy among the different groups of variable stars and common stars is even more severe, since they overlap over a significant fraction of the CMD. The difference with optical CMDs is mainly due to the reduced sensitivity of NIR colors to the effective temperature of F,G and early K-type stars. Moreover, limiting magnitudes in NIR photometry are shallower than in the optical regime, and evolutionary features such as the RC can hardly be recognized.

To partially ease this difficulty, Fig. B9 shows the same variables, but plotted in the optical-NIR K,$V-K$ CMD. There is still some overlap between static and variable stars, but the increased sensitivity to the effective temperature provides a

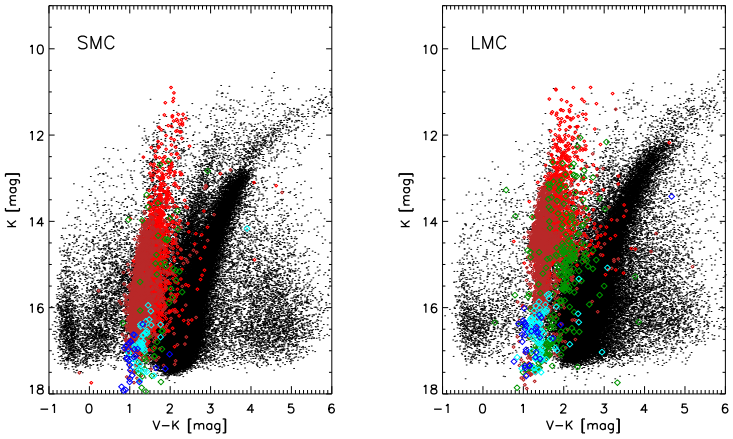

Fig. B9 Left: distribution of fundamental (light red) and first overtone (dark red) CCs, fundamental (light blue) and first overtone (dark blue) ACs and fundamental (green) TIICs in the Optical-NIR K,$V-K$ CMD of the SMC. The different groups of Cepheids are more separated, due to the increased sensitivity of the $V-K$ color to the effective temperature. Right: Same as the left, but for LMC Cepheids.

better separation of the different groups of variable stars. Indeed, they cover a range in color which is at least a factor of four larger when compared with the optical CMD. Moreover, the distribution in magnitude and in color is significantly more linear, since they become intrinsically brighter when moving from hotter (shorter periods) to cooler (longer periods) variables.

B.2 Period-Luminosity and Period-Wesenheit relations

This subsection deals with NIR and optical-NIR diagnostics to estimate individual Cepheid distances. Data plotted in Fig. B10 clearly show the advantages in using NIR mean magnitudes. The spread for both FO and FU Cepheids is, at fixed pulsation period, systematically smaller and the slope becomes systematically steeper (see Table B1). The same trend also applies to optical, optical-NIR and NIR PW relations (see Table B2).

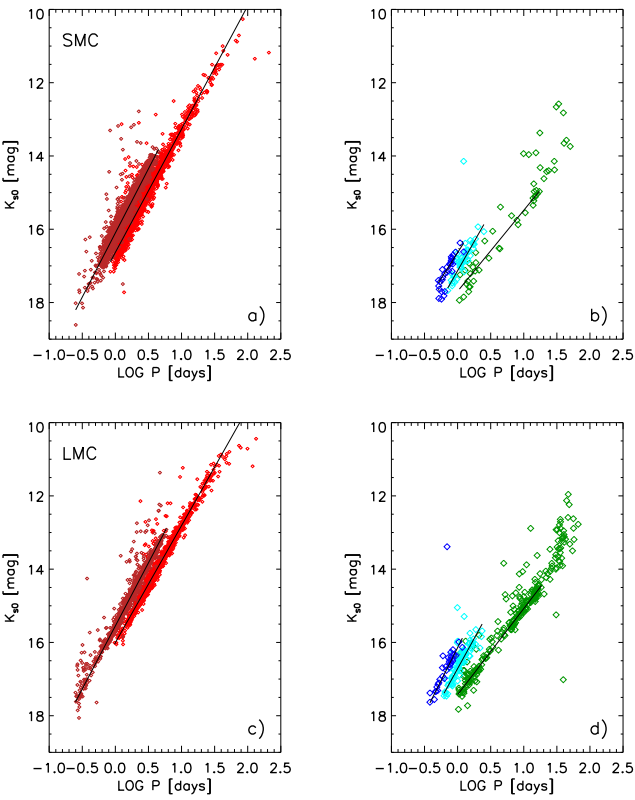

Fig. B10 Top: Dereddened *K*-band PL relations (see Table B1) of SMC CCs (left) and ACs plus TIICs (right). From shorter to longer periods, the dark red and the light red symbols display FO and FU CCs, while the dark blue and the light blue symbols display FO and FU ACs and the green symbols the FU TIICs. The solid black lines display the linear fits to the PL relations. Bottom: Same as the top, but for LMC Cepheids

Table B1 Optical and NIR PL relations ($M_X = a + b \times \log P$) for Magellanic Cloud Cepheids.

band	mode	a[1]	b	ϵ_a	ϵ_b	σ
		—SMC CCs—				
V	FO	17.155	–3.143	0.008	0.033	0.282
I	FO	16.723	–3.299	0.006	0.026	0.231
J	FO	16.388	–3.398	0.006	0.024	0.205
H	FO	16.162	–3.537	0.006	0.023	0.179
K	FO	16.101	–3.501	0.005	0.021	0.184
V	FU	17.783	–2.907	0.009	0.018	0.267
I	FU	17.315	–3.128	0.007	0.014	0.214
J	FU	16.935	–3.211	0.006	0.013	0.202
H	FU	16.701	–3.376	0.006	0.013	0.186
K	FU	16.633	–3.365	0.005	0.011	0.172
		—SMC ACs—				
V	FO	17.601	–2.370	0.048	0.344	0.171
I	FO	17.216	–2.585	0.033	0.237	0.120
J	FO	16.825	–2.859	0.027	0.214	0.055
H	FO	16.540	–3.836	0.044	0.258	0.074
K	FO	16.638	–2.820	0.044	0.272	0.124
V	FU	18.173	–2.256	0.031	0.208	0.233
I	FU	17.674	–2.233	0.018	0.113	0.105
J	FU	17.392	–2.887	0.023	0.148	0.111
H	FU	17.095	–2.649	0.069	0.393	0.230
K	FU	17.132	–3.175	0.024	0.153	0.121
		—SMC TIICs—				
V	FU	18.885	–1.677	0.092	0.127	0.325
I	FU	18.401	–1.913	0.078	0.108	0.276
J	FU	17.973	–2.027	0.080	0.112	0.286
H	FU	17.705	–2.113	0.122	0.170	0.355
K	FU	17.694	–2.211	0.070	0.097	0.248
		—LMC CCs—				
V	FO	16.618	–3.241	0.007	0.018	0.187
I	FO	16.207	–3.317	0.005	0.013	0.135
J	FO	15.829	–3.364	0.004	0.011	0.115
H	FO	15.614	–3.475	0.004	0.011	0.094
K	FO	15.549	–3.441	0.003	0.009	0.089
V	FU	17.056	–2.690	0.011	0.016	0.180
I	FU	16.660	–2.924	0.008	0.012	0.123
J	FU	16.266	–3.013	0.007	0.011	0.124
H	FU	16.094	–3.232	0.007	0.011	0.117
K	FU	16.006	–3.195	0.005	0.008	0.086
		—LMC ACs—				
V	FO	16.988	–3.416	0.065	0.316	0.236
I	FO	16.679	–3.362	0.046	0.214	0.168
J	FO	16.354	–3.390	0.047	0.224	0.152
H	FO	16.219	–3.504	0.064	0.264	0.158
K	FO	16.143	–3.603	0.029	0.136	0.079
V	FU	17.719	–2.582	0.028	0.186	0.252
I	FU	17.353	–2.921	0.018	0.122	0.162
J	FU	16.980	–3.136	0.020	0.139	0.162
H	FU	16.754	–3.311	0.015	0.102	0.080
K	FU	16.715	–3.284	0.015	0.112	0.122
		—LMC TIICs—				
V	FU	18.414	–1.602	0.036	0.046	0.262
I	FU	18.041	–1.954	0.022	0.028	0.170
J	FU	17.601	–2.063	0.027	0.034	0.192
H	FU	17.497	–2.326	0.035	0.043	0.206
K	FU	17.428	–2.352	0.017	0.021	0.109

From left to right the columns list the photometric band, the mode, the zero-point, the slope and their uncertainties and the standard deviation (mag).

[1]To obtain the absolute zero points, one should subtract the geometrical distance modulus of the LMC and SMC, based on eclipsing binaries (18.477±0.026 mag and 18.977±0.028 mag for the LMC and SMC, respectively, (Pietrzyński et al, 2019; Graczyk et al, 2020))

Table B2 Optical, NIR and optical–NIR PW relations ($M_X = a + b \times \log P + c \times CI$) for Magellanic Cloud Cepheids.

band/CI	mode	a[1]	b	ϵ_a	ϵ_b	c	σ
			—SMC CCs—				
$I, V-I$	FO	15.966	–3.570	0.005	0.020	1.550	0.173
$J, V-J$	FO	16.064	–3.554	0.005	0.022	0.406	0.186
$H, V-H$	FO	15.940	–3.642	0.005	0.021	0.217	0.165
$K, V-K$	FO	15.956	–3.569	0.005	0.021	0.134	0.174
$K, I-K$	FO	15.949	–3.570	0.005	0.020	0.250	0.175
$K, J-K$	FO	15.904	–3.576	0.005	0.021	0.690	0.178
$K, V-I$	FO	16.047	–3.528	0.005	0.021	0.288	0.179
$I, V-I$	FU	16.491	–3.457	0.005	0.011	1.550	0.159
$J, V-J$	FU	16.580	–3.359	0.006	0.013	0.406	0.187
$H, V-H$	FU	16.450	–3.471	0.006	0.013	0.217	0.184
$K, V-K$	FU	16.473	–3.429	0.005	0.011	0.134	0.163
$K, I-K$	FU	16.468	–3.432	0.005	0.011	0.250	0.164
$K, J-K$	FU	16.422	–3.466	0.005	0.011	0.690	0.172
$K, V-I$	FU	16.573	–3.396	0.005	0.011	0.288	0.166
			—SMC ACs—				
$I, V-I$	FO	16.517	–3.470	0.026	0.150	1.550	0.083
$J, V-J$	FO	16.519	–3.217	0.062	0.381	0.406	0.143
$H, V-H$	FO	16.299	–4.136	0.044	0.236	0.217	0.075
$K, V-K$	FO	16.502	–2.763	0.045	0.267	0.134	0.119
$K, I-K$	FO	16.343	–3.674	0.018	0.110	0.250	0.037
$K, J-K$	FO	16.424	–2.776	0.048	0.286	0.690	0.128
$K, V-I$	FO	16.627	–2.527	0.043	0.261	0.288	0.100
$I, V-I$	FU	16.936	–2.918	0.017	0.114	1.550	0.121
$J, V-J$	FU	17.053	–3.042	0.027	0.175	0.406	0.134
$H, V-H$	FU	16.842	–2.680	0.078	0.442	0.217	0.259
$K, V-K$	FU	16.981	–3.234	0.025	0.159	0.134	0.126
$K, I-K$	FU	16.976	–3.252	0.024	0.159	0.250	0.126
$K, J-K$	FU	16.912	–3.158	0.022	0.145	0.690	0.108
$K, V-I$	FU	17.073	–3.195	0.024	0.156	0.288	0.124
			—SMC TIICs—				
$I, V-I$	FU	17.554	–2.309	0.056	0.079	1.550	0.201
$J, V-J$	FU	17.604	–2.193	0.079	0.111	0.406	0.283
$H, V-H$	FU	17.470	–2.244	0.124	0.173	0.217	0.361
$K, V-K$	FU	17.536	–2.290	0.067	0.094	0.134	0.239
$K, I-K$	FU	17.527	–2.291	0.069	0.097	0.250	0.247
$K, J-K$	FU	17.502	–2.338	0.072	0.101	0.690	0.257
$K, V-I$	FU	17.635	–2.249	0.067	0.093	0.288	0.238
			—LMC CCs—				
$I, V-I$	FO	15.396	–3.437	0.003	0.008	1.550	0.079
$J, V-J$	FO	15.479	–3.448	0.004	0.010	0.406	0.099
$H, V-H$	FO	15.377	–3.538	0.004	0.010	0.217	0.083
$K, V-K$	FO	15.398	–3.490	0.003	0.009	0.134	0.079
$K, I-K$	FO	15.389	–3.493	0.003	0.009	0.250	0.082
$K, J-K$	FO	15.355	–3.502	0.003	0.009	0.690	0.082
$K, V-I$	FO	15.503	–3.465	0.003	0.009	0.288	0.086
$I, V-I$	FU	15.889	–3.315	0.005	0.008	1.550	0.077
$J, V-J$	FU	15.922	–3.183	0.007	0.011	0.406	0.120
$H, V-H$	FU	15.858	–3.352	0.008	0.012	0.217	0.120
$K, V-K$	FU	15.850	–3.263	0.005	0.007	0.134	0.078
$K, I-K$	FU	15.844	–3.269	0.005	0.008	0.250	0.079
$K, J-K$	FU	15.812	–3.299	0.005	0.008	0.690	0.091
$K, V-I$	FU	15.961	–3.233	0.005	0.008	0.288	0.082

continued on next page

Table B2 continued.

band/CI	mode	a[1]	b	ϵ_a	ϵ_b	c	σ
			—LMC ACs—				
$I, V-I$	FO	16.012	–3.475	0.038	0.183	1.550	0.127
$J, V-J$	FO	16.088	–3.380	0.045	0.225	0.406	0.142
$H, V-H$	FO	16.003	–3.690	0.076	0.326	0.217	0.181
$K, V-K$	FO	16.060	–3.462	0.030	0.152	0.134	0.089
$K, I-K$	FO	16.022	–3.535	0.028	0.133	0.250	0.074
$K, J-K$	FO	16.025	–3.355	0.037	0.172	0.690	0.115
$K, V-I$	FO	16.112	–3.610	0.030	0.148	0.288	0.079
$I, V-I$	FU	16.578	–2.825	0.014	0.089	1.550	0.108
$K, J-K$	FU	16.514	–3.327	0.016	0.120	0.406	0.131
$K, V-K$	FU	16.573	–3.396	0.016	0.115	0.217	0.123
$K, V-I$	FU	16.669	–3.332	0.016	0.113	0.134	0.123
$K, I-K$	FU	16.557	–3.233	0.017	0.119	0.250	0.136
$J, V-J$	FU	16.642	–3.160	0.020	0.137	0.690	0.156
$H, V-H$	FU	16.570	–3.406	0.023	0.142	0.288	0.127
			—LMC TIICs—				
$I, V-I$	FU	17.326	–2.496	0.014	0.018	1.550	0.101
$J, V-J$	FU	17.280	–2.307	0.031	0.038	0.406	0.202
$H, V-H$	FU	17.260	–2.470	0.042	0.052	0.217	0.237
$K, V-K$	FU	17.263	–2.433	0.017	0.021	0.134	0.107
$K, I-K$	FU	17.264	–2.448	0.017	0.021	0.250	0.114
$K, J-K$	FU	17.275	–2.523	0.020	0.024	0.690	0.129
$K, V-I$	FU	17.368	–2.375	0.016	0.020	0.288	0.101

From left to right the columns list the photometric band and the color adopted to define the Wesenheit pseudo magnitude, the mode, the zero-point, the slope of the PW relation, the uncertainties on zero-point and slope, the color index and the standard deviation (mag).

[1]To obtain the absolute zero points, one should subtract the geometrical distance modulus of the LMC and SMC, based on eclipsing binaries (18.477±0.026 mag and 18.977±0.028 mag for the LMC and SMC, respectively (Pietrzyński et al, 2019; Graczyk et al, 2020)).

Appendix C Evolutionary constraints for Cepheids

Cepheid pulsation properties are the convolution between evolutionary and pulsation properties of low- and intermediate-mass stars. Panel a) of Fig. 4 shows the comparison in the HRD between BASTI-IAC canonical scaled solar evolutionary models at solar chemical composition, covering a broad range in stellar masses and the CC instability strip (Fiorentino et al, 2002). The dashed lines display hydrogen-burning phases, while solid purple lines display helium-burning phases, and the solid cyan lines the double shell burning phases (AGB). The blue and the red almost vertical lines show the first overtone blue edge and the fundamental red edge for the same chemical composition. These boundaries bracket the region of the HRD, in which CCs are expected to be pulsationally stable. Evolutionary and pulsation predictions plotted in this panel indicate that CCs at solar iron abundance are expected to cover a broad range in pulsation period. The minimum mass crossing the Cepheid instability strip is of the order of $M = 3.0$–$3.5\,M_{\odot}$, while the most massive ones are still crossing the instability strip during helium-burning phases.

Panels b) and c) of Fig. 4 display the same predictions, but for stellar structures constructed by assuming chemical compositions that are half solar Z=0.01 and Z=0.001, respectively. A glance at the predictions plotted in these panels shows quite clearly that the minimum mass crossing the CC instability strip steadily decreases when moving into the more metal-poor regimes. This explains why the period distribution shifts toward shorter periods moving from the MW to the SMC. Moreover, evolutionary tracks plotted in the bottom panel show that a significant fraction of more massive stellar structures cross the instability strip during the AGB (cyan color). This means a decrease in the evolutionary time spent inside the instability strip, and in turn, it explains the lack of long period Cepheids in metal-poor stellar systems like IC 1613 (Pietrzyński et al, 2006) and WLM (Pietrzyński et al, 2007).

In order to investigate this issue on a more quantitative basis, Table C3 gives for four different chemical compositions the difference in luminosity and in evolutionary lifetime for the three different crossings based on evolutionary models taking into account convective core overshooting during central hydrogen burning phases.

Figure 7 shows the comparison in the HRD between BASTI-IAC canonical evolutionary models for intermediate-age stellar structures and the AC instability strip (Monelli and Fiorentino, 2022). The blue tips (the hottest point during helium burning phases) when moving from more metal-rich to more metal-poor stellar structures become systematically hotter and cross the Anomalous Cepheid instability strip (blue and red almost vertical lines). This trend is even more evident for stellar structures taking into account convective core overshooting.

Evolutionary and pulsation predictions for TIICs plotted in Fig. 10 cover two dex in metal/hydrogen abundance ratio. However, TIICs evolutionary status is minimally affected by the metal content, since they are either AGB or post AGB stars during their lifetime. This property is independent of the pulsation period, i.e. from BL Herculis to RV Tauri variables. Moreover, the current evidence supports their presence both in metal-poor and in metal-rich stellar systems. The key point is the presence of hot and extreme HB stars, i.e. the low mass-tail of HB stars.

Table C3 Mean luminosity and evolutionary lifetime for the three different crossings of intermediate-mass evolutionary models constructed by taking into account convective core overshooting during central hydrogen burning phases.

$M/M_\odot$	$\langle\log(L/L_\odot)\rangle^a$	t(Kyr)	$\langle\log(L/L_\odot)\rangle^a$	t(Kyr)	$\langle\log(L/L_\odot)\rangle^a$	t(Kyr)
	1st crossing		2nd crossing		3rd crossing	
			[Fe/H]=+0.06			
2.8	2.099	251.81	…	…	…	…
3.0	2.205	170.61	…	…	…	…
3.5	2.436	73.56	…	…	…	…
4.0	2.636	39.95	…	…	…	…
4.5	2.812	23.00	…	…	…	…
5.0	2.970	14.50	3.163	2880.21[b]	…	…
6.0	3.242	7.00	3.459	138.81	3.501	191.63
7.0	3.472	4.00	3.704	53.40	3.739	59.52
8.0	3.649	2.50	3.922	16.96	3.933	27.52
9.0	3.818	1.56	4.109	9.45	4.098	15.28
10.0	3.937	1.20	…	…	…	…
11.0	3.998	0.79	4.402	5.22	4.339	6.46
12.0	4.109	0.70	4.490	5.22	4.443	5.40
13.0	4.303	1.12	…	…	…	…
14.0	4.622	9.09	…	…	…	…
			[Fe/H]=-0.30			
2.8	2.210	159.59	…	…	…	…
3.0	2.324	111.45	…	…	…	…
3.5	2.539	52.57	…	…	…	…
4.0	2.736	29.07	2.907	45.04	2.982	2225.45
4.5	2.910	17.79	3.113	364.28	3.179	365.68
5.0	3.068	11.90	3.289	307.13	3.348	192.83
6.0	3.340	6.09	3.570	140.94	3.612	36.92
7.0	3.565	3.70	3.807	41.16	3.821	16.35
8.0	3.749	2.58	4.009	17.75	3.998	10.73
9.0	3.896	1.90	4.157	12.57	4.103	5.28
10.0	3.991	1.29	4.314	12.29	4.273	9.08
11.0	4.099	1.16	4.406	9.48	4.291	2.25
12.0	4.239	1.31	4.498	10.30	4.380	2.24
13.0	4.421	2.23	4.610	15.56	4.601	11.20
			[Fe/H]=-0.60			
2.8	2.296	114.17	…	…	…	…
3.0	2.397	82.87	…	…	…	…
3.5	2.623	41.54	2.814	737.93	2.898	933.95
4.0	2.819	23.61	3.035	645.04	3.101	248.89
4.5	2.992	15.17	3.232	682.77	3.273	186.44
5.0	3.148	10.35	3.403	551.16	3.428	176.14
6.0	3.417	5.70	3.659	232.49	3.694	99.88
7.0	3.628	4.00	3.882	55.88	3.912	55.91
8.0	3.807	3.00	4.070	25.61	4.085	33.60
9.0	3.944	1.95	4.221	19.35	4.216	17.50
10.0	4.066	1.38	4.334	16.28	4.300	6.24
11.0	4.197	1.66	4.435	19.41	4.396	5.24
12.0	4.378	2.64	4.556	36.83	4.591	15.55
13.0	4.724	105.75	…	…	…	…
			[Fe/H]=-0.90			
2.6	2.262	129.10	…	…	…	…
2.8	2.371	91.97	2.615	3449.14	2.646	4483.62
3.0	2.472	66.21	2.737	6159.92[b]	…	…
3.5	2.698	35.14	2.964	5414.59[b]	…	…
4.0	2.893	20.54	3.132	1129.51	3.186	315.84
4.5	3.066	13.50	3.291	595.31	3,359	134.27
5.0	3.221	9.50	3.435	370.46	3.509	66.84
6.0	3.481	6.00	3.686	107.64	3.754	24.09
7.0	3.692	3.71	3.904	31.16	3.947	13.18
8.0	3.868	2.71	4.087	22.71	4.106	9.37
9.0	4.013	2.41	4.237	25.18	4.212	4.92
10.0	4.148	2.32	4.358	34.52	4.341	4.40
11.0	4.317	3.14	4.474	74.24	4.534	10.85
12.0	4.652	28.52	…	…	…	…
13.0	4.738	18.84	…	…	…	…

[a] The mean luminosity was estimated as the mean along the crossing (see text for more details). [b] The blue loop is entirely located inside the instability strip.

C.1 Helium burning lifetimes

The top left panels of Fig. C11 display three key parameters for investigating central helium burning phases of both low- and intermediate-mass stellar structures at solar metal content. The solid lines plotted in panel a) show the helium-core mass (solar units) as a function of the stellar mass just before the onset of central helium burning. The helium-core mass is, as expected, almost constant ($M_{\rm CHe}/M_{\odot} \sim 0.5$) for stellar masses ranging from 1 to 1.6 $M_{\odot}$, attains a well-defined minimum ($M_{\rm CHe}/M_{\odot} \sim 0.32$) for $M \sim 1.8\,M_{\odot}$ and then steadily increases. This minimum marks the transition between low-mass stellar structures that ignite helium in electron-degenerate core through a core-helium flash and intermediate-mass stars that ignite helium quiescently. Hydrogen burning for stellar structures at solar iron abundance and more massive than 1.6 $M_{\odot}$ is almost entirely driven by the CNO cycle. The strong dependence of the CNO cycle on the temperature causes an increase in the core temperature gradient, and in turn, the transition into the convective regime. The onset of convective cores causes the steady increase in the helium core mass soon after the minimum. This transition has been defined by Sweigart et al (1989) as the *RGB transition*. Solid and dashed line display predictions for evolutionary models constructed either taking account of or neglecting convective core overshooting. Canonical models display, as expected, the same transition, but at larger stellar masses ($M \sim 2.2\,M_{\odot}$).

Panel b) shows the logarithmic luminosity (solar units) at the onset of central helium burning as a function of the stellar mass. Predictions plotted in this panel display a well known result. The luminosity of evolutionary models taking account for the convective core overshooting is, at fixed stellar mass, systematically brighter than canonical models. Indeed, the former models have, at fixed stellar mass, larger helium-core masses.

Panel c) shows the logarithm of the ratio between central hydrogen and helium burning time. Predictions indicate that this ratio decreases by 1.5 dex when moving from the low- to the intermediate-mass regime. This decrease is caused by the fact that, across the transition, the luminosity of central helium-burning structures decreases and the central helium-burning lifetime increases by more than a factor of three. Indeed, the central helium-burning time (solid blue line) increases from ≈100 Myr to almost ≈300 Myr. The main consequence of this increase is that central hydrogen burning lifetime across the transition is only a factor of four longer than central helium-burning lifetime. The hydrogen burning lifetime is two order of magnitude longer in the low-mass regime, and roughly one order of magnitude longer in the intermediate-mass regime. The stellar structures at the transition between low- and intermediate-mass stellar structures are strong contributors of central helium-burning stellar populations (red clump, Girardi, 2016). Predictions based on canonical evolutionary models display the same trend. The main difference being that central hydrogen burning lifetime is, at the transition, only a factor of two longer than central helium lifetime. Thus further increases the fraction of red clump stars compared with main-sequence stars.

Evolutionary predictions plotted in panels d), e), and f) and in the bottom panels of Fig. C11 display the same predictions, but for more metal-poor chemical compositions (see labelled values). The decrease in the metal content causes, as

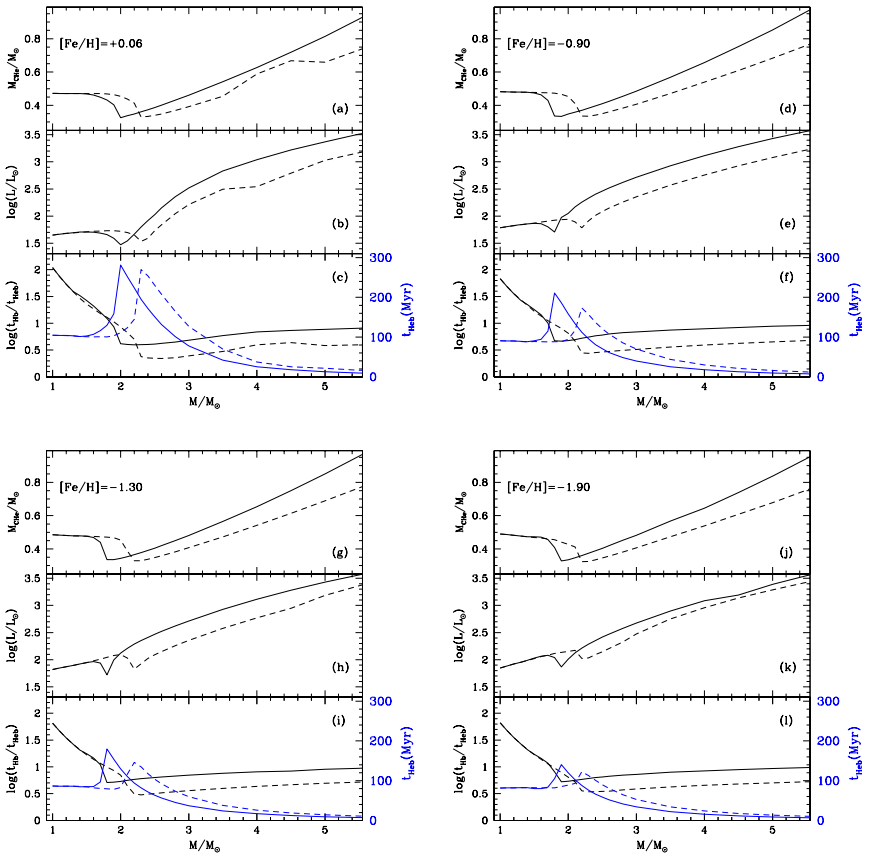

Fig. C11 Top left: Panel a)– Core helium mass (solar units) just before central helium burning phases as a function of the stellar mass (solar units) at solar metal content. The solid lines display predictions based on evolutionary models taking account of convective core overshooting, while the dashed lines on evolutionary models that neglect convective core overshooting. Panel b)– Logarithmic luminosity (solar units) at the onset of central helium-burning phases as a function of the stellar mass (solar units). Panel c)– Logarithmic ratio between central hydrogen and central helium-burning evolutionary times (black line). The blue line shows the central helium-burning evolutionary time, the scale is showed on the right side of the panel. Top right: Panels d,e,f) same as the top left, but for a more metal-poor chemical composition [Fe/H] = −0.90. Bottom left: Panels g,h,i) same as the top left, but for a more metal-poor chemical composition [Fe/H] = −1.30. Bottom right: Panels j,k,l) same as the top left, but for a more metal-poor chemical composition [Fe/H] = −1.60.

expected, a mild decrease in the stellar mass at which the transition between low- and intermediate-mass stars takes place. Indeed, it decreases from $M \sim 2.3\,M_{\odot}$ at solar iron abundance to $M \sim 2.2\,M_{\odot}$ at [Fe/H]= −1.90. The decrease is caused by the fact that more metal-poor stellar structure are, at fixed stellar mass, brighter and hotter than more metal-rich stellar structures. Therefore, the former stellar structures ignite quiescently helium at lower stellar masses (Castellani and degl'Innocenti, 1995).

Evolutionary models constructed by taking into account convective core overshooting during central hydrogen burning show a similar trend. The difference is also discussed in section C.2; here we simply mention that the transition decreases from $M \sim 2.0\,M_{\odot}$ to $M \sim 1.90\,M_{\odot}$ when moving from solar iron abundance to [Fe/H]= −1.90.

C.2 On the mass luminosity relation of ACs

Evolutionary predictions plotted in Fig. C12 display the mass–luminosity relations in a log-log plane for stellar structures during central helium-burning phases. Intermediate-mass stars perform the so-called blue loop, during which they cross the Cepheid instability strip. The luminosity for these stellar structures was estimated at the center of the instability strip ($\log T_{\rm eff} = 3.85$), as the mean between the blueward and the red-ward excursion. Stellar structures in which the helium ignition in the core takes place in partially electron degenerate conditions (low-mass regime) do not become hot enough to cross the Cepheid instability strip. The luminosity for these stellar structures was defined as the mean luminosity between the luminosity at the helium ignition and central helium exhaustion. The black crosses show the transition ($M/M_{\odot}$=2.3–2.2) between stellar structures experiencing a mild core-helium flash and stellar structures that ignite helium quiescently. In order to provide a more quantitative estimate of the transition between low and intermediate-mass stars, we also performed linear fits of the two groups. We found that the ML relation for the intermediate-mass stars is:

$$\log(M/M_{\odot}) = 1.21 \pm 0.03 + 3.06(\pm 0.05) \times \log(L/L_{\odot})$$

where the symbols have their usual meaning, and the standard deviation is σ= 0.03 dex, whereas for the low-mass stars it is

$$\log(M/M_{\odot}) = 1.95 \pm 0.02 + 0.98(\pm 0.08) \times \log(L/L_{\odot})$$

with σ= 0.02 dex. The current findings are suggesting that the coefficient of the luminosity term is three times larger when moving from the low- to the intermediate-mass regime.

In order to provide a comprehensive analysis of the transition between low- and intermediate-mass stars we performed the same calculations, but for evolutionary models constructed by assuming a mild convective core overshooting during central hydrogen-burning phases. Predictions plotted in the right panel of Fig. C12 clearly show that models taking account of core overshooting are at a fixed stellar mass, as expected, systematically brighter than canonical models. Moreover, the transition between low- and intermediate mass stars takes place at lower stellar masses when compared with canonical models, typically between $M/M_{\odot}$=2.0 and 1.9. The difference is due to the fact that evolutionary models taking into account core overshooting have, at a fixed stellar mass, larger core helium masses, and in turn hotter central temperatures. Therefore, they are less affected by electron degeneracy. We

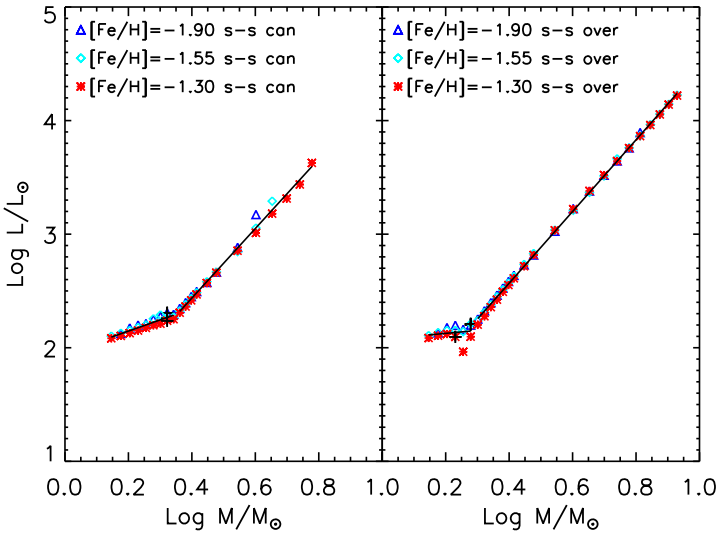

Fig. C12 Left: Logarithmic stellar mass versus logarithmic luminosity. Different symbols display canonical evolutionary models constructed by assuming different scaled-solar chemical compositions (see labelled values). The black crosses mark the transition between stellar structures, in which core helium burning is partially affected by electron degeneracy (less massive), and those with a quiescent ignition of core-helium burning (more massive). The dashed and the solid black lines show the linear fit for the two different groups. Right: Same as the left, but for evolutionary models constructed by assuming a mild convective core overshooting during central hydrogen burning phases.

also performed the linear fits to the two different regimes and we found:

$$\log(M/M_{\odot}) = 1.31 \pm 0.01 + 3.16(\pm 0.01) \times \log(L/L_{\odot})$$

with σ= 0.02 dex (intermediate-mass)

$$\log(M/M_{\odot}) = 2.08 \pm 0.07 + 0.25(\pm 0.33) \times \log(L/L_{\odot})$$

with σ= 0.06 dex (low-mass). The difference between low- and intermediate-mass regime is smaller than for canonical models, but the variation is still at 50% level. This suggests, once again, a relevant change between faint and bright ACs.

This direct evidence, together with the circumstantial evidence brought forward in Sect. 5 discloses a more complex evolutionary framework for ACs. Indeed, the current findings are suggesting, as originally found by Caputo et al (2004) and Fiorentino et al (2014), that ACs are a mix of stellar structures that are either partially affected by electron degeneracy or stellar structures that quiescently ignite helium. The latter group is from the evolutionary point of view identical to classical Cepheids. This means that more massive ACs are indeed, nothing else but the more metal-poor tail of classical Cepheids (Caputo et al, 2004). Therefore, the truly ACs appear to be the less massive ACs. This plain evidence also explains why the PL relations for ACs explicitly include a term for the stellar mass. The ACs identified in dwarf galaxies are

a mix of objects which are either minimally or partially affected by electron degeneracy. This means that they are fundamental laboratories to constrain the impact of electron degeneracy on the pulsation properties of ACs.

C.3 First dredge up

The transition between low- and intermediate-mass stars brings forward several interesting properties concerning the mixing and the variation of surface abundances. Panel a) of Fig. C13 shows a set of evolutionary model at solar iron abundance and stellar masses ranging from 2.3 to 13 $M_{\odot}$. The red circles plotted along the individual tracks mark the central helium ignition. This key evolutionary phase moves from

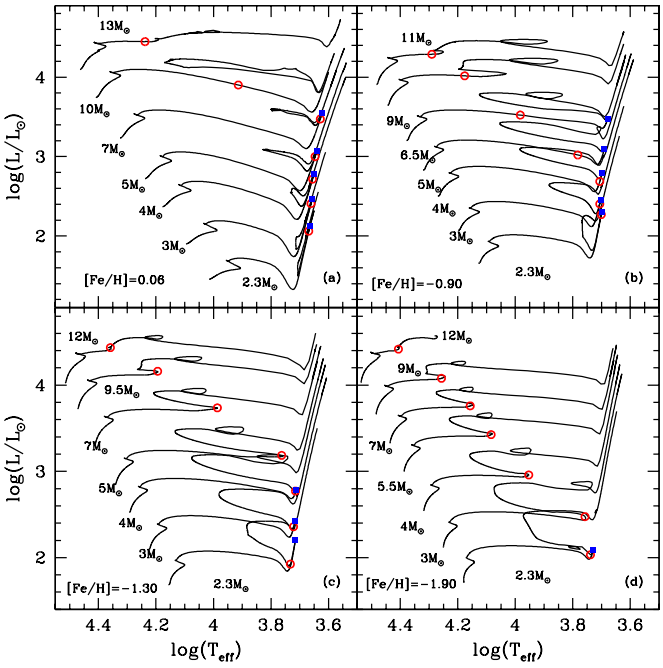

Fig. C13 Panel a): Hertzsprung–Russell Diagram for young stellar structures neglecting convective overshooting during core hydrogen-burning phase with a scaled solar chemical mixture and solar iron abundance. The stellar masses range from 2.8 to 13 $M_{\odot}$. The blue squares mark the position of the I dredge up, whereas the red circles the ignition of the 3α reactions (core He burning). Panel b): Same as the left, but for a more metal-poor ([Fe/H]= −0.90) chemical composition. Bottom: Same as the top, but for two more metal-poor chemical compositions: [Fe/H]= −1.30 (panel c) and [Fe/H]= −1.90 (panel d).

the tip of the red giant branch (TRGB) in the low- and in the intermediate-mass regime to earlier and earlier phases in the massive stellar regime. The helium ignition for $M \sim 10\,M_{\odot}$ takes place in the so-called Hertzsprung gap, well before the stellar structure approached the TRGB, and soon after central hydrogen exhaustion for

$M \sim 13\,M_{\odot}$. The latter stellar structure does not perform the blue loop, therefore, its contribution to classical Cepheids becomes either minimal or vanishing.

The blue squares plotted along the same tracks mark the phases in which the I dredge up (IDUP) takes place. This is a well-known mixing phenomenon, stellar structures moving towards their Hayashi track become systematically cooler. The increase in the envelope opacity causes the convective envelope to become thicker and thicker. During subsequent evolutionary phases the hydrogen shell moves outwards (the helium-core mass increases) and the bottom of the convective envelope recedes. In this specific phase, the IDUP occurs, during which nuclear processed material (central hydrogen burning phases) is dredged-up into the surface regions. Predictions plotted in this panel show that stellar structures in which central-helium ignition takes place before the stellar structures approach their Hayashi track either do not experience or experience a very mild IDUP.

Evolutionary tracks plotted in panel b) and in the panels c), d) display similar predictions, but for more metal-poor stellar structures (see labelled values). The main consequence of the decrease in metal content is that central helium ignition in more metal-poor stellar structures takes place before the approach to the Hayashi tracks at lower stellar masses, indeed it ranges from $M = 6.5\,M_{\odot}$ for [Fe/H]= −0.90 to $M = 2.3\,M_{\odot}$ at [Fe/]= −1.90. This means that only a minor fraction, if any, of intermediate mass stars in the metal-poor regime experience the IDUP. This change has implications not only for the surface chemical abundances, but also on the evolutionary lifetime spent inside the instability strip.

The key evolutionary parameters at central He-burning ignition and at the IDUP for canonical and convective core overshooting evolutionary models are listed in Table C4 and in Table C5 available in this Appendix.

To further constrain the abundance patterns of different groups of variable stars, we decided to analyze the impact of the I dredge up on their surface abundance. Figure C14 shows the fractional variation in the abundances of the elements affected by the I dredge up. The top panels display the relative difference between the surface chemical composition at the I dredge up and the surface chemical composition on the main sequence for He (panel a), C (panel b), N (panel c) and O (panel d) normalized to the abundance on the main sequence. These panels only includes stellar structures which undergo the I dredge up and lines of different colors show predictions for different chemical compositions. The bottom panels of Fig. C14 display the predicted fractional variation in the abundance of He (panel e), C (panel f), N (panel g) and O (panel h), but for more metal-poor chemical compositions.

Panel a) of Fig. C14 shows that the impact on the He abundance in the metal-rich regime is, as expected, modest and typically smaller than 10% with a local minimum for stellar masses of 1.5–2.0 $M_{\odot}$. The variation in helium abundance is vanishing for stellar masses larger than $\sim 2.5\,M_{\odot}$ over the entire metallicity range. The impact is also minimal in the metal-poor regime. Indeed, canonical (dashed lines) and non-canonical (solid lines) stellar structures display variations of the order of a few percents.

The variation concerning the C abundance is more complex. Indeed, the surface C abundance steadily decreases in more metal-rich stellar structures (left panels) that

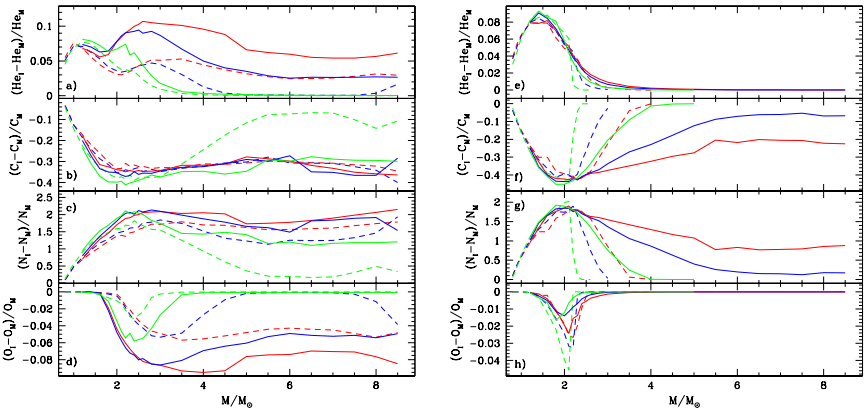

Fig. C14 Top: Relative difference between the surface chemical composition at the I dredge up and the surface chemical composition on the main sequence for He (panel a), C (panel b), N (panel c) and O (panel d) normalized to the abundance on the main sequence. The iron abundance of the different evolutionary models is color-coded and changes from solar iron abundance ([Fe/H]=0.06, red) to half-solar ([Fe/H]= −0.30, blue) and to Z=0.001 ([Fe/H]= −0.90, green). Dashed lines display predictions based on evolutionary models neglecting convective core overshooting, while the solid ones are based on models taking into account convective core overshooting during central hydrogen-burning phases. Note that only evolutionary models that underwent the I dredge up have been plotted. Bottom: Same as the top panels, but for the three more metal-poor chemical compositions: [Fe/H]= −1.30, red; [Fe/H]= −1.55, blue; [Fe/H]= −1.90, green.

undergo a core helium flash. The variation in C (panel b) ranges from a few percent for old ($M/M_{\odot}$ = 0.8) stellar structures to 30%–40% for stellar structures at the transition between low- and intermediate-mass ($M/M_{\odot}$=2.0–2.2) regime. The metallicity has a minimal impact, since they remain under-abundant over the entire range in stellar mass. More metal-poor stellar structures (panel f) display a steady increase soon after the maximum, thus suggesting that these structures experience a very mild IDUP. The difference is mainly caused by the fact that metal-poor stellar structures are systematically brighter and hotter than metal-rich ones. This means that along the RGB, convective transport is less efficient and the bottom of the convective envelope is not deep enough to approach the regions in which the CNO cycle has been efficient. The difference between canonical (dashed lines) and non-canonical (solid) is minimal with the former ones experiencing the IDUP in a very limited range in mass.

The variation of the surface N abundance is, as expected for the CN cycle, the mirror image of the C abundance. The N abundance (panel c) steadily increases by more than a factor of two when moving from old ($M/M_{\odot}$ = 0.8) to intermediate-age ($M/M_{\odot}$=2.0–2.2) stellar structures. The current predictions indicate that more metal-rich (solar, half solar) stellar structures are overabundant in N over the entire mass range. On the other hand, metal-intermediate and metal-poor stellar structures (panel g) are less affected by the IDUP for stellar masses larger than 4 $M_{\odot}$. Canonical evolutionary models indicate that only stellar structures less massive than 4 $M_{\odot}$ experience the IDUP.

The variation of the surface O abundance for metal-rich (panel d) stellar structures is similar to C, but there are some key differences. In the low-mass regime ($M/M_{\odot} \leq 1.5$) O abundance is not affected by the IDUP. This trend is expected because in these structures the NO cycle has a very low efficiency. The variation becomes more relevant and approaches 5%–6% for stellar structures with masses ranging from 2 to 4 $M_{\odot}$. The trend in the metal-poor regime (panel h) is the mirror image of He abundance, indeed, for stellar masses of 1.8–2.5 $M_{\odot}$ decreases by roughly 3%–4%, while it is vanishing for more massive stellar structures.

The difference between metal-rich and metal-poor stellar structures is twofold: the metal-poor ones are brighter and hotter; this means that with a fixed stellar mass the central temperature is higher and the NO cycle becomes more efficient. The convective envelopes are less extended, since convection is less efficient along the RGB, but they deepen enough to dredge up material processed by both CN and NO cycles.

The current predictions concerning the efficiency of the IDUP as a function of stellar mass and chemical composition bring forward two key features worth being discussed in more detail.

a) Stellar structures at the transition between low- and intermediate-mass stars after the IDUP are predicted to show an enhancement in N abundance that is two times the abundance on the main sequence. The decrease in C abundance for the same stellar structures is 30%–40% when compared with the MS abundance. Note that this metallicity range does not produce ACs, since their helium-burning locus is systematically cooler (redder) than the instability strip.

b) The current predictions indicate that Galactic CCs should show larger abundance variations due to the IDUP when compared with LMC CCs, and in particular, with SMC CCs. In this context, it is worth mentioning that canonical evolutionary models for intermediate-mass stars in the metal-poor regime do not experience any IDUP. Therefore, CCs in very metal-poor stellar systems (IC 1613, SagDig, NGC 6822) should show N and C surface abundances similar to their main sequence progenitors.

Table C4 Evolutionary parameters at central He-burning ignition and at I dredge-up (IDUP) from BaSTI2 scaled solar (Caffau et al, 2011) canonical evolutionary models.

	He burning			IDUP		
$M/M_\odot$	log t	log $L/L_\odot$	log $T_{\rm eff}$	log t	log $L/L_\odot$	log $T_{\rm eff}$
			[Fe/H]=+0.06, Y=0.2695			
2.5	8.726	2.353	3.653	2.268	3.659	8.724
2.6	8.676	2.342	3.656	2.347	3.656	8.676
2.8	8.587	2.365	3.659	2.400	3.657	8.587
3.0	8.505	2.409	3.661	2.436	3.659	8.506
3.5	8.328	2.562	3.659	2.534	3.661	8.330
4.0	8.177	2.716	3.655	2.621	3.663	8.177
4.5	8.048	2.863	3.651	2.691	3.666	8.047
5.0	7.931	3.000	3.646	3.064	3.641	7.931
5.5	7.833	3.129	3.642	3.194	3.636	7.833
6.0	7.745	3.249	3.637	3.320	3.631	7.745
6.5	7.667	3.364	3.633	3.437	3.626	7.668
7.0	7.598	3.473	3.628	3.549	3.621	7.598
7.5	7.536	3.568	3.625	3.655	3.617	7.536
8.0	7.479	3.601	3.627	3.755	3.612	7.480
8.5	7.428	3.493	3.642	3.848	3.608	7.429
9.0	7.381	3.449	3.665	3.937	3.604	7.382
9.5	7.338	3.702	3.767	4.011	3.601	7.339
10.0	7.299	3.900	3.913	4.057	3.600	7.300
11.0	7.229	4.139	4.091	4.070	3.605	7.230
12.0	7.189	4.324	4.210	4.328	3.596	7.257
13.0	7.147	4.447	4.238	4.537	3.577	7.216
14.0	7.140	4.558	4.279	4.715	3.564	7.197
			[Fe/H]=–0.30, Y=0.2571			
2.5	8.647	2.330	3.676	2.358	3.674	8.648
2.6	8.602	2.332	3.678	2.370	3.676	8.602
2.8	8.517	2.367	3.680	2.412	3.677	8.518
3.0	8.440	2.419	3.681	2.468	3.678	8.440
3.5	8.271	2.579	3.679	2.632	3.675	8.271
4.0	8.130	2.731	3.676	2.735	3.676	8.130
4.5	8.008	2.880	3.671	2.826	3.676	8.008
5.0	7.903	3.017	3.668	3.078	3.663	7.902
5.5	7.806	3.133	3.665	3.211	3.658	7.806
6.0	7.724	3.193	3.666	3.338	3.653	7.725
6.5	7.651	3.139	3.681	3.456	3.648	7.652
7.0	7.586	3.236	3.698	3.570	3.644	7.587
7.5	7.528	3.431	3.729	3.673	3.639	7.528
8.0	7.475	3.592	3.801	3.773	3.633	7.476
8.5	7.427	3.728	3.879	3.862	3.631	7.427
9.0	7.383	3.850	3.950	3.940	3.628	7.383
9.5	7.343	3.981	4.040	3.974	3.629	7.343
10.0	7.306	4.068	4.104	3.976	3.633	7.307
11.0	7.239	4.243	4.208	4.364	3.608	7.307
12.0	7.200	4.362	4.268	4.445	3.607	7.266

continued on next page

Table C4 continued.

		He burning			IDUP	
$M/M_\odot$	log t	log $L/L_\odot$	log $T_{\rm eff}$	log t	log $L/L_\odot$	log $T_{\rm eff}$
		[Fe/H]=–0.60, Y=0.2521				
2.5	8.598	2.296	3.692	2.341	3.690	8.599
2.6	8.554	2.309	3.694	2.330	3.693	8.554
2.8	8.472	2.355	3.695	2.404	3.692	8.473
3.0	8.398	2.418	3.695	2.466	3.692	8.398
3.5	8.236	2.581	3.693	2.633	3.689	8.236
4.0	8.099	2.737	3.690	2.795	3.686	8.100
4.5	7.982	2.878	3.687	2.944	3.682	7.983
5.0	7.880	2.917	3.692	3.057	3.681	7.885
5.5	7.788	2.960	3.714	3.225	3.673	7.789
6.0	7.709	3.196	3.756	3.351	3.668	7.710
6.5	7.640	3.381	3.837	3.468	3.664	7.640
7.0	7.577	3.530	3.894	3.582	3.660	7.578
7.5	7.521	3.656	3.939	3.688	3.656	7.522
8.0	7.470	3.764	3.986	3.782	3.652	7.470
8.5	7.423	3.866	4.031	3.866	3.648	7.424
9.0	7.381	3.964	4.088	3.913	3.648	7.382
9.5	7.342	4.056	4.149	4.183	3.634	7.409
10.0	7.306	4.130	4.186	4.256	3.631	7.373
		[Fe/H]=–0.90, Y=0.2496				
2.5	8.564	2.255	3.706	2.302	3.703	8.565
2.6	8.521	2.277	3.706	2.326	3.704	8.522
2.8	8.442	2.336	3.707	2.386	3.704	8.442
3.0	8.369	2.404	3.706	2.454	3.703	8.370
3.5	8.212	2.574	3.705	2.627	3.701	8.212
4.0	8.079	2.686	3.706	2.795	3.698	8.079
4.5	7.964	2.747	3.726	2.944	3.694	7.965
5.0	7.866	3.020	3.783	3.096	3.690	7.867
5.5	7.776	3.227	3.880	3.231	3.686	7.777
6.0	7.700	3.387	3.939	3.358	3.682	7.701
6.5	7.632	3.523	3.983	3.477	3.678	7.633
7.0	7.571	3.643	4.021	3.587	3.675	7.572
7.5	7.516	3.750	4.051	3.691	3.671	7.518
8.0	7.467	3.843	4.081	3.784	3.667	7.468
8.5	7.421	3.929	4.120	3.848	3.666	7.423
9.0	7.379	4.016	4.176	4.289	3.635	7.447
9.5	7.341	4.095	4.206	4.375	3.631	7.407

Table C5 Evolutionary parameters at central He-burning ignition and at I dredge-up (IDUP) from BaSTI2 scaled-solar (Caffau et al, 2011) evolutionary models taking into account of convective core overshooting during central hydrogen burning phases.

		He burning			IDUP	
$M/M_\odot$	log t	log $L/L_\odot$	log $T_{\rm eff}$	log t	log $L/L_\odot$	log $T_{\rm eff}$
		[Fe/H]=+0.06, Y=0.2695				
2.5	8.796	2.501	3.645	2.538	3.642	8.797
2.6	8.749	2.523	3.645	2.567	3.642	8.749
2.8	8.660	2.590	3.645	2.635	3.641	8.660
3.0	8.578	2.661	3.644	2.712	3.640	8.579
3.5	8.400	2.840	3.639	2.894	3.635	8.400
4.0	8.249	3.013	3.634	3.071	3.629	8.250
4.5	8.120	3.173	3.628	3.231	3.622	8.121
5.0	8.004	3.312	3.622	3.380	3.616	8.004
5.5	7.905	3.449	3.617	3.523	3.610	7.906
6.0	7.818	3.576	3.612	3.649	3.604	7.818
6.5	7.740	3.692	3.607	3.765	3.599	7.741
7.0	7.670	3.798	3.602	3.872	3.595	7.671
7.5	7.607	3.896	3.598	3.972	3.590	7.608
8.0	7.550	3.987	3.594	4.064	3.586	7.551
8.5	7.498	4.069	3.591	4.150	3.583	7.499
9.0	7.451	4.153	3.587	4.229	3.579	7.451
9.5	7.407	4.236	3.583	4.303	3.576	7.408
10.0	7.367	4.312	3.580	4.372	3.574	7.367
11.0	7.295	3.893	3.640	4.496	3.569	7.295
12.0	7.234	4.329	3.942	4.583	3.568	7.234
13.0	7.181	4.513	4.081	4.556	3.578	7.181
14.0	7.135	4.653	4.173	4.787	3.561	7.177
		[Fe/H]=–0.30, Y=0.2571				
2.5	8.718	2.520	3.665	2.460	3.670	8.718
2.6	8.674	2.553	3.665	2.481	3.671	8.673
2.8	8.589	2.621	3.665	2.540	3.671	8.589
3.0	8.512	2.693	3.663	2.584	3.672	8.512
3.5	8.344	2.877	3.659	2.685	3.674	8.344
4.0	8.203	3.046	3.654	2.770	3.678	8.202
4.5	8.081	3.206	3.648	2.878	3.680	8.081
5.0	7.976	3.351	3.643	3.302	3.647	7.976
5.5	7.879	3.477	3.639	3.548	3.632	7.880
6.0	7.798	3.601	3.634	3.675	3.627	7.798
6.5	7.725	3.716	3.629	3.788	3.622	7.725
7.0	7.659	3.817	3.625	3.893	3.618	7.659
7.5	7.600	3.912	3.621	3.992	3.614	7.600
8.0	7.546	3.978	3.620	4.082	3.610	7.546
8.5	7.497	4.082	3.615	4.168	3.607	7.498
9.0	7.452	4.128	3.615	4.246	3.604	7.452
9.5	7.410	3.949	3.638	4.317	3.601	7.411
10.0	7.373	4.060	3.757	4.385	3.599	7.373
11.0	7.304	4.281	3.954	4.496	3.595	7.304
12.0	7.244	4.436	4.088	4.553	3.596	7.245
13.0	7.192	4.552	4.175	4.579	3.601	7.192
14.0	7.145	4.680	4.255	4.813	3.586	7.185

continued on next page

Table C5 continued.

		He burning			IDUP	
$M/M_{\odot}$	log t	log $L/L_{\odot}$	log $T_{\rm eff}$	log t	log $L/L_{\odot}$	log $T_{\rm eff}$
		[Fe/H]=–0.60, Y=0.2521				
2.5	8.670	2.527	3.680	2.573	3.677	8.670
2.6	8.626	2.562	3.679	2.610	3.676	8.627
2.8	8.545	2.636	3.679	2.685	3.675	8.546
3.0	8.471	2.713	3.677	2.718	3.677	8.471
3.5	8.309	2.895	3.673	2.824	3.678	8.308
4.0	8.173	3.066	3.668	2.931	3.680	8.172
4.5	8.056	3.223	3.663	3.244	3.662	8.056
5.0	7.954	3.369	3.658	3.426	3.654	7.955
5.5	7.862	3.493	3.655	3.565	3.649	7.862
6.0	7.783	3.614	3.650	3.687	3.644	7.784
6.5	7.713	3.720	3.647	3.801	3.640	7.714
7.0	7.650	3.759	3.649	3.905	3.635	7.650
7.5	7.593	3.670	3.666	4.002	3.632	7.593
8.0	7.541	3.733	3.681	4.091	3.628	7.541
8.5	7.493	3.896	3.722	4.174	3.625	7.493
9.0	7.450	4.019	3.797	4.252	3.622	7.450
9.5	7.409	4.122	3.878	4.323	3.620	7.410
10.0	7.372	4.209	3.954	4.386	3.618	7.373
		[Fe/H]=–0.90, Y=0.2496				
2.5	8.636	2.527	3.692	2.571	3.689	8.637
2.6	8.594	2.563	3.692	2.611	3.689	8.594
2.8	8.515	2.638	3.691	2.688	3.688	8.515
3.0	8.443	2.719	3.689	2.766	3.686	8.443
3.5	8.285	2.902	3.685	2.955	3.682	8.285
4.0	8.152	3.075	3.681	3.126	3.677	8.153
4.5	8.038	3.230	3.677	3.262	3.675	8.042
5.0	7.940	3.373	3.673	3.404	3.670	7.940
5.5	7.850	3.482	3.671	3.569	3.663	7.851
6.0	7.774	3.482	3.678	3.690	3.659	7.774
6.5	7.705	3.515	3.693	3.803	3.655	7.706
7.0	7.644	3.683	3.717	3.907	3.651	7.644
7.5	7.588	3.831	3.798	4.003	3.648	7.588
8.0	7.537	3.943	3.865	4.090	3.645	7.537
8.5	7.490	4.038	3.918	4.175	3.642	7.491
9.0	7.447	4.124	3.965	4.252	3.640	7.448
9.5	7.408	4.199	4.013	4.322	3.637	7.408

References

Alcock C, Allsman RA, Alves DR, et al (1999) The MACHO Project LMC Variable Star Inventory. VIII. The Recent Star Formation History of the Large Magellanic Cloud from the Cepheid Period Distribution. AJ 117(2):920–926. https://doi.org/10.1086/300736, https://arxiv.org/abs/astro-ph/9811240 [astro-ph]

Anderson J (2002) Main-Sequence Observations with HST. In: van Leeuwen F, Hughes JD, Piotto G (eds) Omega Centauri, A Unique Window into Astrophysics, p 87

Anderson RI, Ekström S, Georgy C, et al (2014) On the effect of rotation on populations of classical Cepheids. I. Predictions at solar metallicity. A&A 564:A100. https://doi.org/10.1051/0004-6361/201322988, https://arxiv.org/abs/1403.0809 [astro-ph.SR]

Anderson RI, Saio H, Ekström S, et al (2016) On the effect of rotation on populations of classical Cepheids. II. Pulsation analysis for metallicities 0.014, 0.006, and 0.002. A&A 591:A8. https://doi.org/10.1051/0004-6361/201528031, https://arxiv.org/abs/1604.05691 [astro-ph.SR]

Andreasen GK (1988) Precise Fourier decomposition parameters for classical Cepheids. A&A 196:159–172

Andreasen GK, Petersen JO (1987) Cepheids in the Magellanic clouds. I. Fourier decomposition of LMC Cepheid light curves. A&A 180:129–144

Andrievsky SM, Luck RE, Kovtyukh VV (2005) Phase-dependent Variation of the Fundamental Parameters of Cepheids. III. Periods between 3 and 6 Days. AJ 130(4):1880–1889. https://doi.org/10.1086/444541

Andrievsky SM, Lépine JRD, Korotin SA, et al (2013) Barium abundances in Cepheids. MNRAS 428(4):3252–3261. https://doi.org/10.1093/mnras/sts270, https://arxiv.org/abs/1210.6211 [astro-ph.GA]

Andrievsky SM, Luck RE, Korotin SA (2014) Barium in Cepheids: new data on the abundance distribution in the Galactic disc. MNRAS 437(3):2106–2110. https://doi.org/10.1093/mnras/stt1992

Aparicio A, Gallart C (2004) IAC-STAR: A Code for Synthetic Color-Magnitude Diagram Computation. AJ 128:1465–1477. https://doi.org/10.1086/382836, https://arxiv.org/abs/astro-ph/0407589

Arnett WD (1979) On the theory of type I supernovae. ApJ 230:L37–L40. https://doi.org/10.1086/182957

Baade W (1956) The Period-Luminosity Relation of the Cepheids. PASP 68:5. https:

//doi.org/10.1086/126870

Bailer-Jones CAL, Rybizki J, Fouesneau M, et al (2021) Estimating Distances from Parallaxes. V. Geometric and Photogeometric Distances to 1.47 Billion Stars in Gaia Early Data Release 3. AJ 161(3):147. https://doi.org/10.3847/1538-3881/abd806, https://arxiv.org/abs/2012.05220 [astro-ph.SR]

Barmby P, Marengo M, Evans NR, et al (2011) Galactic Cepheids with Spitzer. II. Search for Extended Infrared Emission. AJ 141(2):42. https://doi.org/10.1088/0004-6256/141/2/42, https://arxiv.org/abs/1011.3386 [astro-ph.SR]

Beaton RL, Bono G, Braga VF, et al (2018) Old-Aged Primary Distance Indicators. Space Sci Rev 214(8):113. https://doi.org/10.1007/s11214-018-0542-1

Beaulieu JP (1998) Cepheids in the Magellanic Cloud from the EROS microlensing survey. Mem Soc Astron Italiana 69:21–30

Belmonte MT, Pickering JC, Ruffoni MP, et al (2017) Fe I Oscillator Strengths for Transitions from High-lying Odd-parity Levels. ApJ 848(2):125. https://doi.org/10.3847/1538-4357/aa8cd3, https://arxiv.org/abs/1710.07571 [astro-ph.SR]

Beltrame M, Poretti E (2002) HD 304373, the second case of 1O/2O double-mode Cepheid in the Galaxy. A&A 386:L9–L12. https://doi.org/10.1051/0004-6361:20020315, https://arxiv.org/abs/astro-ph/0203078 [astro-ph]

Bergemann M, Lind K, Collet R, et al (2012) Non-LTE line formation of Fe in late-type stars - I. Standard stars with 1D and <3D> model atmospheres. MNRAS 427(1):27–49. https://doi.org/10.1111/j.1365-2966.2012.21687.x, https://arxiv.org/abs/1207.2455 [astro-ph.SR]

Besla G, Martínez-Delgado D, van der Marel RP, et al (2016) Low Surface Brightness Imaging of the Magellanic System: Imprints of Tidal Interactions between the Clouds in the Stellar Periphery. ApJ 825(1):20. https://doi.org/10.3847/0004-637X/825/1/20, https://arxiv.org/abs/1602.04222 [astro-ph.GA]

Bhardwaj A (2020) High-precision distance measurements with classical pulsating stars. Journal of Astrophysics and Astronomy 41(1):23. https://doi.org/10.1007/s12036-020-09640-z, https://arxiv.org/abs/2006.16262 [astro-ph.SR]

Bhardwaj A (2022) RR Lyrae and Type II Cepheid Variables in Globular Clusters: Optical and Infrared Properties. Universe 8(2):122. https://doi.org/10.3390/universe8020122, https://arxiv.org/abs/2202.06982 [astro-ph.SR]

Bhardwaj A, Kanbur SM, Macri LM, et al (2016a) Large Magellanic Cloud Near-Infrared Synoptic Survey - III. A statistical study of non-linearity in the Leavitt Laws. MNRAS 457(2):1644–1665. https://doi.org/10.1093/mnras/stw040, https://arxiv.org/abs/1601.00953 [astro-ph.GA]

Bhardwaj A, Kanbur SM, Macri LM, et al (2016b) Large Magellanic Cloud Near-infrared Synoptic Survey. II. The Wesenheit Relations and Their Application to the Distance Scale. AJ 151(4):88. https://doi.org/10.3847/0004-6256/151/4/88, https://arxiv.org/abs/1510.03682 [astro-ph.GA]

Bisterzo S, Gallino R, Straniero O, et al (2011) The s-process in low-metallicity stars - II. Interpretation of high-resolution spectroscopic observations with asymptotic giant branch models. MNRAS 418(1):284–319. https://doi.org/10.1111/j.1365-2966.2011.19484.x, https://arxiv.org/abs/1108.0500 [astro-ph.SR]

Bohm-Vitense E (1988) Are Most Short-Period Cepheids Overtone Pulsators? ApJ 324:L27. https://doi.org/10.1086/185083

Bono G, Caputo F, Stellingwerf RF (1994) Oosterhoff dichotomy in the Galaxy and globular clusters in the Large Magellanic Cloud. ApJ 423:294–304. https://doi.org/10.1086/173806

Bono G, Caputo F, Castellani V, et al (1997) Nonlinear investigation of the pulsational properties of RR Lyrae variables. A&AS 121:327–342. https://doi.org/10.1051/aas:1997289, https://arxiv.org/abs/astro-ph/9606030

Bono G, Caputo F, Castellani V, et al (1999a) Theoretical Models for Classical Cepheids. II. Period-Luminosity, Period-Color, and Period-Luminosity-Color Relations. ApJ 512:711–723. https://doi.org/10.1086/306815, https://arxiv.org/abs/arXiv:astro-ph/9809127

Bono G, Marconi M, Stellingwerf RF (1999b) Classical Cepheid Pulsation Models. I. Physical Structure. ApJS 122:167–205. https://doi.org/10.1086/313207

Bono G, Caputo F, Cassisi S, et al (2000a) Intermediate-Mass Star Models with Different Helium and Metal Contents. ApJ 543:955–971. https://doi.org/10.1086/317156, https://arxiv.org/abs/arXiv:astro-ph/0006251

Bono G, Castellani V, Marconi M (2000b) Classical Cepheid Pulsation Models. III. The Predictable Scenario. ApJ 529:293–317. https://doi.org/10.1086/308263, https://arxiv.org/abs/arXiv:astro-ph/9908014

Bono G, Marconi M, Stellingwerf RF (2000c) Classical Cepheid pulsation models — VI. The Hertzsprung progression. A&A 360:245–262. https://arxiv.org/abs/astro-ph/0006229 [astro-ph]

Bono G, Caputo F, Castellani V, et al (2001) Theoretical insights into the RR Lyrae K-band period-luminosity relation. MNRAS 326:1183–1190. https://doi.org/10.1046/j.1365-8711.2001.04655.x, https://arxiv.org/abs/astro-ph/0105481

Bono G, Stetson PB, Sanna N, et al (2008) On the Relative Distances of ω Centauri and 47 Tucanae. ApJ 686:L87. https://doi.org/10.1086/593013, https://arxiv.org/

abs/0809.0863

Bono G, Caputo F, Marconi M, et al (2010) Insights into the Cepheid Distance Scale. ApJ 715(1):277–291. https://doi.org/10.1088/0004-637X/715/1/277, https://arxiv.org/abs/1004.0363 [astro-ph.SR]

Bono G, Iannicola G, Braga VF, et al (2019) On a New Method to Estimate the Distance, Reddening, and Metallicity of RR Lyrae Stars Using Optical/Near-infrared (B, V, I, J, H, K) Mean Magnitudes: ω Centauri as a First Test Case. ApJ 870:115. https://doi.org/10.3847/1538-4357/aaf23f, https://arxiv.org/abs/1811.07069 [astro-ph.SR]

Bono G, Braga VF, Crestani J, et al (2020a) On the Metamorphosis of the Bailey Diagram for RR Lyrae Stars. ApJ 896(1):L15. https://doi.org/10.3847/2041-8213/ab9538, https://arxiv.org/abs/2005.11566 [astro-ph.SR]

Bono G, Braga VF, Fiorentino G, et al (2020b) Evolutionary and pulsation properties of Type II Cepheids. A&A 644:A96. https://doi.org/10.1051/0004-6361/202038191, https://arxiv.org/abs/2009.06985 [astro-ph.SR]

Braga VF, Dall'Ora M, Bono G, et al (2015) On the Distance of the Globular Cluster M4 (NGC 6121) Using RR Lyrae Stars. I. Optical and Near-infrared Period-Luminosity and Period-Wesenheit Relations. ApJ 799(2):165. https://doi.org/10.1088/0004-637X/799/2/165, https://arxiv.org/abs/1411.6826 [astro-ph.GA]

Braga VF, Stetson PB, Bono G, et al (2019) New near-infrared JHK$_s$ light-curve templates for RR Lyrae variables. A&A 625:A1. https://doi.org/10.1051/0004-6361/201834893, https://arxiv.org/abs/1812.06372 [astro-ph.SR]

Braga VF, Bono G, Fiorentino G, et al (2020) Separation between RR Lyrae and type II Cepheids and their importance for a distance determination: the case of omega Cen. A&A 644:A95. https://doi.org/10.1051/0004-6361/202039145, https://arxiv.org/abs/2010.06368 [astro-ph.SR]

Breger M (1981) The unusual cepheid HR 7308 with a variable amplitude. ApJ 249:666–672. https://doi.org/10.1086/159327

Breuval L, Kervella P, Anderson RI, et al (2020) The Milky Way Cepheid Leavitt law based on Gaia DR2 parallaxes of companion stars and host open cluster populations. A&A 643:A115. https://doi.org/10.1051/0004-6361/202038633, https://arxiv.org/abs/2006.08763 [astro-ph.SR]

Breuval L, Kervella P, Wielgórski P, et al (2021) The Influence of Metallicity on the Leavitt Law from Geometrical Distances of Milky Way and Magellanic Cloud Cepheids. ApJ 913(1):38. https://doi.org/10.3847/1538-4357/abf0ae, https://arxiv.org/abs/2103.10894 [astro-ph.GA]

Breuval L, Riess AG, Kervella P, et al (2022) An Improved Calibration of the Wavelength Dependence of Metallicity on the Cepheid Leavitt Law. ApJ 939(2):89. https://doi.org/10.3847/1538-4357/ac97e2, https://arxiv.org/abs/2205.06280 [astro-ph.GA]

Brott I, Evans CJ, Hunter I, et al (2011) Rotating massive main-sequence stars. II. Simulating a population of LMC early B-type stars as a test of rotational mixing. A&A 530:A116. https://doi.org/10.1051/0004-6361/201016114, https://arxiv.org/abs/1102.0766 [astro-ph.SR]

Brown TM, Bowers CW, Kimble RA, et al (2000) Detection and Photometry of Hot Horizontal Branch Stars in the Core of M32. ApJ 532:308–322. https://doi.org/10.1086/308566, https://arxiv.org/abs/arXiv:astro-ph/9909391

Buchler JR, Kollath Z, Beaulieu JP, et al (1996) Do the Magellanic Cepheids Pose a New Puzzle? ApJ 462:L83. https://doi.org/10.1086/310036

Burki G, Mayor M (1980) HR 7308, a new cepheid with variable amplitude and very-short period (1.5d). A&A 91:115–121

Burris DL, Pilachowski CA, Armandroff TE, et al (2000) Neutron-Capture Elements in the Early Galaxy: Insights from a Large Sample of Metal-poor Giants. ApJ 544(1):302–319. https://doi.org/10.1086/317172, https://arxiv.org/abs/astro-ph/0005188 [astro-ph]

Caffau E, Ludwig HG, Steffen M, et al (2011) Solar Chemical Abundances Determined with a CO5BOLD 3D Model Atmosphere. Sol Phys 268(2):255–269. https://doi.org/10.1007/s11207-010-9541-4, https://arxiv.org/abs/1003.1190 [astro-ph.SR]

Calzetti D, Battisti AJ, Shivaei I, et al (2021) Revisiting Attenuation Curves: The Case of NGC 3351. ApJ 913(1):37. https://doi.org/10.3847/1538-4357/abf118, https://arxiv.org/abs/2103.12117 [astro-ph.GA]

Caputo F, Castellani V, Degl'Innocenti S, et al (2004) Bright metal-poor variables: Why "Anomalous" Cepheids? A&A 424:927–934. https://doi.org/10.1051/0004-6361:20040307, https://arxiv.org/abs/arXiv:astro-ph/0405395

Cardelli JA, Clayton GC, Mathis JS (1989) The relationship between infrared, optical, and ultraviolet extinction. ApJ 345:245–256. https://doi.org/10.1086/167900

Carraro G, Geisler D, Villanova S, et al (2007) Old open clusters in the outer Galactic disk. A&A 476(1):217–227. https://doi.org/10.1051/0004-6361:20078113, https://arxiv.org/abs/0709.2126 [astro-ph]

Carson TR, Stothers RB (1988) Classical Bump Cepheids: Reconcilliation of Theory with Observations. ApJ 328:196. https://doi.org/10.1086/166281

Cassisi S, Salaris M (2011) A Classical Cepheid in a Large Magellanic Cloud Eclipsing Binary: Evidence Of Shortcomings in Current Stellar Evolutionary Models? ApJ 728:L43. https://doi.org/10.1088/2041-8205/728/2/L43, https://arxiv.org/abs/1101.0394 [astro-ph.SR]

Castellani M, Castellani V, Prada Moroni PG (2006) Hot flashers and He dwarfs in galactic globulars. A&A 457:569–573. https://doi.org/10.1051/0004-6361:20064875, https://arxiv.org/abs/astro-ph/0606026

Castellani V, degl'Innocenti S (1995) Dwarf spheroidals and the evolution of not-too-old Population II stars. A&A 298:827. https://arxiv.org/abs/arXiv:astro-ph/9406058

Castellani V, Chieffi A, Pulone L (1991) The evolution of He-burning stars - Horizontal and asymptotic branches in Galactic globulars. ApJS 76:911–977. https://doi.org/10.1086/191584

Castelli F, Kurucz RL (2004) New Grids of ATLAS9 Model Atmospheres. ArXiv Astrophysics e-prints https://arxiv.org/abs/astro-ph/0405087

Cescutti G, Matteucci F, François P, et al (2007) Abundance gradients in the Milky Way for α elements, iron peak elements, barium, lanthanum, and europium. A&A 462(3):943–951. https://doi.org/10.1051/0004-6361:20065403, https://arxiv.org/abs/astro-ph/0609813 [astro-ph]

Chiavassa A, Casagrande L, Collet R, et al (2018) The STAGGER-grid: A grid of 3D stellar atmosphere models. V. Synthetic stellar spectra and broad-band photometry. A&A 611:A11. https://doi.org/10.1051/0004-6361/201732147, https://arxiv.org/abs/1801.01895 [astro-ph.SR]

Chiosi C, Bertelli G, Bressan A (1992) New developments in understanding the HR diagram. ARA&A 30:235–285. https://doi.org/10.1146/annurev.aa.30.090192.001315

Christy RF (1968) Cepheid Variables in the Magellanic Clouds. The Astronomical Journal Supplement 73:170

Christy RF (1970) Lectures on Variable Stars (concluded). JRASC 64:8

Christy RF (1975) The Hertzsprung progression in cepheid calculations. Memoires of the Societe Royale des Sciences de Liege 8:173–181

Cioni MRL, Clementini G, Girardi L, et al (2011) The VMC survey. I. Strategy and first data. A&A 527:A116. https://doi.org/10.1051/0004-6361/201016137, https://arxiv.org/abs/1012.5193 [astro-ph.CO]

Cioni MRL, Girardi L, Moretti MI, et al (2014) The VMC survey. IX. Pilot study

of the proper motion of stellar populations in the LMC from 2MASS and VISTA data. A&A 562:A32. https://doi.org/10.1051/0004-6361/201322100, https://arxiv.org/abs/1306.4336 [astro-ph.GA]

Collet R, Asplund M, Thévenin F (2005) Effects of line-blocking on the non-LTE Fe I spectral line formation. A&A 442(2):643–650. https://doi.org/10.1051/0004-6361:20053363, https://arxiv.org/abs/astro-ph/0507375 [astro-ph]

Constantino T, Campbell SW, Lattanzio JC, et al (2016) The treatment of mixing in core helium burning models - II. Constraints from cluster star counts. MNRAS 456:3866–3885. https://doi.org/10.1093/mnras/stv2939, https://arxiv.org/abs/1512.04845 [astro-ph.SR]

Costa G, Girardi L, Bressan A, et al (2019) Multiple stellar populations in NGC 1866. New clues from Cepheids and colour-magnitude diagram. A&A 631:A128. https://doi.org/10.1051/0004-6361/201936409, https://arxiv.org/abs/1909.01907 [astro-ph.SR]

Cox AN, King DS, Hodson SW (1980) Theoretical period ratios for RR LYR variables and AQ Leo. ApJ 236:219–224. https://doi.org/10.1086/157736

Cristallo S, Straniero O, Gallino R, et al (2009) Evolution, Nucleosynthesis, and Yields of Low-Mass Asymptotic Giant Branch Stars at Different Metallicities. ApJ 696:797–820. https://doi.org/10.1088/0004-637X/696/1/797, https://arxiv.org/abs/0902.0243 [astro-ph.SR]

Croswell K (1997) The First Cepheid. S&T 94(4):90

da Silva R, Lemasle B, Bono G, et al (2016) Neutron-capture elements across the Galactic thin disk using Cepheids. A&A 586:A125. https://doi.org/10.1051/0004-6361/201527300, https://arxiv.org/abs/1510.06314 [astro-ph.SR]

da Silva R, Crestani J, Bono G, et al (2022) A new and Homogeneous metallicity scale for Galactic classical Cepheids. II. Abundance of iron and α elements. A&A 661:A104. https://doi.org/10.1051/0004-6361/202142957, https://arxiv.org/abs/2202.07945 [astro-ph.SR]

da Silva R, D'Orazi V, Palla M, et al (2023) Oxygen, sulfur, and iron radial abundance gradients of classical Cepheids across the Galactic thin disk. arXiv e-prints arXiv:2308.01928. https://doi.org/10.48550/arXiv.2308.01928, https://arxiv.org/abs/2308.01928 [astro-ph.GA]

Dalessandro E, Lapenna E, Mucciarelli A, et al (2016) Multiple Populations in the Old and Massive Small Magellanic Cloud Globular Cluster NGC 121. ApJ 829(2):77. https://doi.org/10.3847/0004-637X/829/2/77, https://arxiv.org/abs/1607.05736 [astro-ph.SR]

Das S, Kanbur SM, Bellinger EP, et al (2020) The stellar photosphere-hydrogen ionization front interaction in classical pulsators: a theoretical explanation for observed period-colour relations. MNRAS 493(1):29–47. https://doi.org/10.1093/mnras/staa182, https://arxiv.org/abs/2001.06818 [astro-ph.SR]

de Grijs R, Bono G (2017) Clustering of Local Group Distances: Publication Bias or Correlated Measurements? V. Galactic Rotation Constants. ApJS 232(2):22. https://doi.org/10.3847/1538-4365/aa8b71, https://arxiv.org/abs/1709.02501 [astro-ph.GA]

De Somma G, Marconi M, Cassisi S, et al (2021) Period-age-metallicity and period-age-colour-metallicity relations for classical Cepheids: an application to the Gaia EDR3 sample. MNRAS 508(1):1473–1488. https://doi.org/10.1093/mnras/stab2611, https://arxiv.org/abs/2109.05850 [astro-ph.SR]

Den Hartog EA, Ruffoni MP, Lawler JE, et al (2014) Fe I Oscillator Strengths for Transitions from High-lying Even-parity Levels. ApJS 215(2):23. https://doi.org/10.1088/0067-0049/215/2/23, https://arxiv.org/abs/1409.8142 [astro-ph.SR]

Den Hartog EA, Lawler JE, Sneden C, et al (2019) Atomic Transition Probabilities for UV and Blue Lines of Fe II and Abundance Determinations in the Photospheres of the Sun and Metal-poor Star HD 84937. ApJS 243(2):33. https://doi.org/10.3847/1538-4365/ab322e, https://arxiv.org/abs/1907.11760 [astro-ph.SR]

Diethelm R (1983) A photometric classification of pulsating variables with periods between one and three days. A&A 124:108–115

Diethelm R (1990) Physical parameters of pulsating variables with periods between one and three days. II - Fundamental parameters. A&A 239:186–192

Dobbie PD, Cole AA, Subramaniam A, et al (2014) Red giants in the Small Magellanic Cloud - I. Disc and tidal stream kinematics. MNRAS 442(2):1663–1679. https://doi.org/10.1093/mnras/stu910, https://arxiv.org/abs/1405.3705 [astro-ph.GA]

Donor J, Frinchaboy PM, Cunha K, et al (2020) The Open Cluster Chemical Abundances and Mapping Survey. IV. Abundances for 128 Open Clusters Using SDSS/APOGEE DR16. AJ 159(5):199. https://doi.org/10.3847/1538-3881/ab77bc, https://arxiv.org/abs/2002.08980 [astro-ph.GA]

Dorman B, Rood RT (1993) On partial mixing zones in horizontal-branch stellar cores. ApJ 409:387–403. https://doi.org/10.1086/172671

Dotter A (2008) Horizontal-Branch Morphology and Mass Loss in Globular Clusters. ApJ 687:L21. https://doi.org/10.1086/593149, https://arxiv.org/abs/0809.2603

Duffau S, Caffau E, Sbordone L, et al (2017) The Gaia-ESO Survey: Galactic evolution of sulphur and zinc. A&A 604:A128. https://doi.org/10.1051/0004-6361/201730477, https://arxiv.org/abs/1704.02981 [astro-ph.SR]

Evans NR, Sasselov DD, Short CI (2002) Polaris: Amplitude, Period Change, and Companions. ApJ 567(2):1121–1130. https://doi.org/10.1086/338583

Evans NR, Schaefer GH, Bond HE, et al (2008) Direct Detection of the Close Companion of Polaris with the Hubble Space Telescope. AJ 136(3):1137–1146. https://doi.org/10.1088/0004-6256/136/3/1137, https://arxiv.org/abs/0806.4904 [astro-ph]

Fabrizio M, Braga VF, Crestani J, et al (2021) On the Use of Field RR Lyrae As Galactic Probes: IV. New Insights Into and Around the Oosterhoff Dichotomy. ApJ 919(2):118. https://doi.org/10.3847/1538-4357/ac1115, https://arxiv.org/abs/2107.00919 [astro-ph.SR]

Feast MW, Whitelock PA (2013) Variable Stars and Galactic Structure. ArXiv e-prints https://arxiv.org/abs/1310.3928 [astro-ph.GA]

Feast MW, Laney CD, Kinman TD, et al (2008) The luminosities and distance scales of type II Cepheid and RR Lyrae variables. MNRAS 386:2115–2134. https://doi.org/10.1111/j.1365-2966.2008.13181.x, https://arxiv.org/abs/0803.0466

Fiorentino G, Monelli M (2012) Anomalous Cepheids in the Large Magellanic Cloud. Insight into their origin and connection with the star formation history. A&A 540:A102. https://doi.org/10.1051/0004-6361/201118621, https://arxiv.org/abs/1202.2752 [astro-ph.SR]

Fiorentino G, Caputo F, Marconi M, et al (2002) Theoretical Models for Classical Cepheids. VIII. Effects of Helium and Heavy-Element Abundance on the Cepheid Distance Scale. ApJ 576:402–412. https://doi.org/10.1086/341731, https://arxiv.org/abs/arXiv:astro-ph/0205147

Fiorentino G, Lanzoni B, Dalessandro E, et al (2014) Blue Straggler Masses from Pulsation Properties. I. The Case of NGC 6541. ApJ 783:34. https://doi.org/10.1088/0004-637X/783/1/34, https://arxiv.org/abs/1312.0388 [astro-ph.SR]

Fiorentino G, Bellazzini M, Spera M, et al (2020) Deep into the core of dense star clusters: an astrometric and photometric test case for ELT. MNRAS 494(3):4413–4425. https://doi.org/10.1093/mnras/staa869

Freedman WL, Madore BF (2010) The Hubble Constant. ARA&A 48:673–710. https://doi.org/10.1146/annurev-astro-082708-101829, https://arxiv.org/abs/1004.1856 [astro-ph.CO]

Freeman K, Bland-Hawthorn J (2002) The New Galaxy: Signatures of Its Formation. ARA&A 40:487–537. https://doi.org/10.1146/annurev.astro.40.060401.093840, https://arxiv.org/abs/astro-ph/0208106 [astro-ph]

Fricke K, Stobie RS, Strittmatter PA (1972) The Masses of Cepheid Variables. ApJ 171:593. https://doi.org/10.1086/151313

Gascoigne SCB, Kron GE (1965) Photoelectric observations of Magellanic Cloud cepheids. MNRAS 130:333. https://doi.org/10.1093/mnras/130.5.333

Gautschy A, Saio H (1995) Stellar Pulsations Across The HR Diagram: Part 1. ARA&A 33:75–114. https://doi.org/10.1146/annurev.aa.33.090195.000451

Gautschy A, Saio H (1996) Stellar Pulsations Across the HR Diagram: Part 2. ARA&A 34:551–606. https://doi.org/10.1146/annurev.astro.34.1.551

Genovali K, Lemasle B, Bono G, et al (2013) On the metallicity distribution of classical Cepheids in the Galactic inner disk. A&A 554:A132. https://doi.org/10.1051/0004-6361/201321650, https://arxiv.org/abs/1305.2742 [astro-ph.SR]

Genovali K, Lemasle B, Bono G, et al (2014) On the fine structure of the Cepheid metallicity gradient in the Galactic thin disk. A&A 566:A37. https://doi.org/10.1051/0004-6361/201323198, https://arxiv.org/abs/1403.6128 [astro-ph.GA]

Genovali K, Lemasle B, da Silva R, et al (2015) On the α-element gradients of the Galactic thin disk using Cepheids. A&A 580:A17. https://doi.org/10.1051/0004-6361/201525894, https://arxiv.org/abs/1503.03758 [astro-ph.SR]

Gerber JM, Magg E, Plez B, et al (2023) Non-LTE radiative transfer with Turbospectrum. A&A 669:A43. https://doi.org/10.1051/0004-6361/202243673, https://arxiv.org/abs/2206.00967 [astro-ph.SR]

Gieren W, Pilecki B, Pietrzyński G, et al (2015) The Araucaria Project: A Study of the Classical Cepheid in the Eclipsing Binary System OGLE LMC562.05.9009 in the Large Magellanic Cloud. ApJ 815(1):28. https://doi.org/10.1088/0004-637X/815/1/28, https://arxiv.org/abs/1511.02826 [astro-ph.SR]

Gingold RA (1974) Asymptotic Giant-Branch Evolution of a 0.6 m, Star. ApJ 193:177–186. https://doi.org/10.1086/153144

Gingold RA (1976) The evolutionary status of Population II Cepheids. ApJ 204:116–130. https://doi.org/10.1086/154156

Gingold RA (1985) The evolutionary status of Type II Cepheids. Mem Soc Astron Italiana 56:169–191

Girardi L (2016) Red Clump Stars. ARA&A 54:95–133. https://doi.org/10.1146/annurev-astro-081915-023354

González-Fernández C, Hodgkin ST, Irwin MJ, et al (2018) The VISTA ZYJHKs photometric system: calibration from 2MASS. MNRAS 474(4):5459–5478. https://doi.org/10.1093/mnras/stx3073, https://arxiv.org/abs/1711.08805 [astro-ph.IM]

Graczyk D, Pietrzyński G, Thompson IB, et al (2012) The Araucaria Project: An Accurate Distance to the Late-type Double-lined Eclipsing Binary OGLE SMC113.3 4007 in the Small Magellanic Cloud. ApJ 750(2):144. https://doi.org/10.1088/0004-637X/750/2/144, https://arxiv.org/abs/1203.2517 [astro-ph.CO]

Graczyk D, Pietrzyński G, Thompson IB, et al (2020) A Distance Determination to the Small Magellanic Cloud with an Accuracy of Better than Two Percent Based on Late-type Eclipsing Binary Stars. ApJ 904(1):13. https://doi.org/10.3847/1538-4357/abbb2b, https://arxiv.org/abs/2010.08754 [astro-ph.GA]

Gratton RG, Bragaglia A, Clementini G, et al (2004) Metal abundances of RR Lyrae stars in the bar of the Large Magellanic Cloud. A&A 421:937–952. https://doi.org/10.1051/0004-6361:20035840, https://arxiv.org/abs/arXiv:astro-ph/0405412

Greggio L, Renzini A (1990) Clues on the hot star content and the ultraviolet output of elliptical galaxies. ApJ 364:35–64. https://doi.org/10.1086/169384

Groenewegen MAT (2018) The Cepheid period-luminosity-metallicity relation based on Gaia DR2 data. A&A 619:A8. https://doi.org/10.1051/0004-6361/201833478, https://arxiv.org/abs/1808.05796 [astro-ph.SR]

Gustafsson B, Edvardsson B, Eriksson K, et al (2008) A grid of MARCS model atmospheres for late-type stars. I. Methods and general properties. A&A 486:951–970. https://doi.org/10.1051/0004-6361:200809724, https://arxiv.org/abs/0805.0554

Hansen CJ, Bergemann M, Cescutti G, et al (2013) LTE or non-LTE, that is the question. The NLTE chemical evolution of strontium in extremely metal-poor stars. A&A 551:A57. https://doi.org/10.1051/0004-6361/201220584

Henry RBC, Kwitter KB, Jaskot AE, et al (2010) Abundances of Galactic Anticenter Planetary Nebulae and the Oxygen Abundance Gradient in the Galactic Disk. ApJ 724(1):748–761. https://doi.org/10.1088/0004-637X/724/1/748, https://arxiv.org/abs/1009.1921 [astro-ph.GA]

Hertzsprung E (1926) On the relation between period and form of the light-curve of variable stars of the δ Cephei type. Bull Astron Inst Netherlands 3:115

Hocdé V, Smolec R, Moskalik P, et al (2022) Metallicity estimation of MW, SMC and LMC classical Cepheids from the shape of the V- and I-band light curves. arXiv e-prints arXiv:2301.00229. https://doi.org/10.48550/arXiv.2301.00229, https://arxiv.org/abs/2301.00229 [astro-ph.SR]

Hoskin M (1979) Goodricke, Pigott and the Quest for Variable Stars. Journal for the

History of Astronomy 10:23. https://doi.org/10.1177/002182867901000103

Hubble EP (1925) Cepheids in Spiral Nebulae. Popular Astronomy 33:252–255

Hubble EP (1929) A spiral nebula as a stellar system, Messier 31. ApJ 69:103–158. https://doi.org/10.1086/143167

Hunter I, Brott I, Lennon DJ, et al (2008) The VLT FLAMES Survey of Massive Stars: Rotation and Nitrogen Enrichment as the Key to Understanding Massive Star Evolution. ApJ 676(1):L29. https://doi.org/10.1086/587436, https://arxiv.org/abs/0711.2267 [astro-ph]

Hunter I, Brott I, Langer N, et al (2009) The VLT-FLAMES survey of massive stars: constraints on stellar evolution from the chemical compositions of rapidly rotating Galactic and Magellanic Cloud B-type stars. A&A 496(3):841–853. https://doi.org/10.1051/0004-6361/200809925, https://arxiv.org/abs/0901.3853 [astro-ph.SR]

Iben IJr., Truran JW (1978) On the surface composition of thermally pulsing stars of high luminosity and on the contribution of such stars to the element enrichment of the interstellar medium. ApJ 220:980–995. https://doi.org/10.1086/155986

Idiart T, Thévenin F (2000) Non-LTE Abundances and Consequences for the Evolution of the α-Elements in the Galaxy. ApJ 541(1):207–217. https://doi.org/10.1086/309416, https://arxiv.org/abs/astro-ph/0004337 [astro-ph]

Inno L, Matsunaga N, Bono G, et al (2013) On the Distance of the Magellanic Clouds Using Cepheid NIR and Optical-NIR Period-Wesenheit Relations. ApJ 764(1):84. https://doi.org/10.1088/0004-637X/764/1/84, https://arxiv.org/abs/1212.4376 [astro-ph.SR]

Inno L, Matsunaga N, Romaniello M, et al (2015) New NIR light-curve templates for classical Cepheids. A&A 576:A30. https://doi.org/10.1051/0004-6361/201424396, https://arxiv.org/abs/1410.5460 [astro-ph.SR]

Inno L, Bono G, Matsunaga N, et al (2016) The Panchromatic View of the Magellanic Clouds from Classical Cepheids. I. Distance, Reddening, and Geometry of the Large Magellanic Cloud Disk. ApJ 832:176. https://doi.org/10.3847/0004-637X/832/2/176, https://arxiv.org/abs/1609.03554

Inno L, Urbaneja MA, Matsunaga N, et al (2019) First metallicity determination from near-infrared spectra for five obscured Cepheids discovered in the inner disc. MNRAS 482(1):83–97. https://doi.org/10.1093/mnras/sty2661, https://arxiv.org/abs/1805.03212 [astro-ph.GA]

Ita Y, Tanabé T, Matsunaga N, et al (2004) Variable stars in the Magellanic Clouds - II. The data and infrared properties. MNRAS 353(3):705–712.

https://doi.org/10.1111/j.1365-2966.2004.08126.x, https://arxiv.org/abs/astro-ph/0312079 [astro-ph]

Ita Y, Matsunaga N, Tanabé T, et al (2018) A near-infrared variable star survey in the Magellanic Clouds: the Small Magellanic Cloud data. MNRAS 481(3):4206–4220. https://doi.org/10.1093/mnras/sty2539, https://arxiv.org/abs/1810.01617 [astro-ph.SR]

Jacyszyn-Dobrzeniecka AM, Skowron DM, Mróz P, et al (2016) OGLE-ing the Magellanic System: Three-Dimensional Structure of the Clouds and the Bridge Using Classical Cepheids. Acta Astron 66(2):149–196. https://doi.org/10.48550/arXiv.1602.09141, https://arxiv.org/abs/1602.09141 [astro-ph.GA]

Joy AH (1937) Radial Velocities of Cepheid Variable Stars. ApJ 86:363. https://doi.org/10.1086/143874

Joy AH (1939) Rotation Effects, Interstellar Absorption, and Certain Dynamical Constants of the Galaxy Determined from Cepheid Variables. ApJ 89:356. https://doi.org/10.1086/144060

Kanbur SM, Simon NR (1994) Comparative Pulsation Calculations with OP and Opal Opacities. ApJ 420:880. https://doi.org/10.1086/173611

Kanbur SM, Ngeow CC, Feiden G (2007) Period-colour and amplitude-colour relations in classical Cepheid variables - V. The Small Magellanic Cloud Cepheid models. MNRAS 380(2):819–827. https://doi.org/10.1111/j.1365-2966.2007.12123.x, https://arxiv.org/abs/0706.2629 [astro-ph]

Kato D, Nagashima C, Nagayama T, et al (2007) The IRSF Magellanic Clouds Point Source Catalog. PASJ 59:615–641. https://doi.org/10.1093/pasj/59.3.615

Kippenhahn R, Ruschenplatt G, Thomas HC (1980) The time scale of secularly unstable stellar rotation. A&A 91(1-2):181–185

Kiselman D (2001) NLTE effects on oxygen lines. New A Rev 45(8):559–563. https://doi.org/10.1016/S1387-6473(01)00127-0, https://arxiv.org/abs/astro-ph/0010300 [astro-ph]

Kobayashi C, Umeda H, Nomoto K, et al (2006) Galactic Chemical Evolution: Carbon through Zinc. ApJ 653(2):1145–1171. https://doi.org/10.1086/508914, https://arxiv.org/abs/astro-ph/0608688 [astro-ph]

Kobayashi C, Karakas AI, Umeda H (2011) The evolution of isotope ratios in the Milky Way Galaxy. MNRAS 414(4):3231–3250. https://doi.org/10.1111/j.1365-2966.2011.18621.x, https://arxiv.org/abs/1102.5312 [astro-ph.GA]

Kovtyukh V, Wallerstein G, Yegorova I, et al (2018) Metal-poor Type II Cepheids

with Periods Less Than Three Days. PASP 130(5):054,201. https://doi.org/10.1088/1538-3873/aaacf7, https://arxiv.org/abs/1803.05041 [astro-ph.SR]

Kovtyukh VV, Andrievsky SM, Belik SI, et al (2005) Phase-dependent Variation of the Fundamental Parameters of Cepheids. II. Periods Longer than 10 Days. AJ 129:433–453. https://doi.org/10.1086/426339

Kovtyukh VV, Korotin SA, Andrievsky SM, et al (2022) Chemical properties of the central part of the Galactic nuclear stellar disc. Abundances in four classical Cepheids revisited. MNRAS 516(3):4269–4275. https://doi.org/10.1093/mnras/stac2468

Kraft RP (1963) The Absolute Magnitudes of Classical Cepheids. In: Strand KA (ed) Basic Astronomical Data: Stars and Stellar Systems. p 421

Kramida A, Yu. R, Reader J, et al (2020) NIST Atomic Spectra Database. https://doi.org/10.18434/T4W30F, URL https://physics.nist.gov/asd, version 5.8

Kubryk M, Prantzos N, Athanassoula E (2015) Evolution of the Milky Way with radial motions of stars and gas. I. The solar neighbourhood and the thin and thick disks. A&A 580:A126. https://doi.org/10.1051/0004-6361/201424171, https://arxiv.org/abs/1412.0585 [astro-ph.GA]

Kukarkin BV, Parenago PP (1949) Book reviews: General Catalogue of Variable Stars. Popular Astronomy 57:473

Kurbah K, Deb S, Kanbur SM, et al (2023) A multiphase study of theoretical and observed light curves of classical Cepheids in the Magellanic Clouds. MNRAS 521(4):6034–6052. https://doi.org/10.1093/mnras/stad806, https://arxiv.org/abs/2303.08393 [astro-ph.SR]

Laney CD, Caldwell JAR (2007) The reliability of Cepheid reddenings based on BVI_C photometry. MNRAS 377(1):147–158. https://doi.org/10.1111/j.1365-2966.2007.11574.x

Laney CD, Stobie RS (1994) Cepheid period-luminosity relations in K, H, J and V. MNRAS 266:441–454. https://doi.org/10.1093/mnras/266.2.441

Lawler JE, Guzman A, Wood MP, et al (2013) Improved Log(gf) Values for Lines of Ti I and Abundance Determinations in the Photospheres of the Sun and Metal-Poor Star HD 84937 (Accurate Transition Probabilities for Ti I). ApJS 205(2):11. https://doi.org/10.1088/0067-0049/205/2/11

Leavitt HS (1908) 1777 variables in the Magellanic Clouds. Annals of Harvard College Observatory 60:87–108.3

Leavitt HS, Pickering EC (1912) Periods of 25 Variable Stars in the Small Magellanic

Cloud. Harvard College Observatory Circular 173:1–3

Ledoux P, Walraven T (1958) Variable Stars. Handbuch der Physik 51:353–604. https://doi.org/10.1007/978-3-642-45908-5_6

Lee YW, Demarque P, Zinn R (1990) The horizontal-branch stars in globular clusters. I - The period-shift effect, the luminosity of the horizontal branch, and the age-metallicity relation. ApJ 350:155–172. https://doi.org/10.1086/168370

Lemasle B, François P, Bono G, et al (2007) Detailed chemical composition of Galactic Cepheids. A determination of the Galactic abundance gradient in the 8-12 kpc region. A&A 467(1):283–294. https://doi.org/10.1051/0004-6361:20066375, https://arxiv.org/abs/astro-ph/0701499 [astro-ph]

Lemasle B, François P, Genovali K, et al (2013) Galactic abundance gradients from Cepheids. α and heavy elements in the outer disk. A&A 558:A31. https://doi.org/10.1051/0004-6361/201322115, https://arxiv.org/abs/1308.3249

Lemasle B, Groenewegen MAT, Grebel EK, et al (2017) Detailed chemical composition of classical Cepheids in the LMC cluster NGC 1866 and in the field of the SMC. A&A 608:A85. https://doi.org/10.1051/0004-6361/201731370, https://arxiv.org/abs/1709.03083 [astro-ph.GA]

Lemasle B, Hanke M, Storm J, et al (2020) Atmospheric parameters of Cepheids from flux ratios with ATHOS. I. The temperature scale. A&A 641:A71. https://doi.org/10.1051/0004-6361/202038277, https://arxiv.org/abs/2006.14638 [astro-ph.SR]

Lemasle B, Lala HN, Kovtyukh V, et al (2022) Tracing the Milky Way warp and spiral arms with classical Cepheids. A&A 668:A40. https://doi.org/10.1051/0004-6361/202243273, https://arxiv.org/abs/2209.02731 [astro-ph.GA]

Limongi M, Chieffi A (2018) Presupernova Evolution and Explosive Nucleosynthesis of Rotating Massive Stars in the Metallicity Range -3 $\leq$ [Fe/H] $\leq$ 0. ApJS 237(1):13. https://doi.org/10.3847/1538-4365/aacb24, https://arxiv.org/abs/1805.09640 [astro-ph.SR]

Lind K, Bergemann M, Asplund M (2012) Non-LTE line formation of Fe in late-type stars - II. 1D spectroscopic stellar parameters. MNRAS 427(1):50–60. https://doi.org/10.1111/j.1365-2966.2012.21686.x, https://arxiv.org/abs/1207.2454 [astro-ph.SR]

Luck RE (2014) Parameters and Abundances in Luminous Stars. AJ 147(6):137. https://doi.org/10.1088/0004-6256/147/6/137

Luck RE, Lambert DL (2011) The Distribution of the Elements in the Galactic Disk. III. A Reconsideration of Cepheids from l = 30° to 250°. AJ

142(4):136. https://doi.org/10.1088/0004-6256/142/4/136, https://arxiv.org/abs/1108.1947 [astro-ph.GA]

Luck RE, Andrievsky SM, Kovtyukh VV, et al (2011) The Distribution of the Elements in the Galactic Disk. II. Azimuthal and Radial Variation in Abundances from Cepheids. AJ 142(2):51. https://doi.org/10.1088/0004-6256/142/2/51, https://arxiv.org/abs/1106.0182 [astro-ph.GA]

Maas T, Giridhar S, Lambert DL (2007) The Chemical Compositions of the Type II Cepheids-The BL Herculis and W Virginis Variables. ApJ 666:378–392. https://doi.org/10.1086/520081, https://arxiv.org/abs/0706.2029

Maciel WJ, Costa RDD, Uchida MMM (2003) An estimate of the time variation of the O/H radial gradient from planetary nebulae. A&A 397:667–674. https://doi.org/10.1051/0004-6361:20021530, https://arxiv.org/abs/astro-ph/0210470 [astro-ph]

Macri LM, Ngeow CC, Kanbur SM, et al (2015) Large Magellanic Cloud Near-Infrared Synoptic Survey. I. Cepheid Variables and the Calibration of the Leavitt Law. AJ 149:117. https://doi.org/10.1088/0004-6256/149/4/117, https://arxiv.org/abs/1412.1511 [astro-ph.SR]

Madore BF (1982) The period-luminosity relation. IV - Intrinsic relations and reddenings for the Large Magellanic Cloud Cepheids. ApJ 253:575–579. https://doi.org/10.1086/159659

Madore BF, Freedman WL (1985) The search, discovery and use of cepheid variables as distance indicators : past procedures and future strategies. AJ 90:1104–1112. https://doi.org/10.1086/113817

Madore BF, Freedman WL (1991) The Cepheid Distance Scale. PASP 103:933. https://doi.org/10.1086/132911

Madore BF, Freedman WL (2023) Population II Distance Indicators: RR Lyrae Variables, Tip of the Red Giant Branch (TRGB) Stars and J-Branch Asymptotic Giant Branch (JAGB/Carbon) Stars. arXiv e-prints arXiv:2305.19437. https://doi.org/10.48550/arXiv.2305.19437, https://arxiv.org/abs/2305.19437 [astro-ph.SR]

Maeder A, Meynet G (2000) The Evolution of Rotating Stars. ARA&A 38:143–190. https://doi.org/10.1146/annurev.astro.38.1.143, https://arxiv.org/abs/astro-ph/0004204 [astro-ph]

Magic Z, Chiavassa A, Collet R, et al (2015) The Stagger-grid: A grid of 3D stellar atmosphere models. IV. Limb darkening coefficients. A&A 573:A90. https://doi.org/10.1051/0004-6361/201423804, https://arxiv.org/abs/1403.3487 [astro-ph.SR]

Magrini L, Viscasillas Vázquez C, Spina L, et al (2023) The Gaia-ESO survey: Mapping the shape and evolution of the radial abundance gradients with open clusters. A&A 669:A119. https://doi.org/10.1051/0004-6361/202244957, https://arxiv.org/abs/2210.15525 [astro-ph.GA]

Marconi M, Minniti D (2018) Gauging the Helium Abundance of the Galactic Bulge RR Lyrae Stars. ApJ 853:L20. https://doi.org/10.3847/2041-8213/aaa8e3, https://arxiv.org/abs/1801.05883 [astro-ph.SR]

Marconi M, Musella I, Fiorentino G (2005) Cepheid Pulsation Models at Varying Metallicity and $\Delta Y/\Delta Z$. ApJ 632:590–610. https://doi.org/10.1086/432790, https://arxiv.org/abs/arXiv:astro-ph/0506207

Marconi M, Molinaro R, Ripepi V, et al (2013) Theoretical fit of Cepheid light a radial velocity curves in the Large Magellanic Cloud cluster NGC 1866. MNRAS 428:2185–2197. https://doi.org/10.1093/mnras/sts197, https://arxiv.org/abs/1210.4343 [astro-ph.SR]

Marconi M, Coppola G, Bono G, et al (2015) On a New Theoretical Framework for RR Lyrae Stars. I. The Metallicity Dependence. ApJ 808:50. https://doi.org/10.1088/0004-637X/808/1/50, https://arxiv.org/abs/1505.02531 [astro-ph.SR]

Marconi M, Bono G, Pietrinferni A, et al (2018) On the Impact of Helium Content on the RR Lyrae Distance Scale. ApJ 864:L13. https://doi.org/10.3847/2041-8213/aada17, https://arxiv.org/abs/1808.07348 [astro-ph.SR]

Marengo M, Evans NR, Barmby P, et al (2010) An Infrared Nebula Associated with δ Cephei: Evidence of Mass Loss? ApJ 725(2):2392–2400. https://doi.org/10.1088/0004-637X/725/2/2392, https://arxiv.org/abs/1102.0305 [astro-ph.SR]

Martin RP, Andrievsky SM, Kovtyukh VV, et al (2015) Oxygen, α-element and iron abundance distributions in the inner part of the Galactic thin disc. MNRAS 449(4):4071–4078. https://doi.org/10.1093/mnras/stv590, https://arxiv.org/abs/1503.05898 [astro-ph.GA]

Matsunaga N, Fukushi H, Nakada Y, et al (2006) The period-luminosity relation for type II Cepheids in globular clusters. MNRAS 370:1979–1990. https://doi.org/10.1111/j.1365-2966.2006.10620.x, https://arxiv.org/abs/astro-ph/0606609

Matsunaga N, Feast MW, Menzies JW (2009) Period-luminosity relations for type II Cepheids and their application. MNRAS 397:933–942. https://doi.org/10.1111/j.1365-2966.2009.14992.x, https://arxiv.org/abs/0904.4701 [astro-ph.SR]

Matsunaga N, Feast MW, Soszyński I (2011) Period-luminosity relations of type II Cepheids in the Magellanic Clouds. MNRAS 413:223–234. https://doi.org/10.1111/j.1365-2966.2010.18126.x, https://arxiv.org/abs/1012.0098 [astro-ph.SR]

Matsunaga N, Taniguchi D, Elgueta SS, et al (2023) Metallicities of Classical Cepheids in the Inner Galactic Disk. arXiv e-prints arXiv:2308.02853. https://doi.org/10.48550/arXiv.2308.02853, https://arxiv.org/abs/2308.02853 [astro-ph.SR]

Matteucci F (2021) Modelling the chemical evolution of the Milky Way. A&A Rev 29(1):5. https://doi.org/10.1007/s00159-021-00133-8, https://arxiv.org/abs/2106.13145 [astro-ph.GA]

McAlary CW, Madore BF, McGonegal R, et al (1983) The distance to NGC 6822 from infrared photometry of cepheids. ApJ 273:539–543. https://doi.org/10.1086/161390

McGonegal R, McAlary CW, Madore BF, et al (1982) The Cepheid distance scale - A new application for infrared photometry. ApJ 257:L33–L36. https://doi.org/10.1086/183803

McGonegal R, McAlary CW, McLaren RA, et al (1983) The near-infrared cepheid distance scale. I. Preliminary galactic calibration. ApJ 269:641–644. https://doi.org/10.1086/161071

Medina GE, Lemasle B, Grebel EK (2021) A revisited study of Cepheids in open clusters in the Gaia era. MNRAS 505(1):1342–1366. https://doi.org/10.1093/mnras/stab1267, https://arxiv.org/abs/2104.14565 [astro-ph.GA]

Meléndez J, Barbuy B (2009) Both accurate and precise gf-values for Fe II lines. A&A 497(2):611–617. https://doi.org/10.1051/0004-6361/200811508, https://arxiv.org/abs/0901.4451 [astro-ph.SR]

Merle T, Thévenin F, Pichon B, et al (2011) A grid of non-local thermodynamic equilibrium corrections for magnesium and calcium in late-type giant and supergiant stars: application to Gaia. MNRAS 418(2):863–887. https://doi.org/10.1111/j.1365-2966.2011.19540.x, https://arxiv.org/abs/1107.6015 [astro-ph.SR]

Merrill PW (1952a) Spectroscopic Observations of Stars of Class S. ApJ 116:21. https://doi.org/10.1086/145589

Merrill PW (1952b) Technetium in the Stars. Science 115(2992):484. https://doi.org/10.1126/science.115.2992.479

Minchev I, Chiappini C, Martig M (2014) Chemodynamical evolution of the Milky Way disk. II. Variations with Galactic radius and height above the disk plane. A&A 572:A92. https://doi.org/10.1051/0004-6361/201423487, https://arxiv.org/abs/1401.5796 [astro-ph.GA]

Molnár L, Szabados L (2014) V473 Lyrae, a unique second-overtone Cepheid with two modulation cycles. MNRAS 442(4):3222–3234. https://doi.org/10.1093/mnras/stu1091, https://arxiv.org/abs/1406.0494 [astro-ph.SR]

Molnár L, Derekas A, Szabó R, et al (2017) V473 Lyr, a modulated, period-doubled Cepheid, and U TrA, a double-mode Cepheid, observed by MOST. MNRAS 466(4):4009–4020. https://doi.org/10.1093/mnras/stw3345, https://arxiv.org/abs/1612.06722 [astro-ph.SR]

Monelli M, Fiorentino G (2022) RR Lyrae Stars and Anomalous Cepheids as Population Tracers in Local Group Galaxies. Universe 8(3):191. https://doi.org/10.3390/universe8030191

Monty S, Rigaut F, McDermid R, et al (2021) Towards realistic modelling of the astrometric capabilities of MCAO systems: detecting an intermediate-mass black hole with MAVIS. MNRAS 507(2):2192–2207. https://doi.org/10.1093/mnras/stab2199, https://arxiv.org/abs/2107.13199 [astro-ph.GA]

Moore CE, Minnaert M, Houtgast J (1966) The Solar Spectrum 2935 Å to 8770 Å

Moskalik P, Buchler JR, Marom A (1992) Toward a Resolution of the Bump and Beat Cepheid Mass Discrepancies. ApJ 385:685. https://doi.org/10.1086/170975

Moskalik P, Krzyt T, Gorynya NA, et al (2000) Accurate Fourier Decomposition of Cepheid Radial Velocity Curves. In: Szabados L, Kurtz D (eds) IAU Colloq. 176: The Impact of Large-Scale Surveys on Pulsating Star Research, pp 233–234

Munari U, Tomasella L, Fiorucci M, et al (2008) Diffuse interstellar bands in RAVE survey spectra. A&A 488(3):969–973. https://doi.org/10.1051/0004-6361:200810232, https://arxiv.org/abs/0808.1456 [astro-ph]

Nataf DM, Gould A, Fouqué P, et al (2013) Reddening and Extinction toward the Galactic Bulge from OGLE-III: The Inner Milky Way's $R_V \sim 2.5$ Extinction Curve. ApJ 769(2):88. https://doi.org/10.1088/0004-637X/769/2/88, https://arxiv.org/abs/1208.1263 [astro-ph.GA]

Natale G, Marconi M, Bono G (2008) Theoretical Fits of the δ Cephei Light, Radius, and Radial Velocity Curves. ApJ 674(2):L93. https://doi.org/10.1086/526518, https://arxiv.org/abs/0711.2857 [astro-ph]

Neeley JR, Monelli M, Marengo M, et al (2021) Variable Stars in Local Group Galaxies. VI. The Isolated Dwarfs VV 124 and KKr 25. ApJ 920(2):152. https://doi.org/10.3847/1538-4357/ac1a7a

Neilson HR, Lester JB (2008) On the Enhancement of Mass Loss in Cepheids Due to Radial Pulsation. ApJ 684(1):569–587. https://doi.org/10.1086/588650, https://arxiv.org/abs/0803.4198 [astro-ph]

Neilson HR, Cantiello M, Langer N (2011) The Cepheid mass discrepancy and pulsation-driven mass loss. A&A 529:L9. https://doi.org/10.1051/0004-6361/201116920, https://arxiv.org/abs/1104.1638 [astro-ph.SR]

Ngeow C, Kanbur SM (2006) Nonlinear Period-Luminosity Relation for the Large Magellanic Cloud Cepheids: Myths and Truths. ApJ 650(1):180–188. https://doi.org/10.1086/507419, https://arxiv.org/abs/astro-ph/0607059 [astro-ph]

Ngeow CC, Kanbur SM (2005) The linearity of the Wesenheit function for the Large Magellanic Cloud Cepheids. MNRAS 360(3):1033–1039. https://doi.org/10.1111/j.1365-2966.2005.09092.x, https://arxiv.org/abs/astro-ph/0504207 [astro-ph]

Nordström B, Mayor M, Andersen J, et al (2004) The Geneva-Copenhagen survey of the Solar neighbourhood. Ages, metallicities, and kinematic properties of ∼14 000 F and G dwarfs. A&A 418:989–1019. https://doi.org/10.1051/0004-6361:20035959, https://arxiv.org/abs/astro-ph/0405198 [astro-ph]

Oort JH (1927) Observational evidence confirming Lindblad's hypothesis of a rotation of the galactic system. Bull Astron Inst Netherlands 3:275

Origlia L, Ferraro FR, Fabbri S, et al (2014) An empirical mass-loss law for Population II giants from the Spitzer-IRAC survey of Galactic globular clusters. A&A 564:A136. https://doi.org/10.1051/0004-6361/201423617, https://arxiv.org/abs/1403.4096

Owens KA, Freedman WL, Madore BF, et al (2022) Current Challenges in Cepheid Distance Calibrations Using Gaia Early Data Release 3. ApJ 927(1):8. https://doi.org/10.3847/1538-4357/ac479e, https://arxiv.org/abs/2201.00733 [astro-ph.GA]

Palla M, Matteucci F, Spitoni E, et al (2020) Chemical evolution of the Milky Way: constraints on the formation of the thick and thin discs. MNRAS 498(2):1710–1725. https://doi.org/10.1093/mnras/staa2437, https://arxiv.org/abs/2008.07484 [astro-ph.GA]

Pardo I, Poretti E (1997) The galactic double-mode Cepheids. I. Frequency analysis of the light curves and comparison with single-mode Cepheids. A&A 324:121–132

Parenago PP, Kukarkin BW (1936) The Shapes of Light Curves of Long Period Cepheids. Mit 12 Abbildungen. ZAp 11:337

Paxton B, Smolec R, Schwab J, et al (2019) Modules for Experiments in Stellar Astrophysics (MESA): Pulsating Variable Stars, Rotation, Convective Boundaries, and Energy Conservation. ApJS 243(1):10. https://doi.org/10.3847/1538-4365/ab2241, https://arxiv.org/abs/1903.01426 [astro-ph.SR]

Payne-Gaposchkin C (1947) On the light curves of Cepheid variables. AJ 52:218. https://doi.org/10.1086/105998

Payne-Gaposchkin C (1951) The Intrinsic Variable Stars. In: Hynek JA (ed) 50th Anniversary of the Yerkes Observatory and Half a Century of Progress in Astrophysics, p 495

Payne-Gaposchkin C (1954) The Cepheid variables and RR Lyrae stars. Annals of Harvard College Observatory 113:151–186

Pedicelli S, Lemasle B, Groenewegen M, et al (2010) New Baade-Wesselink distances and radii for four metal-rich Galactic Cepheids. A&A 518:A11. https://doi.org/10.1051/0004-6361/201014262, https://arxiv.org/abs/1003.3854 [astro-ph.SR]

Petersen JO (1973) Masses of double mode cepheid variables determined by analysis of period ratios. A&A 27:89

Piatti AE, Koch A (2018) Search for an Intrinsic Metallicity Spread in Old Globular Clusters of the Large Magellanic Cloud. ApJ 867(1):8. https://doi.org/10.3847/1538-4357/aadfe1, https://arxiv.org/abs/1809.01709 [astro-ph.GA]

Pietrinferni A, Cassisi S, Bono G, et al (2006a) Horizontal Branch stars: He-enhanced stellar models. Mem Soc Astron Italiana 77:144

Pietrinferni A, Cassisi S, Salaris M, et al (2006b) A Large Stellar Evolution Database for Population Synthesis Studies. II. Stellar Models and Isochrones for an α-enhanced Metal Distribution. ApJ 642:797–812. https://doi.org/10.1086/501344, https://arxiv.org/abs/astro-ph/0603721

Pietrukowicz P, Soszyński I, Udalski A (2021) Classical Cepheids in the Milky Way. Acta Astron 71(3):205–222. https://doi.org/10.32023/0001-5237/71.3.2, https://arxiv.org/abs/2112.03284 [astro-ph.SR]

Pietrzyński G, Gieren W, Soszyński I, et al (2006) The Araucaria Project: The Distance to the Local Group Galaxy IC 1613 from Near-Infrared Photometry of Cepheid Variables. ApJ 642(1):216–224. https://doi.org/10.1086/500926, https://arxiv.org/abs/astro-ph/0601309 [astro-ph]

Pietrzyński G, Gieren W, Udalski A, et al (2007) The Araucaria Project: The Distance to the Local Group Galaxy WLM from Cepheid Variables Discovered in a Wide-Field Imaging Survey. AJ 134(2):594–603. https://doi.org/10.1086/518599, https://arxiv.org/abs/0704.2075 [astro-ph]

Pietrzyński G, Thompson IB, Gieren W, et al (2010) The dynamical mass of a classical Cepheid variable star in an eclipsing binary system. Nature 468:542–544. https://doi.org/10.1038/nature09598

Pietrzyński G, Graczyk D, Gieren W, et al (2013) An eclipsing-binary distance to the Large Magellanic Cloud accurate to two per cent. Nature 495:76–79. https://doi.org/10.1038/nature11878, https://arxiv.org/abs/1303.2063 [astro-ph.GA]

Pietrzyński G, Graczyk D, Gallenne A, et al (2019) A distance to the Large Magellanic Cloud that is precise to one per cent. Nature 567:200–203. https://doi.org/10.

1038/s41586-019-0999-4, https://arxiv.org/abs/1903.08096 [astro-ph.GA]

Pilecki B, Graczyk D, Gieren W, et al (2015) The Araucaria Project: the First-overtone Classical Cepheid in the Eclipsing System OGLE-LMC-CEP-2532. ApJ 806(1):29. https://doi.org/10.1088/0004-637X/806/1/29, https://arxiv.org/abs/1504.04611 [astro-ph.SR]

Pilecki B, Gieren W, Smolec R, et al (2017) Mass and p-factor of the Type II Cepheid OGLE-LMC-T2CEP-098 in a Binary System. ApJ 842(2):110. https://doi.org/10.3847/1538-4357/aa6ff7, https://arxiv.org/abs/1704.07782 [astro-ph.SR]

Pilecki B, Dervişoğlu A, Gieren W, et al (2018) The Dynamical Mass and Evolutionary Status of the Type II Cepheid in the Eclipsing Binary System OGLE-LMC-T2CEP-211 with a Double-ring Disk. ApJ 868(1):30. https://doi.org/10.3847/1538-4357/aae68f, https://arxiv.org/abs/1810.06524 [astro-ph.SR]

Pilecki B, Pietrzyński G, Anderson RI, et al (2021) Cepheids with Giant Companions. I. Revealing a Numerous Population of Double-lined Binary Cepheids. ApJ 910(2):118. https://doi.org/10.3847/1538-4357/abe7e9, https://arxiv.org/abs/2102.11302 [astro-ph.SR]

Poretti E, Baglin A, Weiss WW (2014) The CoRoT Discovery of a Unique Triple-mode Cepheid in the Galaxy. ApJ 795(2):L36. https://doi.org/10.1088/2041-8205/795/2/L36, https://arxiv.org/abs/1410.8331 [astro-ph.SR]

Prada Moroni PG, Gennaro M, Bono G, et al (2012) On the Evolutionary and Pulsation Mass of Classical Cepheids. III. The Case of the Eclipsing Binary Cepheid CEP0227 in the Large Magellanic Cloud. ApJ 749(2):108. https://doi.org/10.1088/0004-637X/749/2/108, https://arxiv.org/abs/1202.2855 [astro-ph.SR]

Proxauf B, da Silva R, Kovtyukh VV, et al (2018) A new and homogeneous metallicity scale for Galactic classical Cepheids. I. Physical parameters. A&A 616:A82. https://doi.org/10.1051/0004-6361/201833087, https://arxiv.org/abs/1805.00727 [astro-ph.SR]

Rabidoux K, Smith HA, Pritzl BJ, et al (2010) Light Curves and Period Changes of Type II Cepheids in the Globular Clusters M3 and M5. AJ 139:2300–2307. https://doi.org/10.1088/0004-6256/139/6/2300, https://arxiv.org/abs/1003.5924 [astro-ph.SR]

Randich S, Gilmore G, Magrini L, et al (2022) The Gaia-ESO Public Spectroscopic Survey: Implementation, data products, open cluster survey, science, and legacy. A&A 666:A121. https://doi.org/10.1051/0004-6361/202243141, https://arxiv.org/abs/2206.02901 [astro-ph.GA]

Rich RM, Origlia L, Valenti E (2012) Detailed Abundances for M Giants in Two Inner Bulge Fields from Infrared Spectroscopy. ApJ 746(1):59. https://doi.org/10.

1088/0004-637X/746/1/59, https://arxiv.org/abs/1112.0306 [astro-ph.GA]

Riess AG, Casertano S, Yuan W, et al (2019) Large Magellanic Cloud Cepheid Standards Provide a 1% Foundation for the Determination of the Hubble Constant and Stronger Evidence for Physics beyond ΛCDM. ApJ 876(1):85. https://doi.org/10.3847/1538-4357/ab1422, https://arxiv.org/abs/1903.07603 [astro-ph.CO]

Riess AG, Casertano S, Yuan W, et al (2021) Cosmic Distances Calibrated to 1% Precision with Gaia EDR3 Parallaxes and Hubble Space Telescope Photometry of 75 Milky Way Cepheids Confirm Tension with ΛCDM. ApJ 908(1):L6. https://doi.org/10.3847/2041-8213/abdbaf, https://arxiv.org/abs/2012.08534 [astro-ph.CO]

Riess AG, Anand GS, Yuan W, et al (2023) Crowded No More: The Accuracy of the Hubble Constant Tested with High-resolution Observations of Cepheids by JWST. ApJ 956(1):L18. https://doi.org/10.3847/2041-8213/acf769, https://arxiv.org/abs/2307.15806 [astro-ph.CO]

Riess AG, Anand GS, Yuan W, et al (2024) JWST Observations Reject Unrecognized Crowding of Cepheid Photometry as an Explanation for the Hubble Tension at 8σ Confidence. ApJ 962(1):L17. https://doi.org/10.3847/2041-8213/ad1ddd, https://arxiv.org/abs/2401.04773 [astro-ph.CO]

Ripepi V, Marconi M, Moretti MI, et al (2014) The VMC Survey - VIII. First results for anomalous Cepheids. MNRAS 437:2307–2319. https://doi.org/10.1093/mnras/stt2047, https://arxiv.org/abs/1310.5967 [astro-ph.SR]

Ripepi V, Moretti MI, Marconi M, et al (2015) The VMC Survey - XIII. Type II Cepheids in the Large Magellanic Cloud. MNRAS 446:3034–3061. https://doi.org/10.1093/mnras/stu2260, https://arxiv.org/abs/1410.7817 [astro-ph.SR]

Ripepi V, Marconi M, Moretti MI, et al (2016) The VMC Survey. XIX. Classical Cepheids in the Small Magellanic Cloud. ApJS 224:21. https://doi.org/10.3847/0067-0049/224/2/21, https://arxiv.org/abs/1602.09005 [astro-ph.SR]

Ripepi V, Cioni MRL, Moretti MI, et al (2017) The VMC survey - XXV. The 3D structure of the Small Magellanic Cloud from Classical Cepheids. MNRAS 472(1):808–827. https://doi.org/10.1093/mnras/stx2096, https://arxiv.org/abs/1707.04500 [astro-ph.GA]

Ripepi V, Molinaro R, Musella I, et al (2019) Reclassification of Cepheids in the Gaia Data Release 2. Period-luminosity and period-Wesenheit relations in the Gaia passbands. A&A 625:A14. https://doi.org/10.1051/0004-6361/201834506, https://arxiv.org/abs/1810.10486 [astro-ph.SR]

Ripepi V, Catanzaro G, Molinaro R, et al (2021) Cepheid metallicity in the Leavitt law (C-metall) survey - I. HARPS-N@TNG spectroscopy of 47 classical Cepheids and 1 BL Her variables. MNRAS 508(3):4047–4071. https://doi.org/10.1093/

mnras/stab2460, https://arxiv.org/abs/2108.11391 [astro-ph.GA]

Ripepi V, Catanzaro G, Clementini G, et al (2022a) Classical Cepheid period-Wesenheit-metallicity relation in the Gaia bands. arXiv e-prints arXiv:2201.01126. https://arxiv.org/abs/2201.01126 [astro-ph.SR]

Ripepi V, Chemin L, Molinaro R, et al (2022b) The VMC survey - XLVIII. Classical cepheids unveil the 3D geometry of the LMC. MNRAS 512(1):563–582. https://doi.org/10.1093/mnras/stac595, https://arxiv.org/abs/2203.01780 [astro-ph.GA]

Ripepi V, Clementini G, Molinaro R, et al (2022c) Gaia DR3: Specific processing and validation of all-sky RR Lyrae and Cepheid stars – The Cepheid sample. arXiv e-prints arXiv:2206.06212. https://doi.org/10.48550/arXiv.2206.06212, https://arxiv.org/abs/2206.06212 [astro-ph.SR]

Rodgers AW (1970) The masses of pulsating stars. MNRAS 151:133. https://doi.org/10.1093/mnras/151.1.133

Rogers FJ, Iglesias CA (1992) Radiative Atomic Rosseland Mean Opacity Tables. ApJS 79:507. https://doi.org/10.1086/191659

Romaniello M, Primas F, Mottini M, et al (2008) The influence of chemical composition on the properties of Cepheid stars. II. The iron content. A&A 488:731–747. https://doi.org/10.1051/0004-6361:20065661, https://arxiv.org/abs/0807.1196

Romaniello M, Riess A, Mancino S, et al (2022) The iron and oxygen content of LMC Classical Cepheids and its implications for the extragalactic distance scale and Hubble constant. Equivalent width analysis with Kurucz stellar atmosphere models. A&A 658:A29. https://doi.org/10.1051/0004-6361/202142441, https://arxiv.org/abs/2110.08860 [astro-ph.CO]

Ruffoni MP, Den Hartog EA, Lawler JE, et al (2014) Fe I oscillator strengths for the Gaia-ESO survey. MNRAS 441(4):3127–3136. https://doi.org/10.1093/mnras/stu780, https://arxiv.org/abs/1404.5578 [astro-ph.SR]

Salaris M, Cassisi S (2005) Evolution of Stars and Stellar Populations

Salaris M, Althaus LG, García-Berro E (2013) Comparison of theoretical white dwarf cooling timescales. A&A 555:A96. https://doi.org/10.1051/0004-6361/201220622, https://arxiv.org/abs/1306.2575 [astro-ph.SR]

Sandage A (2005) Centennial History of the Carnegie Institution of Washington, pg. 495

Sandage A, Tammann GA (2006) Absolute Magnitude Calibrations of Population I and II Cepheids and Other Pulsating Variables in the Instability Strip of the Hertzsprung-Russell Diagram. ARA&A 44:93–140. https://doi.org/10.1146/annurev.astro.43.072103.150612

Sandage AR (1972) Classical Cepheids: Cornerstone to Extragalactic Distances. QJRAS 13:202

Saydjari AK, Zucker C, Peek JEG, et al (2022) Measuring the 8621 Å Diffuse Interstellar Band in Gaia DR3 RVS Spectra: Obtaining a Clean Catalog by Marginalizing over Stellar Types. arXiv e-prints arXiv:2212.03879. https://doi.org/10.48550/arXiv.2212.03879, https://arxiv.org/abs/2212.03879 [astro-ph.GA]

Schlafly EF, Finkbeiner DP (2011) Measuring Reddening with Sloan Digital Sky Survey Stellar Spectra and Recalibrating SFD. ApJ 737:103. https://doi.org/10.1088/0004-637X/737/2/103, https://arxiv.org/abs/1012.4804 [astro-ph.GA]

Schlegel DJ, Finkbeiner DP, Davis M (1998) Maps of Dust Infrared Emission for Use in Estimation of Reddening and Cosmic Microwave Background Radiation Foregrounds. ApJ 500:525–+. https://doi.org/10.1086/305772, https://arxiv.org/abs/arXiv:astro-ph/9710327

Seaton MJ, Yan Y, Mihalas D, et al (1994) Opacities for stellar envelopes. MNRAS 266:805. https://doi.org/10.1093/mnras/266.4.805

Shapley H, McKibben V (1940) Galactic and Extragalactic Studies, V. The Period Frequency of Classical Cepheids in the Magellanic Clouds. Proceedings of the National Academy of Science 26(2):105–115. https://doi.org/10.1073/pnas.26.2.105

Shipp N, Erkal D, Drlica-Wagner A, et al (2021) Measuring the Mass of the Large Magellanic Cloud with Stellar Streams Observed by S ^{5}. ApJ 923(2):149. https://doi.org/10.3847/1538-4357/ac2e93, https://arxiv.org/abs/2107.13004 [astro-ph.GA]

Simmerer J, Sneden C, Cowan JJ, et al (2004) The Rise of the s-Process in the Galaxy. ApJ 617(2):1091–1114. https://doi.org/10.1086/424504, https://arxiv.org/abs/astro-ph/0410396 [astro-ph]

Simon NR (1976) Nonlinear Cepheid Pulsations in the Iterative Approximation. In: Cox AN, Deupree RG (eds) Solar and Stellar Pulsation Conference, p 173

Simon NR (1995) Cepheids: pulsation, evolution, opacity. Highlights of Astronomy 10:593

Simon NR, Lee AS (1981) The structural properties of cepheid light curves. ApJ 248:291–297. https://doi.org/10.1086/159153

Simon NR, Schmidt EG (1976) Evidence Favoring Nonevolutionary Cepheid Masses. ApJ 205:162–164. https://doi.org/10.1086/154259

Simon NR, Young TS (1997) The Cepheid instability strip and the calibration of the

primary distance scale. MNRAS 288(1):267–272. https://doi.org/10.1093/mnras/288.1.267

Skowron DM, Soszyński I, Udalski A, et al (2016) OGLE-ing the Magellanic System: Photometric Metallicity from Fundamental Mode RR Lyrae Stars. Acta Astron 66(3):269–292. https://arxiv.org/abs/1608.00013 [astro-ph.SR]

Skowron DM, Skowron J, Mróz P, et al (2019) A three-dimensional map of the Milky Way using classical Cepheid variable stars. Science 365(6452):478–482. https://doi.org/10.1126/science.aau3181, https://arxiv.org/abs/1806.10653 [astro-ph.GA]

Skowron DM, Skowron J, Udalski A, et al (2021) OGLE-ing the Magellanic System: Optical Reddening Maps of the Large and Small Magellanic Clouds from Red Clump Stars. ApJS 252(2):23. https://doi.org/10.3847/1538-4365/abcb81, https://arxiv.org/abs/2006.02448 [astro-ph.SR]

Smolec R, Moskalik P, Plachy E, et al (2018) Diversity of dynamical phenomena in type II Cepheids of the OGLE collection. MNRAS 481(3):3724–3749. https://doi.org/10.1093/mnras/sty2452, https://arxiv.org/abs/1809.02842 [astro-ph.SR]

Smolec R, Ziółkowska O, Ochalik M, et al (2023) First overtone Cepheids of the OGLE Magellanic Cloud Collection - beyond radial modes. MNRAS 519(3):4010–4029. https://doi.org/10.1093/mnras/stac3706, https://arxiv.org/abs/2212.06732 [astro-ph.SR]

Sneden C, Cowan JJ, Gallino R (2008) Neutron-capture elements in the early galaxy. ARA&A 46:241–288. https://doi.org/10.1146/annurev.astro.46.060407.145207

Soszyński I, Poleski R, Udalski A, et al (2008a) The Optical Gravitational Lensing Experiment. Triple-Mode and 1O/3O Double-Mode Cepheids in the Large Magellanic Cloud. Acta Astron 58:153–162. https://arxiv.org/abs/0807.4182

Soszyński I, Udalski A, Szymański MK, et al (2008b) The Optical Gravitational Lensing Experiment. The OGLE-III Catalog of Variable Stars. II.Type II Cepheids and Anomalous Cepheids in the Large Magellanic Cloud. Acta Astron 58:293. https://arxiv.org/abs/0811.3636

Soszyński I, Udalski A, Pietrukowicz P, et al (2011) The Optical Gravitational Lensing Experiment. The OGLE-III Catalog of Variable Stars. XIV. Classical and TypeII Cepheids in the Galactic Bulge. Acta Astron 61:285–301. https://arxiv.org/abs/1112.1406 [astro-ph.SR]

Soszyński I, Udalski A, Szymański MK, et al (2014) Over 38000 RR Lyrae Stars in the OGLE Galactic Bulge Fields. Acta Astron 64:177–196. https://arxiv.org/abs/1410.1542 [astro-ph.SR]

Soszyński I, Udalski A, Szymański MK, et al (2015a) The OGLE Collection of

Variable Stars. Anomalous Cepheids in the Magellanic Clouds. Acta Astron 65:233–250. https://arxiv.org/abs/1508.00907 [astro-ph.SR]

Soszyński I, Udalski A, Szymański MK, et al (2015b) The OGLE Collection of Variable Stars. Classical Cepheids in the Magellanic System. Acta Astron 65:297–312. https://arxiv.org/abs/1601.01318 [astro-ph.SR]

Soszyński I, Udalski A, Szymański MK, et al (2017a) Concluding Henrietta Leavitt's Work on Classical Cepheids in the Magellanic System and Other Updates of the OGLE Collection of Variable Stars. Acta Astron 67(2):103–113. https://doi.org/10.32023/0001-5237/67.2.1, https://arxiv.org/abs/1706.09452 [astro-ph.SR]

Soszyński I, Udalski A, Szymański MK, et al (2017b) The OGLE Collection of Variable Stars. Classical, Type II, and Anomalous Cepheids toward the Galactic Center. Acta Astron 67:297–316. https://arxiv.org/abs/1712.01307 [astro-ph.SR]

Soszyński I, Udalski A, Szymański MK, et al (2018) The OGLE Collection of Variable Stars. Type II Cepheids in the Magellanic System. Acta Astron 68:89–109. https://arxiv.org/abs/1807.00008 [astro-ph.SR]

Soszyński I, Smolec R, Udalski A, et al (2019) Type II Cepheids Pulsating in the First Overtone from the OGLE Survey. ApJ 873(1):43. https://doi.org/10.3847/1538-4357/ab04ab, https://arxiv.org/abs/1902.02352 [astro-ph.SR]

Soszyński I, Smolec R, Udalski A, et al (2020) OGLE-GAL-ACEP-091: The First Known Multi-mode Anomalous Cepheid. ApJ 901(2):L25. https://doi.org/10.3847/2041-8213/abb817, https://arxiv.org/abs/2009.06642 [astro-ph.SR]

Sousa SG, Santos NC, Israelian G, et al (2007) A new code for automatic determination of equivalent widths: Automatic Routine for line Equivalent widths in stellar Spectra (ARES). A&A 469:783–791. https://doi.org/10.1051/0004-6361:20077288, https://arxiv.org/abs/astro-ph/0703696

Sousa SG, Santos NC, Adibekyan V, et al (2015) ARES v2: new features and improved performance. A&A 577:A67. https://doi.org/10.1051/0004-6361/201425463, https://arxiv.org/abs/1504.02725 [astro-ph.IM]

Spitoni E, Cescutti G, Minchev I, et al (2019) 2D chemical evolution model: The impact of Galactic disc asymmetries on azimuthal chemical abundance variations. A&A 628:A38. https://doi.org/10.1051/0004-6361/201834665, https://arxiv.org/abs/1811.11196 [astro-ph.GA]

Stellingwerf RF (1982a) Convection in Pulsating Stars - Part Two - Rr-Lyrae Convection and Stability. ApJ 262:339. https://doi.org/10.1086/160426

Stellingwerf RF (1982b) Convection in pulsating stars. I - Nonlinear hydrodynamics. II - RR Lyrae convection and stability. ApJ 262:330–343. https://doi.org/10.1086/

160425

Stellingwerf RF (1984a) Convection in pulsating stars. IV - Nonlinear effects. ApJ 277:327–332. https://doi.org/10.1086/161699

Stellingwerf RF (1984b) Convection in pulsating stars. V - Limit cycle characteristics. ApJ 284:712–718. https://doi.org/10.1086/162454

Stobie RS (1969) Cepheid pulsation-II. Models fitted to evolutionary tracks. MNRAS 144:485. https://doi.org/10.1093/mnras/144.4.485

Storm J, Gieren W, Fouqué P, et al (2011) Calibrating the Cepheid period-luminosity relation from the infrared surface brightness technique. II. The effect of metallicity and the distance to the LMC. A&A 534:A95. https://doi.org/10.1051/0004-6361/201117154, https://arxiv.org/abs/1109.2016 [astro-ph.CO]

Strom SE, Strom KM, Rood RT, et al (1970) On the Evolutionary Status of Stars above the Horizontal Branch in Globular Clusters. A&A 8:243

Sturch CR (1978) UBV photometry of RR Lyrae stars in Omega Centauri. PASP 90:264–266. https://doi.org/10.1086/130323

Subramanian S, Subramaniam A (2015) Disk of the Small Magellanic Cloud as traced by Cepheids. A&A 573:A135. https://doi.org/10.1051/0004-6361/201424248, https://arxiv.org/abs/1410.7588 [astro-ph.GA]

Subramanian S, Marengo M, Bhardwaj A, et al (2017) Young and Intermediate-Age Distance Indicators. Space Sci Rev 212(3-4):1817–1869. https://doi.org/10.1007/s11214-017-0427-8, https://arxiv.org/abs/1709.07265 [astro-ph.SR]

Sweigart AV, Greggio L, Renzini A (1989) The Development of the Red Giant Branch. I. Theoretical Evolutionary Sequences. ApJS 69:911. https://doi.org/10.1086/191331

Szabó R, Buchler JR, Bartee J (2007) The Cepheid Phase Lag Revisited. ApJ 667(2):1150–1160. https://doi.org/10.1086/520917, https://arxiv.org/abs/astro-ph/0703568 [astro-ph]

Szabó R, Szabados L, Ngeow CC, et al (2011) Cepheid investigations using the Kepler space telescope. MNRAS 413(4):2709–2720. https://doi.org/10.1111/j.1365-2966.2011.18342.x, https://arxiv.org/abs/1101.2443 [astro-ph.SR]

Sziládi K, Vinkó J, Poretti E, et al (2007) New homogeneous iron abundances of double-mode Cepheids from high-resolution echelle spectroscopy. A&A 473(2):579–587. https://doi.org/10.1051/0004-6361:20077539, https://arxiv.org/abs/0707.2530 [astro-ph]

Takase B, Miyauchi-Isobe N (1984) Kiso survey for ultraviolet-excess galaxies. I.

Annals of the Tokyo Astronomical Observatory 19:595–638

Tammann GA, Sandage A, Reindl B (2003) New Period-Luminosity and Period-Color relations of classical Cepheids: I. Cepheids in the Galaxy. A&A 404:423–448. https://doi.org/10.1051/0004-6361:20030354, https://arxiv.org/abs/arXiv:astro-ph/0303378

Tammann GA, Sandage A, Reindl B (2008) The expansion field: the value of H_0. A&A Rev 15(4):289–331. https://doi.org/10.1007/s00159-008-0012-y, https://arxiv.org/abs/0806.3018 [astro-ph]

Tautvaišienė G, Drazdauskas A, Mikolaitis Š, et al (2015) The Gaia-ESO Survey: CNO abundances in the open clusters Trumpler 20, NGC 4815, and NGC 6705. A&A 573:A55. https://doi.org/10.1051/0004-6361/201424989, https://arxiv.org/abs/1411.2831 [astro-ph.SR]

Taylor BJ (1994) Analyses of Archival Data for Cool Dwarfs. II. A Catalog of Temperatures. PASP 106:452. https://doi.org/10.1086/133400

Thévenin F, Idiart TP (1999) Stellar Iron Abundances: Non-LTE Effects. ApJ 521(2):753–763. https://doi.org/10.1086/307578, https://arxiv.org/abs/astro-ph/9906433 [astro-ph]

Trentin E, Ripepi V, Catanzaro G, et al (2023) Cepheid Metallicity in the Leavitt Law (C- MetaLL) survey - II. High-resolution spectroscopy of the most metal poor Galactic Cepheids. MNRAS 519(2):2331–2348. https://doi.org/10.1093/mnras/stac2459, https://arxiv.org/abs/2209.03792 [astro-ph.GA]

Trundle C, Lennon DJ (2005) Understanding B-type supergiants in the low metallicity environment of the SMC II. A&A 434(2):677–689. https://doi.org/10.1051/0004-6361:20042061, https://arxiv.org/abs/astro-ph/0501228 [astro-ph]

Trundle C, Dufton PL, Hunter I, et al (2007) The VLT-FLAMES survey of massive stars: evolution of surface N abundances and effective temperature scales in the Galaxy and Magellanic Clouds. Astronomy and Astrophysics, Volume 471, Issue 2, August IV 2007, pp.625-643, https://doi.org/10.1051/0004-6361:20077838, 0706.1731

Udalski A, Soszyński I, Szymanski M, et al (1999) The Optical Gravitational Lensing Experiment. Cepheids in the Magellanic Clouds. IV. Catalog of Cepheids from the Large Magellanic Cloud. Acta Astron 49:223–317. https://arxiv.org/abs/arXiv:astro-ph/9908317

Udalski A, Soszyński I, Szymański MK, et al (2015) Eclipsing Binaries with Classical Cepheid Component in the Magellanic System. Acta Astron 65(4):341–350. https://doi.org/10.48550/arXiv.1601.01683, https://arxiv.org/abs/1601.01683 [astro-ph.SR]

Udalski A, Soszyński I, Pietrukowicz P, et al (2018) OGLE Collection of Galactic Cepheids. Acta Astron 68(4):315–339. https://doi.org/10.32023/0001-5237/68.4.1, https://arxiv.org/abs/1810.09489 [astro-ph.SR]

van Albada TS, Baker N (1971) On the Masses, Luminosities, and Compositions of Horizontal-Branch Stars. ApJ 169:311. https://doi.org/10.1086/151144

van Albada TS, Baker N (1973) On the Two Oosterhoff Groups of Globular Clusters. ApJ 185:477–498. https://doi.org/10.1086/152434

van den Bergh S (1975) The Extragalactic Distance Scale, the University of Chicago Press, p 509

van den Bergh S (2006) Globular Clusters in Dwarf Galaxies. AJ 131(1):304–311. https://doi.org/10.1086/498688, https://arxiv.org/abs/astro-ph/0509811 [astro-ph]

van Leeuwen F, Feast MW, Whitelock PA, et al (2007) Cepheid parallaxes and the Hubble constant. MNRAS 379(2):723–737. https://doi.org/10.1111/j.1365-2966.2007.11972.x, https://arxiv.org/abs/0705.1592 [astro-ph]

VandenBerg DA, Brogaard K, Leaman R, et al (2013) The Ages of 55 Globular Clusters as Determined Using an Improved \Delta Vˆ HB_TO Method along with Color-Magnitude Diagram Constraints, and Their Implications for Broader Issues. ApJ 775:134. https://doi.org/10.1088/0004-637X/775/2/134, https://arxiv.org/abs/1308.2257 [astro-ph.GA]

Vasilyev V, Ludwig HG, Freytag B, et al (2018) Spectroscopic properties of a two-dimensional time-dependent Cepheid model. II. Determination of stellar parameters and abundances. A&A 611:A19. https://doi.org/10.1051/0004-6361/201732201, https://arxiv.org/abs/1711.00236 [astro-ph.SR]

Vasilyev V, Amarsi AM, Ludwig HG, et al (2019) Two-dimensional non-LTE O I 777 nm line formation in radiation hydrodynamics simulations of Cepheid atmospheres. A&A 624:A85. https://doi.org/10.1051/0004-6361/201935067, https://arxiv.org/abs/1903.02109 [astro-ph.SR]

Venn KA, Przybilla N (2003) New Nitrogen and Carbon in AF-supergiants (invited review). In: Charbonnel C, Schaerer D, Meynet G (eds) CNO in the Universe, p 20

Viscasillas Vázquez C, Magrini L, Casali G, et al (2022) The Gaia-ESO survey: Age-chemical-clock relations spatially resolved in the Galactic disc. A&A 660:A135. https://doi.org/10.1051/0004-6361/202142937, https://arxiv.org/abs/2202.04863 [astro-ph.GA]

Wagenhuber J, Groenewegen MAT (1998) New input data for synthetic AGB evolution. A&A 340:183–195. https://arxiv.org/abs/astro-ph/9809338

Walker AR, Terndrup DM (1991) The metallicity of RR Lyrae stars in Baade's window. ApJ 378:119–126. https://doi.org/10.1086/170411

Wallerstein G (2002) The Cepheids of Population II and Related Stars. PASP 114:689–699. https://doi.org/10.1086/341698

Wallerstein G, Cox AN (1984) The Population II Cepheids. PASP 96:677–691. https://doi.org/10.1086/131406

Weiss A, Ferguson JW (2009) New asymptotic giant branch models for a range of metallicities. A&A 508:1343–1358. https://doi.org/10.1051/0004-6361/200912043, https://arxiv.org/abs/0903.2155 [astro-ph.SR]

Welch DL, MACHO Collaboration (1999) Cepheid Variables in the LMC and SMC. In: Chu YH, Suntzeff N, Hesser J, et al (eds) New Views of the Magellanic Clouds, p 513

Whitney C (1956) The velocity humps of classical Cepheids. AJ 61:193. https://doi.org/10.1086/107419

Wood MP, Lawler JE, Sneden C, et al (2013) Improved Ti II Log(gf) Values and Abundance Determinations in the Photospheres of the Sun and Metal-Poor Star HD 84937. ApJS 208(2):27. https://doi.org/10.1088/0067-0049/208/2/27, https://arxiv.org/abs/1309.1440 [astro-ph.SR]

Wood PR (1998) Deriving distances from nonlinear pulsation models of bump Cepheids. Mem Soc Astron Italiana 69:99–108

Wood PR, S. Arnold A, Sebo KM (1997) Nonlinear Models of the Bump Cepheid HV 905 and the Distance Modulus to the Large Magellanic Cloud. ApJ 485(1):L25–L28. https://doi.org/10.1086/310798

Yong D, Carney BW, Teixera de Almeida ML, et al (2006) Elemental Abundance Ratios in Stars of the Outer Galactic Disk. III. Cepheids. AJ 131(4):2256–2273. https://doi.org/10.1086/500538, https://arxiv.org/abs/astro-ph/0512348 [astro-ph]

Yong D, Carney BW, Friel ED (2012) Elemental Abundance Ratios in Stars of the Outer Galactic Disk. IV. A New Sample of Open Clusters. AJ 144(4):95. https://doi.org/10.1088/0004-6256/144/4/95, https://arxiv.org/abs/1206.6931 [astro-ph.GA]

Zhao H, Schultheis M, Recio-Blanco A, et al (2021) The diffuse interstellar band around 8620 Å. I. Methods and application to the GIBS data set. A&A 645:A14. https://doi.org/10.1051/0004-6361/202039736, https://arxiv.org/abs/2011.10484 [astro-ph.GA]

Zinn R, Searle L (1976) The masses of the anomalous cepheids in the Draco system.

ApJ 209:734–747. https://doi.org/10.1086/154772

Zoccali M, Vasquez S, Gonzalez OA, et al (2017) The GIRAFFE Inner Bulge Survey (GIBS). III. Metallicity distributions and kinematics of 26 Galactic bulge fields. A&A 599:A12. https://doi.org/10.1051/0004-6361/201629805, https://arxiv.org/abs/1610.09174